UNIVERSITÉ DU QUÉBEC À MONTRÉAL

MÉTHODE DE TÉLESCOPAGE APPLIQUÉE AU MODÈLE RÉGIONAL CANADIEN DU CLIMAT (MRCC5) POUR UNE ÉTUDE DE FAISABILITÉ DE CE MODÈLE À TRÈS HAUTE RÉSOLUTION

MÉMOIRE

PRÉSENTÉ

COMME EXIGENCE PARTIELLE

DE LA MAÎTRISE EN SCIENCES DE L'ATMOSPHÈRE

PAR

MÉLISSA CHOLETTE

DÉCEMBRE 2013

REMERCIEMENTS

Tout d'abord, je tiens à remercier mon directeur de recherche, le professeur René Laprise, pour son soutien, ses idées et ses commentaires sans lesquels ce projet n'aurait certes pas abouti. Un merci spécial à Katja Winger et Emilia Paula Diaconescu pour leurs réponses à mes questions. Finalement, je remercie le Centre ESCER pour son soutien financier et tous ses participants (professeurs, chercheurs, employés et étudiants) pour le soutien moral au cours de cette maîtrise.

TABLE DES MATIÈRES

LISTE DES FIGURES

LISTE DES TABLEAUX

LISTE DES ACRONYMES

ACCESS	Australian Community Climate and Earth System Simulator (CSIRO, Australia)
ALADIN	Aire Limitée Adaptation dynamique Développement InterNational (CNRM, France)
AMCG	Composante Atmosphérique des Modèles de Circulation Générale
AOM	Atmospheric-Ocean Model (GISS, USA)
ARCMIP	Arctic Regional Climate Model Intercomparion Project
ARNO	Rainfall-Runoff Surface Model of REMO and HIRHAM5 models
ARPEGE	Action de Recherche Petite Échelle Grande Échelle (CNRM, France)
AR5	5^{e} rapport d'évaluation sur les changements climatiques du GIEC
BATS1e	Biosphere-Atmosphere Transfer Scheme, version 1e
BCC	Beijing Climate Center (China)
BCCR	Bjerknes Centre for Climate Research (Norway)
BCM	Bergen Climate Model (BCCR, Norway)
BFK	Bechtold-Kain-Fritsch convection scheme
BNU	Beijing Normal University (China)
Bourge 3D	Bourgouin algorithm to determine the types of precipitation
CAM3	Community Atmospheric Model, version 3 (NCAR, USA)
CanCM4	Canadian Climate Model, version 4 (CCCma, Canada)

CanESM	Canadian Earth System Model (CCCma, Canada)
CanRCM4	Regional Climate Model, version 4 (CCCma, Canada)
CBR	Cuxart-Bougeault-Redelsberger scheme for TKE
CCCma	Canadian Centre for Climate Modelling and Analysis (Canada)
CCM2	Community Climate Model, version 2 (NCAR, USA)
CCM3	Community Climate Model, version 3 (NCAR, USA)
CCSM	Community Climate System Model (NCAR, USA)
CCSR	Center for Climate System Research (Japan)
CESM	Community Earth System Model (NCAR, USA)
CESMCMCC	Carbon Earth System Model of CCMC (Italy)
CFLs	Conditions au Frontières Latérales
CFS	Climate Forecast System (COLA, USA)
CGCM	Coupled General Circulation Model (COLA, USA)
CGCM2	Canadian Global Coupled Model, version 2 (OURANOS, Canada)
CHRM	Climate High Resolution Model (GSMS, Germany and Swiss)
CKRS	Correlated-K Radiation Scheme
CLARIS	A Europe-South America Network for Climate Change Assessment and Impact Studies
CLASS2.7	Canadian Land Surface Scheme, version 2.7
CLASS3.5	Canadian Land Surface Scheme, version 3.5
CLM	Climate Limited-area Modeling Community
CLUMEQ	Supercomputer Consortium Laval UQAM McGill and Eastern Quebec
CLWS	Cloud Liquid Water Scheme

CM	Global Coupled Climate Model (GFDL, USA)
CMCC	Centro Euro-Mediterraneo per i Cambiamenti Climatici (Italy)
CMM5	Climate extension of MM5 (NCAR, USA)
CNRM	Centre National de Recherches Météorologiques (France)
COAMPS	Coupled Ocean/Atmosphere Mesoscale Prediction System (Norway)
COLA	Center for Ocean-Land-Atmosphere studies (USA)
CONSUN	Cloud Microphysics Scheme of Sundqvist et al. (1989)
CORDEX	COordinated Regional climate Downscaling EXperiment
COSMO-CLM	COnsortium for Small-scale MOdeling-Climate Limited-area Modeling
CO_2	Dioxide de Carbone
CRCM	Canadian Regional Climate Model (Canada)
CRCM4	Canadian Regional Climate Model, version 4 (OURANOS, Canada)
CRCM5	Canadian Regional Climate Model, version 5 (UQAM, Canada)
CRS	Cloud-Radiation Scheme
CSIRO	Commonwealth Scientific and Industrial Research Organisation, Atmospheric Research (Australia)
CSM	Climate System Model (BCC, Chine)
CSSP	Conjunctive Surface-Subsurface Process Model of CWRF
CWRF	Climate extension of the Weather Research and Forecasting model (NCAR, USA)
DCT	Discrete Cosine Transform
DFT	Discrete Fourier Transform
DHMZ	Croatian Meteorological and Hydrological Service (Croatia)

DMI	Danish Meteorological Institute (Denmark)
DualM-TKE	Combination of TKE scheme and dual mass flux scheme
Dudhia	Dudhia cloud microphysics scheme
Dudhia SW	Dudhia Shortwave radiation scheme
DWD	German Weather Services (Germany)
d81	CRCM5 cascade simulation with 0.81° of horizontal mesh
d27	CRCM5 cascade simulation with 0.27° of horizontal mesh
d9	CRCM5 cascade simulation with 0.09° of horizontal mesh
d9_pilots	CRCM5 simulation with 0.09° of horizontal resolution to provide boundary conditions for d3
d3	CRCM5 cascade simulation with 0.03° of horizontal mesh
d1	CRCM5 cascade simulation with 0.01° of horizontal mesh
ECHAM	European Centre Hamburg Model (MPI, Germany)
ECMWF	European Centre for Medium-Range Weather Forecasts (Europe)
ECP mod G3	Ensemble Cumulus Parameterization, modified from G3
ENSEMBLES	Providing ensembles-based predictions climate changes and their impacts
ERA-Interim	Interim reanalysis project at ECMWF
ESCER	Centre pour l'Étude et la Simulation du Climat à l'Échelle Régionale (UQAM, Canada)
ESM	Earth System Model
FGOALS	Flexible Global Ocean-Atmosphere-Land System model (LASG, Chine)
FIO	First Institute of Oceanography (China)
FMR	Fouquart and Morcrette Radiation scheme

FRPS	Fast Radiation Scheme of RCAO and HIRHAM5
GCESS	College of Global Change and Earth System Science (China)
GCM	General Circulation Model
GCM3	Radiative transfer model of Canadian Global Climate Model, version 3 (CCCma, Canada)
GD	Grell and Dévényi convection scheme
GEM	Global Environmental Multiscale model developed by the Canadian Meteorological Centre (CMC, Canada)
GFDL	Geophysical Fluid Dynamics Laboratory (USA)
GIEC	Groupe d'experts Intergouvernemental sur l'Évolution du Climat
GISS	Goddard Institute for Space Studies (USA)
GISS scheme	Goddard Institute for Space Studies convection scheme
GLAS/UCLA	Goddard Laboratory of Atmospheric Sciences / University of California at Los Angeles long-wave radiation scheme
GR	Grell convection scheme
GRCS	Gregory and Rowntree Convection Scheme
GSFC	Goddard Space Flight Center Cloud Microphysics Scheme
GSFC-GCE	Goddard Space Flight Center Cloud Microphysics Scheme-Goddard Cumulus Ensemble Model
GSMS	German and Swiss Meteorological Services
GWD86	Gravity Wave Drag
G3	New Grell and Dévényi convection scheme
HadCM	Hadley Centre Coupled Model (UKMO, United Kingdom)
HadGEM	Hadley Centre Global Environmental Model (UKMO, United Kingdom)

HadRM3	Hadley Centre Regional Model, version 3 (UKMO, United Kingdom)
HIRAM	Global High Resolution Atmospheric Model (GFDL, USA)
HIRHAM5	High-Resolution Limited-Area Model, version 5 (DMI, Denmark)
ICTP	International Centre for Theoretical Physics (Italy)
IFS	Integrated Forecasting System (ECMWF)
INCA	Integrated Nowcasting through Comprehensive Analysis (Austria)
INM	Institute for Numerical Mathematics (Russia)
IPSL	Institute Pierre Simon Laplace (France)
ISBA	Interactions between Soil-Biosphere-Atmosphere land surface scheme
KE	Kinetic Energy
Kessler	Kessler microphysics scheme
KFC	Kain and Fristch convection scheme
KFC2	Update of Kain-Fristch convective parameterization
KNMI	Koninklijk Nederlands Meteorologisch Instituut (Netherlands)
KSCCS	Kuo-Shallow-Convection Clouds Scheme
K-scheme	Correlated microphysical K-scheme of Rasch and Kristjansson (1998)
LAM	Limited Area Model
LASG	National key Laboratory of Numerical Modeling for Atmospheric Sciences and Geophysical Fluid Dynamics (China)
LBCs	Lateral Boundary Conditions
LCV	Lake Champlain Valley
LocMIP	Local Climate Model Intercomparison Project

LS	Land Surface scheme of RM3
LSS	Land Surface Scheme of RCAO
MCG	Modèle de Circulation Générale
MDDEP	Ministère du Développement Durable, de l'Environnement, de la faune et des Parcs (Québec, Canada)
MDEIE	Ministère du Développement Économique Innovation et Exportation (Québec, Canada)
MIROC	Model for Interdisciplinary Research on Climate (Japan)
MIT	Massachusetts Institute of Technology (USA) convection scheme
Mk	CSIRO Climate System Model (Australia)
MM5	Fifth-generation of the Pennsylvania State University / NCAR Mesoscale Model (USA)
Mod-FMR	Modified Fouquart and Morcrette Radiation scheme
Mod-MY	Modified Mellor and Yamada boundary layer scheme
MOISTKE	MOISTKE boundary-layer cloud scheme
MOSES2	Met Office Surface Exchange Scheme, version 2
MPI	Max Planck Institute for Meteorology (Germany)
MRC	Modèle Régional du Climat
MRCC	Modèle Régional Canadien du Climat (Canada)
MRCC5	Modèle Régional Canadien du Climat, version 5 (UQAM, Canada)
MRF	Medium-Range Forecast model boundary-layer scheme
MRI	Meteorological Research Institute (Japan)
MYDM	Milbrandt and Yau double-moment bulk microphysics scheme
MY2.0	Mellor and Yamada boundary layer scheme, version 2.0

NARCCAP	The North American Regional Climate Change Assessment Program
NASA	National Aeronautics and Space Administration (USA)
NBLMS	New Boundary Layer Mixed Scheme
NCAR	National Center for Atmospheric Research (USA)
NCEP	National Centers for Environmental Prediction (USA)
NNRP	NCEP-NCAR Reanalysis Project
NOAA	National Oceanic and Atmospheric Administration (USA)
Noah	The Community Noah Land-Surface Model
NorESM	Norwegian Earth System Model (BCCR, Norway)
NRCM	Nested Regional Climate Model (NCAR, USA)
NSERC	Natural Sciences and Engineering Research Council (Canada)
NWP	Numerical Weather Prediction
OMCG	Composante Océanique des Modèles de Circulation Générale
OURANOS	Consortium sur la climatologie régional et l'adaptation aux changements climatiques (Québec, Canada)
PCI	Prognostic treatment of Cloud and Ice
PCP	Precipitation and Cloud Parameterization
PEP	Processor for External Parameters
PNT	Prévision Numérique du Temps
PRECIS	Providing Regional Climates for Impacts Studies (UKMO, United Kingdom)
PROMES	Regional Atmospheric Model (UCM, Spain)
PRUDENCE	Prediction of Regional scenarios and Uncertainties for Defining EuropeaN Climate change risks and Effects (Europe)

RACMO2	Regional Atmospheric Climate Model, version 2 (KNMI, Netherland)
RCAO	Rossby Centre Atmosphere-Ocean regional climate model (Sweden)
RCM	Regional Climate Model
RegCM3	Regional Climate Model, version 3 (ICTP, Italy)
REIMS	Regional Economic Input-Output Models
REMO	Regional Model (MPI, Germany)
RMIP	South Australian Regional Mining and Infrastructure Plans
RM3	Regional Model, version 3 (GISS, USA)
RPEWC	Radiation Profiles in Extended Water Clouds parameterization scheme
RRTM	Rapid Radiation Transfer Model
R2	Reisner Microphysics Scheme, version 2
SB	Seifert and Beheng microphysics scheme
SECHIBA	Schématisation des Échanges Hydriques à l'Interface entre la Biosphère et l'Atmosphère
SLRV	St-Lawrence River Valley
SMHI	Swedish Meteorological and Hydrological Institute (Sweden)
SNU-RCM	Seoul National University-Regional Climate Model (SNU, Korea)
SS	Smith Scheme for microphysics
ST	Système Terre
SUBEX	SUB-grid EXplicit moisture scheme
SW rad	Shortwave radiation scheme of Davies (1982)
TERRA_LM	Terrain Land Surface Model

TESSEL	Tiled ECMWF Scheme for Surface Exchanges over Land
TKE	Turbulent Kinetic Energy
UCM	Universidad Complutense de Madrid (Spain)
UKMO	Hadley Centre for Climate Prediction and Research (United Kingdom)
UQAM	Université du Québec À Montréal (Québec, Canada)
USA	United States of America
UTC	Universal Time Coordinated
VSMF	von Salzen and McFarlane boundary-layer scheme
WRF	Weather Research Forecasting model (NCAR, USA)
WSM6	WRF Single-Moment 6-Class Microphysics Scheme
YSU	Yonsei University planetary boundary layer scheme
ZMFS	Zhang and McFarlane convection Scheme

LISTE DES SYMBOLES

$\beta(m)$	Coefficient in the DCT calculation depending on m adimensional wavenumbers in x-direction
$\beta(n)$	Coefficient in the DCT calculation depending on n adimensional wavenumbers in y-direction
$C_{cascade}$	Computational cost of the total cascade
C_{FL}	Courant-Friedrichs-Lewy non-dimensional number
C_{GCM}	Computation cost of a General Circulation Model
C_{LAM}	Computation cost of a Limited-Area Model
f	Coriolis parameter
f_U	The horizontal wind U component discrete field
F_U	Spectral coefficients of the DCT for U component
f_V	The horizontal wind V component discrete field
F_V	Spectral coefficients of the DCT for V component
h	hours
hPa	hectoPascals (pressure unit)
J/m^2	Joules per square meter
k	Horizontal wavenumbers: adimensional $k=\sqrt{m^2+n^2}$ or dimensional $k=2\pi/\lambda$
K	The computational average cost per grid point
KE	Kinetic Energy

km	kilometers
L_t	Length of a simulation
L_x	Length of horizontal domain in x-direction
L_y	Length of horizontal domain in y-direction
L_z	Height of the computational domain
m	Adimensional wavenumbers in x-direction
mm	millimeters
min	minutes
m/s	meters/second
n	Adimensional wavenumbers in y-direction
η	Total number of steps during the telescoping
Π	Brunt-Väisälä frequency
N	Number of horizontal grid points when $N_x = N_y$
N_c	Concentration of clouds
N_g	Concentration of graupel
N_h	Concentration of hail
N_i	Concentration of ice
N_n	Concentration of snow
N_r	Concentration of rain
N_t	Number of time steps during the integration
N_x	Number of grid points in x-direction
N_y	Number of grid points in y-direction
N_z	Number of levels in the vertical

Q	Represent the constant in the C_{LAM} and $C_{cascade}$ computational cost
Q_c	Mass of clouds
Q_g	Mass of graupel
Q_h	Mass of hail
Q_i	Mass of ice
Q_n	Mass of snow
Q_r	Mass of rain
r	*f/Π* ratio of Coriolis parameter to Brunt-Väisälä frequency
rad	radians (standard unit of angular measure)
s	seconds
U	Wind component in x-direction
V	Wind component in y-direction
Δt	Time step
Δx	Grid spacing in x-direction in kilometers
Δx_{eff}	Effective resolution in kilometers
Δy	Grid spacing in y-direction in kilometers
Δz	Vertical grid spacing in kilometers
σ_{KE}^2	Variance of KE
σ_U^2	Variance of U component
σ_V^2	Variance of V component
λ	Wavelength
λ_{max}	Highest wavelength calculated by the DCT
λ_{min}	Lowest wavelength calculated by the DCT

°	Degrees of latitude and longitude
%	Percentage
‘	Minutes de latitude

RÉSUMÉ

Cette étude propose d'appliquer la méthode de télescopage de grille (aussi appelée grilles imbriquées ou cascade) à la 5^{e} génération du Modèle Régional Canadien du Climat (MRCC5) afin d'effectuer un test de faisabilité de ce modèle climatique à très haute résolution. La réduction d'échelle dynamique est appliquée autant de fois que nécessaire afin d'obtenir la résolution horizontale souhaitée, en terme d'espacement entre deux points de grille : de l'ordre de 1 km. Chaque intégration est pilotée par les résultats de la simulation précédente obtenue avec un maillage plus grossier. Il sera démontré que, théoriquement, le coût de calcul de chacune des simulations de la cascade peut être maintenu dans des limites acceptables en réduisant successivement la taille du domaine à aire limitée et en choisissant d'effectuer des simulations épisodiques plutôt que des intégrations continues. En utilisant cette approche, la résolution peut alors être fortement augmentée sans engendrer un coût de calcul trop excessif.

La cascade de cette étude consiste en une suite de cinq simulations ayant des maillages horizontaux de 0.81°, 0.27°, 0.09°, 0.03° et 0.01°. Le domaine d'intérêt couvre essentiellement la vallée du Saint-Laurent, la vallée du Lac Champlain et les reliefs montagneux entourant ces deux vallées (les Appalaches, les Montagnes Vertes, les Montagnes Blanches, les Adirondacks et les Laurentides). La nécessité et la possibilité de simuler les phénomènes météorologiques de petites échelles associés aux reliefs précédents motivent cette étude et ce, dans le but d'éventuellement évaluer leurs impacts sur le climat passé, présent et dans le cadre des changements climatiques.

Une étude des spectres de variance d'énergie cinétique a été effectuée afin d'évaluer le comportement et le développement dynamique des simulations. Les résultats ont montré que les temps d'ajustements des spectres après l'initiation des simulations étaient de moins de 12 heures et que cette durée diminuait au fur et à mesure que la résolution devenait fine. Ce temps d'ajustement des spectres a passé de 12 heures pour la simulation de maillage grossier (0.81°) à 50 minutes pour la simulation de maillage fin (0.01°). Les résolutions effectives, qui représentent la longueur d'onde en dessous de laquelle les spectres sont dynamiquement suspects, ont été approximativement calculées à sept fois l'espacement entre deux points de grille (en kilomètres) pour les simulations de la cascade. La distribution verticale de l'énergie cinétique horizontale donnée par les spectres a montré que l'énergie associée aux

petites (grandes) longueurs d'ondes se situait dans les bas (hauts) niveaux de l'atmosphère. La contribution du raffinement des grilles durant la cascade était surtout perceptible dans les champs de précipitation et de vent, ainsi que par leurs distributions d'intensités. Les champs de précipitation ont montré une augmentation de l'intensité des forts taux de précipitation lorsque la grille était raffinée, une conséquence d'un confinement en bande du champ, d'une diminution de la bruine et d'une augmentation de l'effet de la meilleure définition de la topographie dans le modèle. L'effet de canalisation, qui induit des vents provenant du nord-est durant l'hiver dans la vallée du Saint-Laurent, était de plus en plus perceptible dans les simulations aux fines résolutions horizontales (0.09° et 0.03°, respectivement), alors qu'il était non simulé par les intégrations aux maillages grossiers (0.81° et 0.27°, respectivement). D'ailleurs, une augmentation des fréquences et des intensités des vents près de la surface orientés le long de l'axe de la vallée du Saint-Laurent a été observée par les roses des vents du point de grille le plus près de la ville de Québec pour les simulations avec 0.09° et 0.03° de résolutions horizontales.

Les résultats de cette étude ont non seulement montré la faisabilité de l'application de la cascade au MRCC5, mais aussi des résultats encourageants face à la simulation d'évènements climatiques de grandes importances à l'échelle locale. Cette étude est un premier pas dans la préparation de la prochaine génération de modèles climatiques à très haute résolution.

MOTS-CLÉS : Modélisation Régionale du Climat, Très Haute Résolution, Cascade, Télescopage, Modèle Régional Canadien du Climat

CHAPITRE I

INTRODUCTION

Les Modèles de Circulation Générale (MCGs), aussi connus sous le nom de Modèles du Climat Global, sont les outils les plus fondamentaux en ce qui concerne la modélisation du climat passé, présent et futur à l'échelle globale. Ces modèles mathématiques sont basés sur le système d'équations différentielles couplées de Navier-Stokes découlant de la physique du mouvement des fluides atmosphériques de petites et grandes échelles. Depuis le milieu du 20^{e} siècle, plusieurs centres de recherche sur le climat, de partout dans le monde, ont bâti leur propre MCG. Parmi ces nombreux centres, plusieurs se situent aux Etats-Unis : le *National Center for Atmospheric Research* (NCAR), le *National Oceanic and Atmospheric Administration / Geophysical Fluid Dynamics Laboratory* (NOAA/GFDL), le *National Center for Environmental Prediction* (NCEP), le *Center for Ocean-Land-Atmosphere studies* (COLA) et le *Goddard Institute for Space Studies* (GISS) de la *National Aeronautics and Space Administration* (NASA). D'autres sont localisés en Europe, par exemple en France, il y a l'Institut Pierre Simon Laplace (IPSL) à Paris et le Centre National de Recherches Météorologiques (CNRM) de Météo-France à Toulouse. En Norvège, il y a le *Bjerknes Centre for Climate Research* (BCCR), en Allemagne, le *Max Planck Institute for Meteorology* (MPI), en Italie, le *Centro Euro-Mediterraneo per i Cambiamenti Climatici* (CMCC), en Russie, l'*Institute for Numerical Mathematics* (INM), et, au Royaume-Uni, le *Hadley Centre for Climate*

Prediction and Research (UKMO). Les quatre centres suivants se situent en Chine : le *Beijing Climate Center* (BCC), le *National Key Laboratory of Numerical Modeling for Atmospheric Sciences and Geophysical Fluid Dynamics* (LASG), le *First Institute of Oceanography* (FIO) et le *College of Global Change and Earth System Science* (GCESS). Pour le Japon, il y a le *Meteorological Research Institute* (MRI) et le *Center for Climate System Research* de l'Université de Tokyo (CCSR). En Australie, il existe le *Commonwealth Scientific and Industrial Research Organisation Atmospheric Research* (CSIRO) et, au Canada, il y a le *Canadian Centre for Climate Modelling and Analysis* (CCCma). La plupart de ces centres ont également une division qui se consacre à la Prévision Numérique du Temps (PNT) et les modèles de climat sont souvent basés sur les modèles de prévisions météorologiques.

C'est le couplage des processus océaniques et atmosphériques qui a donné naissance aux premiers Modèles de Circulation Générale proposés par Manabe et Bryan (1969) du GFDL afin de permettre les premières simulations du climat. La composante océanique (OMCG) des MCGs modélise la circulation océanique ainsi que les processus d'échanges entre l'océan et l'atmosphère par le calcul de flux atmosphériques. Les OMCGs contiennent aussi une composante représentant la glace de mer qui intervient de nombreuses façons dans les processus de rétroaction impliquant la radiation atmosphérique et l'albédo de surface. La composante atmosphérique (AMCG) des MCGs consiste, d'une part, en un noyau dynamique qui intègre les équations décrivant l'écoulement atmosphérique et, d'autre part, en un noyau physique qui représente, explicitement ou implicitement, les processus physiques de sous-échelles. Le cœur dynamique des AMCGs résout de manière pronostique la pression de surface, la température, l'humidité (sous forme de vapeur d'eau et parfois d'hydrométéores) et les composantes du vent horizontal pour chaque point de grille à l'horizontale et pour chaque couche à la verticale.

Le tableau 1.1 montre plusieurs MCGs (2e colonne: sauf ceux en bleu), leur centre de recherche respectif (1re colonne), l'évolution des maillages horizontaux (en terme de degré de latitude par degré de longitude) à travers les différentes versions des MCGs (3e colonne) et les références respectives à chaque version (4e colonne). Il est important de faire la différence entre la résolution du modèle et l'espacement entre deux points de la grille. Ces deux termes réfèrent à deux différentes longueurs d'échelles qui caractérisent la configuration de la grille d'un modèle numérique (Grasso, 2000). La résolution indique les échelles pouvant être résolues par le modèle, tandis que l'espacement entre deux points de grille représente la distance moyenne entre des points de grille adjacents pour une même variable (Pielke, 1991). Dans cette étude, l'espacement horizontal entre deux points de grille sera exprimé en kilomètres et parfois en degrés (°) lorsque le terme « résolution horizontale » sera employé.

Au fil du temps et avec un travail continuel de la part des modélisateurs, l'augmentation des ressources computationnelles n'a pas seulement conduit à des meilleures résolutions horizontales, comme le montre la 3e colonne du tableau 1.1, mais aussi à d'autres améliorations, notamment au niveau des différents schémas de paramétrisation inclus dans les AMCGs. Les schémas de paramétrisation sont incorporés dans la physique des AMCGs et servent à représenter de façon implicite les processus qui surviennent à des échelles spatiales de plus petites tailles que la distance entre deux points de grille du modèle (processus de sous-échelles). Les processus physiques non-résolus par les MCGs sont les transferts radiatifs, les interactions avec la surface terrestre, la formation des nuages et la convection. Les schémas radiatifs servent à décrire la représentation du rayonnement solaire d'ondes courtes et de la radiation terrestre d'ondes longues. Les schémas de surface calculent, sous forme de flux, les transferts de chaleur, d'humidité et de quantité de mouvement qui existent entre le sol (et les couches en dessous) et les couches atmosphériques près de la surface. La paramétrisation des nuages est une tâche difficile pour les

modélisateurs, car il existe plusieurs types de nuages dont les processus de formation et de couverture nécessitent des schémas implicites de représentation distincts. Premièrement, il y a les nuages de la couche limite tels que les stratocumulus et les stratus. Deuxièmement, il y a les nuages marqués par la discontinuité entre la couche limite et l'atmosphère libre, comme les petits cumulus non précipitants qui sont induits de la convection peu profonde. Troisièmement, il y a les nuages stratiformes non-convectifs (les stratus, les altostratus et les cirrus) de grandes dimensions spatiales. Finalement, il y a les nuages à grand déploiement vertical provenant de la convection humide profonde : les cumulonimbus et les nimbostratus.

Malgré les complexités associées aux schémas de paramétrisation, comme le calcul des processus physiques ou le couplage des schémas entre eux et avec le modèle, les MCGs ont prouvé leur fiabilité quant à la reproduction du climat passé et présent aux échelles planétaires et continentales. Ils constituent le seul outil pour l'évaluation des conséquences des différents scénarios d'émissions de gaz à effet de serre associés aux changements climatiques tel que démontré dans les récents rapports du Groupe d'experts Intergouvernemental sur l'Évolution du Climat (GIEC). Le GIEC a pour mission d'évaluer toutes les facettes (scientifiques, techniques, socioéconomiques et stratégies d'adaptation) associées aux conséquences des changements climatiques d'origine anthropique sur notre Système Terre (ST). Il existe quatre rapports : le premier était en 1990, le deuxième, en 1995, le troisième, en 2001 et le quatrième, en 2007. Un cinquième rapport (AR5) sera publié en janvier 2014. Pour plus d'informations sur le GIEC consultez le site internet suivant : http://www.ipcc.ch/. C'est avec le couplage des différentes composantes de notre ST (atmosphère, hydrosphère, cryosphère, lithosphère et biosphère) que, depuis les dix dernières années, une nouvelle génération de modèles émerge : les Modèles du Système Terre ou les *Earth System Models* (ESMs; par ex. Hill *et al.*, 2004). À titre d'exemple, les ESMs de certains centres de recherche sont identifiés dans le tableau 1.1 par la couleur bleue. Ces modèles se distinguent des MCGs par l'incorporation de

composantes visant à coupler davantage de processus importants non seulement pour le climat, mais aussi pour l'ensemble du ST. Les ESMs incluent la chimie de l'atmosphère, les processus biogéochimiques des surfaces terrestre et océanique, et une description quantitative des cycles du carbone et de nitrates. Les scientifiques visent à inclure d'autres facettes du ST, comme les interactions avec la terre solide : les mouvements tectoniques, les changements géomorphologiques, les tremblements de terre et les éruptions volcaniques. La figure 1.1 montre les différentes composantes des ESMs (en noir et bleu), les composantes des MCGs (en noir) et les aspects qui ne sont pas encore incorporés dans les ESMs (en vert). Le tableau 1.2 montre les différents modèles (MCGs et ESMs) du tableau 1.1 utilisés pour l'élaboration d'AR5. Pour plus d'information sur AR5 consultez le site internet suivant : http://cmip-pcmdi.llnl.gov/.

Les changements climatiques ont non seulement conduit à un réchauffement mondial, mais aussi à des effets sous-adjacents d'échelles plus locales. Par exemple, il y a les différences régionales occasionnées par les changements de la pression atmosphérique et des vents causés par l'augmentation du niveau moyen des mers. Cette augmentation étant fortement expliquée par la fusion et le retrait des glaciers, la fonte du pergélisol, le rétrécissement des lacs, la diminution de l'écoulement fluvial ainsi qu'une augmentation de la fréquence des coulées de débris et de glissements de terrain. Une intensification de la désertification et une augmentation de la fréquence et de l'intensité des conditions climatiques et météorologiques extrêmes (sècheresse, fortes pluies, grêle, foudre, tempêtes et températures élevées) ont également été observées comme conséquences régionales des changements climatiques (par ex. Wang *et al.*, 2009). Les climatologues ont compris qu'avec les ressources computationnelles restreintes, les MCGs étaient impuissants face à la résolution de la circulation atmosphérique associée à des échelles spatiales locales (par ex. Alexandru *et al.*, 2007; Laprise *et al.*, 2008). En effet, la distance moyenne entre deux points de grille des MCGs varie de 100 à 250 km (soit de 1° à 2.5°) alors que plusieurs

processus régionaux se produisent à des échelles spatiales de 50 km et moins. Il serait certes possible de simuler le climat avec des MCGs de fines résolutions horizontales (~10 km ou 0.1°), toutefois le coût informatique associé à de telles intégrations serait déraisonnable.

C'est ainsi que, dans les années 1980, une alternative aux MCGs, qui avaient alors des maillages horizontaux de 3° à 5° (espacement entre deux points de grille de 300 à 500 km), a été proposée. Cette alternative se base sur le concept de la mise à l'échelle dynamique, il s'agit des Modèles Régionaux du Climat (MRCs; Dickinson *et al.*, 1989; Giorgi et Bates, 1989) qui découlent directement des Modèles à Aire Limitée (LAMs) utilisés en PNT. Les domaines des MRCs sont restreints à des zones ciblées et leurs frontières latérales sont contrôlées par des variables de pilotage provenant d'un MCG, d'un autre MRC ou de réanalyses ayant des maillages horizontaux plus grossiers. La technique de la mise à l'échelle dynamique stipule qu'au fur et à mesure que les variables de résolutions grossières des Conditions aux Frontières Latérales (CFLs) entrent dans le domaine du LAM, ce dernier est apte à développer les phénomènes de plus petites échelles associés à la meilleure résolution de la grille du LAM (Giorgi et Bates, 1989). L'ensemble de base des CFLs contient la température, l'humidité spécifique, la pression de surface et les vents horizontaux. Ces variables sont ensuite interpolées à l'horizontale et à la verticale sur la grille du LAM afin de guider la solution à l'intérieur du domaine. Une zone d'ajustement de quelques points de grille autour du LAM est nécessaire afin de réduire au maximum les artéfacts numériques créés par les CFLs (Davies, 1976). Il est souvent observé que les erreurs contenues dans les données pilotes (CFLs) sont transférées dans la solution du LAM toutefois, l'utilisation d'une même base physique et dynamique entre le modèle pilote et le LAM semble réduire l'effet du transport de l'erreur en limitant les apports qui viennent des différentes configurations des deux modèles (par ex. Diaconescu *et al.*, 2007). La taille du domaine est aussi une caractéristique importante durant la mise à l'échelle dynamique : elle doit être assez petite afin de ne pas diverger du pilotage et

assez grande pour permettre le développement des fines échelles du modèle (Jones *et al.*, 1995; Leduc et Laprise, 2009). La résolution horizontale des MRCs utilisée jusqu'à récemment se situe autour de 50 km. Le tableau 1.3 montre les MRCs (1re colonne) des différents centres de recherches (2e colonne) et certaines de leurs caractéristiques générales telles que l'espacement entre deux points de grille horizontaux (3e colonne), le nombre de niveaux à la verticale (4e colonne) et le nombre de points de grille dans la zone d'ajustement des CFLs (5e colonne). Plusieurs de ces modèles ont l'implantation du mode non-hydrostatique (6e colonne, ceux marqués d'un « oui ») et permettent ainsi des simulations avec des résolutions horizontales très raffinées (< 0.1°). Le mode non-hydrostatique consiste en l'abandon de l'approximation hydrostatique qui négligait le terme de l'accélération verticale dans les équations qui régissent le modèle. Plus de détails concernant cette technique et ces conséquences sur les équations du modèle sont présentés dans l'article de Yeh *et al.* (2002) qui est concentré sur l'implantation du mode non-hydrostatique au *Global Environmental Multiscale Model* (GEM; Côté *et al.*, 1998a, 1998b).

Bien que par l'augmentation de la résolution horizontale, les MRCs améliorent la représentation de plusieurs aspects climatologiques régionaux importants (définition des montagnes, des lacs et des estuaires), la présence de schémas de paramétrisation est toujours requise. Le tableau 1.4 montre les différentes configurations des schémas de paramétrisation (surface, couche limite, radiation et convection, présentés dans les 2e, 3e, 4e, et 5e colonnes, respectivement) pour les mêmes MRCs du tableau 1.3. Avec la variété de schémas illustrée dans le tableau 1.4, il arrive que plusieurs possibilités de configuration (couplage de schémas) soient disponibles pour un même MRC. Par le fait même, des changements significatifs dans la paramétrisation physique entre les différentes versions d'un même modèle peuvent survenir, comme le montre les rangées 11 et 12 des tableaux 1.3 et 1.4 pour les différentes configurations entre la 4e et la 5e génération du Modèle Régional Canadien du Climat (MRCC). Les MRCs sont devenus des outils sophistiqués pour la simulation du climat présent et les projections

à long terme du climat futur sur des domaines limités et avec des maillages horizontaux variant entre 0.25° et 0.5°. Par exemple, le principal objectif du projet PRUDENCE (Christensen et Christensen, 2007) était de fournir, par une étude d'ensemble de MRCs, différents scénarios des changements climatiques sur l'Europe pour la fin du 21^{e} siècle. Les MRCs ont d'abord subit une première mise à l'échelle dynamique de 0.5° de résolution horizontale et quelques modèles ont également effectué une deuxième mise à l'échelle de 0.2°. D'autres projets évoluent en parallèle en employant différents MRCs afin de fournir des informations semblables sur les différents scénarios des changements climatiques pour d'autres régions du globe. Par exemple, il y a NARCCAP (Mearns *et al.*, 2009) sur l'Amérique du Nord, ARCMIP (Curry et Lynch, 2002) sur l'Arctique, CLARIS (Marengo et Ambrizzi, 2006) sur l'Amérique du Sud et RMIP (Fu *et al.*, 2005) sur l'Asie. Le projet ENSEMBLES (Hewitt, 2005) est principalement concentré sur l'Europe et le projet CORDEX (Jones *et al.*, 2011) sur plusieurs régions du monde avec l'Afrique comme région focale. Les MRCs du tableau 1.3 utilisés lors de ces différents projets sont marqués d'un « X » dans le tableau 1.5 (voir liste des acronymes pour les noms des projets).

Même avec des résolutions horizontales beaucoup plus fines que les MCGs, certains problèmes persistent et plusieurs processus physiques tels que le cycle hydrologique et les évènements extrêmes du climat (la précipitation intense, les différents types de précipitation et la convection) ne sont toujours pas résolus explicitement par les MRCs. Avec l'implantation du mode non-hydrostatique dans certains MRCs, des intégrations climatiques de très haute résolution ($< 0.1°$) deviennent possibles. Toutefois, à cause des ressources computationnelles restreintes, de telles intégrations nécessitent le développement de méthodes particulières par le biais de certains compromis. L'utilisation d'un MRC à des résolutions horizontales plus fines que 0.15° ($\sim$ 15 km) est encore relativement rare.

C'est dans le but de préparer la nouvelle génération de MRCs à très haute résolution que cette étude propose d'appliquer la méthode de télescopage (aussi appelée cascade ou grilles imbriquées; cf. Hill, 1968) à la 5^{e} génération du Modèle Régional Canadien du Climat (MRCC5; Hernández-Díaz *et al.*, 2012). Le MRCC5 a été développé au Centre ESCER (Centre pour l'Étude et la Simulation du Climat à l'Échelle Régionale) de l'Université du Québec à Montréal (UQAM). La méthode de cascade est fréquemment employée dans le cadre des PNTs de très courte durée et s'appuie sur le concept d'une série de mise à l'échelle dynamique de simulations imbriquées. Une première simulation de résolution grossière sert de CFLs pour la simulation suivante ayant un domaine imbriqué dans celui de la première simulation et avec une résolution horizontale plus fine. Cette deuxième simulation sert, à son tour, de pilotage pour une troisième imbrication de résolution encore plus fine et ainsi de suite, jusqu'à atteindre la fine résolution horizontale souhaitée. Dans cette étude, un maillage de 0.01° sera atteint, soit d'environ 1 km.

Les besoins et les possibilités d'augmenter la précision des simulations climatiques par le biais de résolutions horizontales de plus en plus fines motivent cette étude. En effet, une fine résolution implique une meilleure définition de la topographie dans le modèle et, par le fait même, une meilleure simulation directe de tous les phénomènes se rattachant aux effets de surface. Par exemple, la très fine résolution permettrait d'envisager la simulation des conditions météorologiques nécessaires à la formation et à la persistance de la pluie verglaçante. Certaines études suggèrent que la combinaison de vents de surface du nord-est dans la vallée du Saint-Laurent et de vents du sud en altitude serait nécessaire à la formation et à la persistance de la pluie verglaçante (Laflamme et Périard, 1998; Stuart et Isaac, 1999; Cortinas, 2000; Cortinas Jr. *et al.*, 2004). Ainsi, pour permettre une étude de l'occurrence des pluies verglaçantes dans la vallée du Saint-Laurent, les modèles climatiques doivent avoir une résolution assez fine pour permettre la simulation des vents de canalisation qui sont causés par la topographie régionale.

Organisation du mémoire

Suite à cette introduction, un article rédigé en anglais correspondra au chapitre II de ce mémoire. Cet article comprendra tout d'abord l'Introduction (Section 2.1) dans laquelle une revue de la littérature et le contexte scientifique du sujet de cette étude seront présentés. Puis, il y aura la Méthodologie (Section 2.2) qui décrira l'implication et la configuration de l'application de la méthode de cascade au MRCC5. Suivi de la présentation des Résultats (Section 2.3) qui sera concentrée sur l'analyse de deux champs dynamiques (vents horizontaux et énergie cinétique) et d'un champ physique (la précipitation). Finalement, un résumé et les conclusions de cet article seront formulés dans la Section 2.4. Le chapitre III correspondra aux conclusions de ce mémoire et le chapitre IV, aux références.

CHAPITRE II

MÉTHODE DE TÉLESCOPAGE APPLIQUÉE AU MODÈLE RÉGIONAL CANADIEN DU CLIMAT (MRCC5) POUR UNE ÉTUDE DE FAISABILITÉ DE CE MODÈLE À TRÈS HAUTE RÉSOLUTION

Comme mentionné plus haut, ce chapitre est présenté sous forme d'un article scientifique rédigé en anglais. Les parties *Introduction* et *Methodology* présenteront les motivations et la description de la méthode de cascade. La troisième partie (*Results*) correspondra à l'élaboration et la discussion des résultats obtenus lors de l'étude et la dernière partie (*Conclusions*) sera une brève conclusion des points essentiels soulevés dans cet article.

FEASIBILITY STUDY OF A VERY HIGH RESOLUTION REGIONAL CLIMATE MODEL BY THE APPLICATION OF THE GRID TELESCOPING METHOD TO THE CANADIAN REGIONAL CLIMATE MODEL (CRCM5)

by

Mélissa Cholette and René Laprise

Centre ESCER, Université du Québec à Montréal

To be submitted to Climate Dynamics

Corresponding author adress:

Mélissa Cholette

Centre ESCER, Département des Sciences de la Terre et de l'Atmosphère, UQAM

BP 8888, Succ. Centre-ville

Montréal (Québec) Canada, H2H 2J2

e-mail: cholette.melissa.2@gmail.com

Abstract

Nested Regional Climate Models have become sophisticated tools for climate simulations. With grid spacing generally around 25 to 50 km, many physical processes can be explicitly resolved compared to coarser General Circulation Models using grid spacing between 100 to 250 km. Then, Regional Climate Models lead to better representation of some high-impact weather phenomena such as intense precipitation and orographic effects. Yet several climate impact applications call for much higher resolution.

This study proposes to apply the grid telescoping method (or cascade) to the fifth generation Canadian Regional Climate Model for a feasibility study of achieving very high-resolution climate simulations on grid mesh of the order of 1 km. The cascade consists in a suite of five one-way nested simulations with grid spacing varying roughly from 81 km successively to 27, 9, 3 and finally 1 km (spatial resolutions of 0.81°, 0.27°, 0.09°, 0.03° and 0.01°, respectively). To maintain reasonable computational resources requirements, the length of the integrations are successively reduced by the same factor of three as the grid spacing decreases.

The results are analysed in terms of precipitation and wind intensity/frequency distributions, showing a definite advantage of using very high-resolution meshes. Kinetic energy spectra are also computed to study the spin-up times and the effective resolutions as a function of the various simulations' grid spacing. The results of this study tend to support the fact that very high-resolution climate simulations could soon become operationally feasible.

Keywords: Regional Climate Modelling – Very High Resolution – Cascade – Grid Telescoping – Canadian Regional Climate Model

2.1 Introduction

Vilhelm Bjerknes was the first to consider weather forecasting as the principal objective for meteorological researchers. He suggested that weather forecasting should be considered as an initial value problem of mathematical physics: starting from observed initial state of the atmosphere, forecasts could be carried out by integrating the governing equations forward in time. Even with the trust of the emerging computers accessibility, the lack of suitable computing facilities at that time (in 1895) did not allow solving such calculations as envisioned (http://earthobservatory.nasa.gov/Features/Bjerknes/bjerknes_2.php).

The first computer models to be able to solve the atmospheric flow based on the quasi-geostrophic vorticity equation came with the pioneering work of Charney and Phillips (1953). The atmospheric simulations have since evolved with increasing the model's performance and the numerical solutions while using the best of the computational resources available. In 1965, Manabe's pioneers group, from the United States Weather Bureau (renamed the Geophysical Fluid Dynamics Laboratory in 1963), assembled a reasonably complete three-dimensional global model that solved the so-called primitive equations for an atmosphere divided into nine vertical levels (Manabe *et al.*, 1965). They were the first to couple the oceanic and the atmospheric components (Manabe and Bryan, 1969) to evaluate the effects of doubling the atmospheric CO_2 concentration on the future climate (Manabe and Wetherald, 1975) while using a General Circulation Model (GCM). Today's GCMs, also known has Global Climate Models, couple atmospheric, oceanic and land-surface components, and sometimes biogeochemistry processes. The GCMs have proved their reliability to reproduce the past and present climates, and constitute the primary tools for making projections of future climate as a result of anthropogenic effects (Intergovernmental Panel on Climate Change; Parry *et al.*, 2007). Owing to their tantamount computational cost resulting from their complex formulations, the need to carry multi-century long to achieve dynamic equilibrium and the need to

obtain statistical significance with ensemble simulations, GCMs employ coarse resolutions, too coarse for most regional climate-change impacts studies (Grotch, 1988; Mearns *et al.*, 1990; Giorgi and Coppola, 2010). Operational GCMs employ meshes with grid spacing varying between 100 and 250 km thus precluding the resolution of mesoscale processes. Reducing the grid spacing of GCMs is still too prohibitive because of insufficient available computational resources for most research centres.

An alternative approach was proposed in the late 1980s: nested Regional Climate Models (RCMs; Dickinson *et al.*, 1989; Giorgi, 1990), also known in Numerical Weather Prediction (NWP) as Limited-Area Models (LAMs). Based on the concept of dynamical downscaling, the LAM domain is restricted to a study region (typically the size of a continent) and the lateral boundary conditions (LBCs) are provided by coarser resolution model. Over the past two decades, RCMs have become sophisticated tools for the present-day simulations and long-term projections of future climate. Many regional processes can be well resolved with typical RCMs' grid spacing around 25 to 50 km. However, the horizontal resolution still too coarse for proper representation of important weather and climate features that may have direct impacts on human society and ecosystems. With the need to produce higher spatial resolution climate integrations, a very recent method has been employed in NWP and is called the grid telescoping or cascade (Hill, 1968; Chen and Miyakoda, 1974; Hart *et al.*, 2005; Lean *et al.*, 2008; Rife *et al.*, 2009; Mailhot *et al.*, 2012). The cascade is based on a suite of dynamical downscaling nested grid simulations with larger domain simulation using coarse spatial resolution and smaller domain simulations successively employing finer horizontal resolution. Each new domain of the cascade uses LBCs provided by the closest coarser spatial resolution simulation's outputs. This method is permitted with the implementation of the non-hydrostatic mode in certain RCMs and allows very high-resolution climate integrations (grid spacing < 10 km).

Recent projects have been developed to apply the grid telescoping method to climate models. For example, Trapp *et al.* (2007) have tested two telescoping methods investigating the possible changes in the frequency, the intensity and the geographical distribution of severe historical extreme convective precipitating storms. For the first cascade, the National Centers for Environmental Prediction and the National Center for Atmospheric Research (NCEP-NCAR) Reanalysis Project (NNRP; Kalnay *et al.*, 1996), data available at 2.5° of latitude/longitude resolution, is used to drive the 55-km grid spacing hydrostatic International Centre for Theoretical Physics Regional (ICTP) Climate Model, version 3 (RegCM3; Pal *et al.*, 2007). The 55-km RegCM3 results are then used to drive the 27-km grid spacing Weather Research and Forecasting model (WRF; Skamarock and Klemp, 2008). To finish the first telescoping, the 27-km WRF provides LBCs for the 9-km WRF, which in turn drives the 3-km convection-permitting WRF for two different periods of 30 hours. The second telescoping method uses the 27-km WRF, directly driven by the NNRP data, for the same following cascade to 9-km WRF and to 3-km convection-permitting WRF. The domain of RegCM3 covers the entire United State continent and is reduced successively to cover approximately the width of a single state (Indiana and North Texas States) in the 3-km WRF. The solutions of the first method were inferior to those from the second method, due to the large sensitivity of the WRF location within the RegCM3 domain. This study showed the ability of the two telescoping methods (especially the second one) to investigate convective precipitation storms. The success seems to reside in the good representation of the large-scale features provided by LBCs and in the skill to develop finer scales.

A very recent study at the Institute for Atmospheric and Climate Science (Swiss Federal Institute of Technology of Zurich) uses the non-hydrostatic version of the Consortium for Small-scale Modeling Climate Limited-area Model (COSMO-CLM version 4.14; Doms *et al.*, 2005) to evaluate a ten-year (1998-2007) cloud-resolving climate integration. The Interim reanalysis (ERA-Interim; Simmons *et al.*, 2007),

developed at the European Centre for Medium-Range Weather Forecasts (ECMWF), are used to drive the 12-km grid spacing COSMO-CLM. Next, the 12-km COSMO-CLM provides LBCs for the 2.2-km COSMO-CLM cloud-resolving model. Differences in temperature and precipitation fields' biases between the 12-km and the 2.2-km simulations are found to be comparatively small for both summer and winter seasons. However, the 2.2-km integration improves the simulation of the timing summer convection and captures quite well the extreme precipitation, while the 12-km simulation underestimates the frequency and the intensity of extreme precipitation (Ban *et al.*, 2013).

Another cascade method is employed in the NCAR Nested Regional Climate Model project (NRCM; Done *et al.*, 2012). NRCM combines the dynamic of the WRF model and the subgrid-scale parameterizations of the Community Climate System Model (CCSM; Collins *et al.*, 2005). The 36-km horizontal grid spacing NRCM, driven by the NNRP data, provides LBCs to the 12-km NRCM. The simulations are performed over the North Atlantic to study the tropical cyclones climate variability and changes over two future periods (2020-2030 and 2045-2055). The results showed that the 36-km simulation cannot resolved well intense hurricanes, while the 12-km simulation is more accurate for the representation of the observed number of storms' tracks (27 observed storms, 28 simulated storms for 12-km and 18 simulated storms for 36-km). The third step of the cascade is a 4-km NRCM simulation driven by the 12-km simulation outputs; however the analysis of the 4-km results is not yet available at the time of writing (Done *et al.*, 2012).

Finally, the Wegener Center of the University of Graz in Austria coordinated the Local Climate Model Intercomparison Project (LocMIP; Prein *et al.*, 2011) for a very high-resolution RCMs intercomparison study. The grid telescoping is applied to four different climate models: two versions of the COSMO-CLM (4.0 and 4.8), the WRF climate model version 2.2.1 (Skamarock *et al.*, 2005) and the fifth-generation

Pennsylvania State University/NCAR Mesoscale Model version 3.7.4 (MM5; Grell *et al.*, 1994). Climate cascades were performed with these four models for two periods (June-July-August 2007 and December-January-February 2007-2008) in the Austrian Alps region. The Integrated Forecasting System (IFS; Gregory *et al.*, 2000) analyses of 25-km grid mesh (provided by ECMWF) furnish LBCs to the three 10-km grid spacing models. The 10-km models' outputs were then used to drive the non-hydrostatic 3-km simulations, which in turn, drove the non-hydrostatic 1-km simulations. Two domains are evaluated in the Alps region, one in a mountainous orography and the other in a valley region. This group benefited from the Integrated Nowcasting through Comprehensive Analysis (INCA; Haiden *et al.*, 2011) on 1-km mesh consisting in a combination of NWP and observations from the Central Institute for Meteorology and Geodynamics to compare their very high-resolution simulations with. They evaluated principally four variables (temperature, relative humidity, precipitation and global radiation) in three different ways (mean climate, spatial and temporal features). In general, they noted an overestimation in the mountainous regions and an underestimation in the valley regions of the precipitation field with the increasing spatial resolution. They also observed an increase of the mean precipitation biases due to the explicitly resolved convection at 3-km and 1-km grid spacing. They conclude that there are larger differences between the different models than between the resolutions' steps of each model cascade.

The results of these last studies are encouraging for very high-resolution climate models using telescoping method. However, the climate modelling at horizontal grid spacing between 1 km and 10 km is far from being established and no systematic intercomparison or evaluation of non-hydrostatic RCMs has been conducted so far (except for LocMIP). The overall goal of this study is to apply the cascade method to the fifth generation non-hydrostatic version of the Canadian Regional Climate Model (CRCM5; Zadra *et al.*, 2008; Hernández-Díaz *et al.*, 2012) to make a feasibility study of this very high-resolution model. It may be a preparation for the next generation of

very fine-scale resolving climate integrations. Climate simulations at fine-resolving scales have the main advantage to resolve the topography and the surface fields more accurately than coarser RCMs. In fact, in NWP, cloud-resolving integrations have already proven to yield a more realistic precipitation pattern and especially over an orographically complex areas (Mass *et al.*, 2002). For example, the very fine resolution simulation would consider the simulation of the needed meteorological conditions for the formation and the duration of freezing rain. The freezing rain in a valley region is almost caused by the channelling effect caused by the detailed topography. Thereby, climate occurrence studies of such high-impact weather phenomena should be permitted with very high-resolution simulations. However, significant obstacles exist with high-resolution regional climate simulations. Indeed, there exists no adequate evaluation dataset due to poor availability of suitable observations. There are also the restricting factors associated with the limited computational resources and storage capacity. The major obstacle is the complexity of the parameterization of the ensemble effect of subgrid-scale physical processes. In fact, the parameterizations used by climate models are typically built for grid spacing coarser than 25 km and the spatial resolution at which some schemes have to be modified (e.g. turned off) is not clear yet. It may be somewhat premature now to launch long-term simulations of past and future climates at local scales, but there is belief that in some near future, long-term climate integrations at grid spacing less than 4 km might become a standard.

This paper is organised as follows. The methodology (Section 2.2) presents the CRCM5 cascade pragmatic consideration (sub-Section 2.2.1) and configuration (grids description, time characteristics, parameterizations and lateral boundary conditions; sub-Section 2.2.2). Results are presented in Section 2.3 and separated in three sub-Sections. The first one (sub-Section 2.3.1) is the dynamical wind fields' analysis with intensity/frequency/direction diagrams. The second part (sub-Section 2.3.2) of the results is the computation and the dynamical evaluation of the kinetic energy variance

spectra using spin-up times and effective resolutions. The last results' sub-Section (2.3.3) is concentrated on the physical analysis of the cascade precipitation fields and their related intensity distributions. Finally a summary of the findings and conclusions are presented in Section 2.4.

2.2 Methodology

Professor René Laprise at the University of Québec in Montréal initiated the development of the first-generation Canadian Regional Climate Model (CRCM; Laprise *et al.*, 1997). The fifth-generation CRCM (CRCM5; Hernández-Díaz *et al.*, 2012) is based on the Canada Global Environment Multiscale (GEM; Côté *et al.*, 1998a, 1998b) model in its LAM version (Zadra *et al.*, 2008). The model GEM uses a two-time-level implicit semi-Lagrangian marching scheme with a horizontal discretization based on an Arakawa staggered C-grid and a terrain-following hydrostatic-pressure vertical coordinate (Laprise, 1992). Yeh *et al.* (2002) implemented a fully elastic non-hydrostatic option in the LAM mode of the CRCM5. Dropping the hydrostatic approximation allows proper consideration of the vertical acceleration terms in the equations that govern the model. Most CRCM5 subgrid-scale physical parameterizations (radiation scheme, surface scheme, convection schemes and condensation scheme) have been taken from a combination of Meso-Global and Regional (15-km grid spacing) modules. The cascade of this study consists in a suite of five one-way nested CRCM5 simulations with horizontal mesh of 0.81°, 0.27°, 0.09°, 0.03° and 0.01° (roughly grid spacing of 81 km, 27 km, 9 km, 3 km and 1 km, respectively). Before describing the CRCM5 cascade configuration, pragmatic consideration associated with the grid telescoping method will be discussed.

2.2.1 A Pragmatic Consideration: the Cascade Computational Cost

The main objective of the grid telescoping is to obtain very high-resolution climate integrations while maintaining reasonable computational resources requirements. Let's start with the GCM computing time, which can be expressed as:

$$C_{GCM} = K * N_x * N_y * N_z * N_t \quad (2.1)$$

where C_{GCM} is the computing time (hereinafter simply referred to as the cost), K is the average cost per grid point, N_x and N_y are the numbers of grid points along the horizontal x- and y-axis, respectively, N_z is the number of vertical levels and N_t is the number of time steps required to complete the simulation. K is a complex function of the hardware, software and complexity of the model. Hardware considerations, such as processor's speed, architecture and degree of parallelism, are of paramount importance to establish the cost. The software, such as the optimisation of the code for a given architecture and the choice of the numerical algorithms to discretize the equations (e.g. explicit Vs implicit, Eulerian Vs semi-Lagrangian) can significantly influence the cost. The complexities of the model, such as whether the model fully couples the atmosphere to the ocean, the details of the land-surface representation and the parameterization of the subgrid-scale processes can also considerably affect the cost of the model. The time needed for reading the inputs variables and for writing the archives of the simulated climate variables is another important factor in the computing cost.

The numbers of grid points N_x and N_y are directly linked to the horizontal grid spacing (Δx and Δy) and to the horizontal dimensions of the domain (L_x and L_y). Similarly, N_z is associated to the vertical grid spacing (Δz) via the height of the computational domain (L_z), and finally N_t is connected to the time step (Δt) and the length of the simulation (L_t). The relation of these associations is:

$$\Delta i = \frac{L_i}{N_i} \tag{2.2}$$

where $i = \{x,y,z,t\}$. Uniform horizontal grid spacing is assumed subsequently for simplicity ($\Delta x = \Delta y$) and hence the cost of a GCM can be expressed as:

$$C_{GCM} = K \frac{L_x}{\Delta x} \frac{L_y}{\Delta x} \frac{L_z}{\Delta z} \frac{L_t}{\Delta t} \tag{2.3}$$

Once Δx is fixed, there are physical and numerical constraints on Δz and Δt. Lindzen and Fox-Rabinowitz (1989) have shown that consistency is necessary between Δx and Δz. At synoptic scales, the following condition should be respected:

$$\frac{\Delta z}{\Delta x} \approx \frac{f}{\Pi} \tag{2.4}$$

where f and Π are respectively the Coriolis parameter and the Brunt-Väisälä frequency. At convective scales, isotropy of the mesh is desirable:

$$\frac{\Delta z}{\Delta x} = 1 \tag{2.5}$$

In the following, we will take for generality $\Delta z = r\Delta x$, in which r =1 for convective scales and $r = f/\Pi$ for synoptic scales. Often however, these constraints are not respected in practice, especially at synoptic scales. The time step must respect constraints as well. The Courant-Friedrichs-Lewy non-dimensional number is defined as:

$$C_{FL} = \frac{U\,\Delta t}{\Delta x} \tag{2.6}$$

In explicit Eulerian schemes, U is the sum of the maximum wind speed and the phase speed of the fastest waves, while in implicit Eulerian schemes, U is the maximum wind speed only. In Eulerian time marching schemes, numerical stability requires that

$C_{FL} \leq 1$, while semi-Lagrangian transport schemes can greatly relax this condition to $C_{FL} \leq 5$ (Robert, 1981). In the following, we will consider for generality that the time step is $\Delta t = C_{FL}\, \Delta x / U$, where C_{FL} is a quantity of an order of 1. Replacing the constraints on Δz and Δt in the cost equation (2.3), we obtain:

$$C_{GCM} = \frac{K\, L_x L_y L_z\, U\, L_t}{r\, C_{FL}} \frac{1}{\Delta x^4} \tag{2.7}$$

For given software, computer hardware and meteorological regime, parameters K, r and C_{FL} are not under the direct control of the user. For a GCM, the horizontal domain (L_x x L_y) covers the entire globe, L_z is heavily constrained to cover the troposphere and at least the lower stratosphere, and the length of simulation is an order of several decades for statistical significance of the simulated results. Hence, the cost is inversely proportional to the fourth power of the horizontal grid spacing. As mentioned before, the condition on Δz is not always respected, in that case, N_z and Δz can be fixed arbitrarily and the cost becomes an inverse function of the third power of the grid spacing:

$$C_{GCM} = \frac{K\, L_x L_y N_z\, U\, L_t}{C_{FL}} \frac{1}{\Delta x^3} \tag{2.8}$$

The above considerations pertain to a GCM. Considering now the LAM cascade case, the choice of the domain size (L_x and L_y) becomes under the control of the user and if one chooses to maintain the same number of horizontal grid points ($N_x = N_y$) between each simulation (accept to reducing the domain size as the grid spacing becomes finer), then the cost of one integration in the cascade becomes inversely proportional to the first power of the grid spacing:

$$C_{LAM} = \frac{K\, N_x N_y N_z\, U}{C_{FL}} \frac{L_t}{\Delta x} \tag{2.9}$$

Under the above assumptions, the cost of an RCM simulation varies only due to the changing parameters L_t and Δx. If furthermore the period of integration is diminished by the same factor as the grid spacing, the ratio $L_t/\Delta x$ remains constant:

$$C_{LAM} = Q \tag{2.10}$$

with,

$$Q = \frac{K\ U\ N_z L_t N_x^2}{C_{FL}\ \Delta x} \tag{2.11}$$

Obviously, the costs of the intermediate integrations contribute to the total cost of the cascade:

$$C_{cascade} = \eta\ Q \tag{2.12}$$

where η is the total number of steps during the telescoping. It is important to recall that equation (2.12) is obtained under the assumption that K, U and C_{FL} are invariant as a function of resolution, and with the constraint that N_z, N_y, N_x and ratio $L_t/\Delta x$ are kept the same for all simulations of the cascade, i.e. reducing the domain sizes and the integration periods by the same factor as the grid spacing is decreasing.

Statistical significance is, of course, an important issue when the length of simulations is involved. For example, considering a 30-years period as a canonical minimal period for a general circulation in the atmosphere and assuming that one were to make cascade of simulations ranging from 81 km to 1 km by steps of three (five simulations). Maintaining a constant ratio of $L_t/\Delta x$ would imply that the 1-km simulation period should be 135 days long. If one accepts to only activate the 1-km simulation for episodes of interests (e.g. frontal passages) of one-day period at a time (i.e. L_t (Δx = 1 km) =1 day), this means that 135 such episodes could be simulated at very high resolution. Given that the episodes could be chosen to be associated to a diversity of synoptic conditions and would be independent of one another, 135 would

appear a reasonable number to obtain statistical significance of the simulated high-impact weather event of interest.

2.2.2 The CRCM5 Cascade Configuration

All information described in Section 2.2.2 is summarized in the table 2.1, where the columns correspond to the five simulations of the cascade and the rows are the different types of configuration, which correspond to the different sub-Sections (2.2.2.1 to 2.2.2.4) in the text.

2.2.2.1 Grids Description

As mentioned before, a suite of CRCM5 simulations is performed with horizontal grid mesh of 0.81°, 0.27°, 0.09°, 0.03° and 0.01° (hereinafter referred to as d81, d27, d9, d3 and d1, respectively). The domains are square and centred on Montréal, Canada (45°30'N, 73°35'W), as shown the figure 2.1. The d81 simulation has 200 x 200 grid points in the horizontal and the four other simulations (d27, d9, d3 and d1) have roughly the same number of horizontal grid points: 225 x 225. The sponge zone (Davies, 1976) is 10 points around the perimeter of the domains and all simulations use 56 levels in the vertical.

As the resolution is becoming finer, the representation of the topography in the model is more complex (as shown the grey tones in figure 2.1) and the surface can exerts a larger influence on the atmospheric flow. Several climatological fields can be influenced thermally or dynamically by the presence of mountains or valleys and the representation of orography in the model becomes very important. Figure 2.2 shows that the d3's region is essentially covering the St-Lawrence River Valley (SLRV) with the Laurentian Mountains to the northwest and the Appalachians to the

southeast. The d3 domain also covers a part of the Lake Champlain Valley (LCV) with the Adirondacks on the west side and the Green Mountains on the east side. More specifically, the SLRV is a southwest-northeast oriented valley starting from Lake Ontario, passing through Montréal City (red point in figure 2.2), Québec City (blue point in figure 2.2) and ending in the St-Lawrence Gulf. The LCV is a north-south valley extending from the border of New York State to the Hudson River Valley. The mean width of SLRV is 50 km, ranging from 3 km near Québec City to 90 km near Montréal, while the mean width of LCV is roughly 30 km.

2.2.2.2 Time Characteristics

The model's time steps are 30 min, 10 min, 200 s, 60 s and 20 s for d81, d27, d9, d3 and d1, respectively, corresponding to roughly the same C_{FL} numbers (assuming U is roughly the same for the five simulations). The lengths of the integrations are 6 months, 4 months, 3 months, 1 month and 15 continuous days for d81, d27, d9, d3 and d1, respectively. The respective dates are identified in table 2.1 and the 15 days of the common period are from 0000 UTC 12 February to 0000 UTC 1 March 2002. Clearly statistical significance will not be achieved with such short simulation period and it does not correspond to a constant $L_f/\Delta x$ ratio. The mean reason is because this study aims at demonstrating the feasibility of the proposed approach rather than the validation of the simulated results and technique experimentation is desired. Winter period is chosen to reduce potential issues related to deep convection, as deep convection is less active in winter period over the study domain. The archival time intervals are modified from a simulation to another to be consistent with the required intervals of the LBCs (to be discussed later); the archival time intervals are 3 h for d81 and d27, 1 h for d9, 20 min for d3 and 5 min for d1.

2.2.2.3 Parameterizations

Parameterizations are used to represent the average effect of the subgrid-scale processes such as turbulence, cloud, microphysics and convection, in terms of the model prognostic variables. In principle, a refinement of the model resolution should be accompanied by certain adaptations of the parameterization schemes and their parameters. In practice however, some components of the parameterizations are less sensitive than others and do not require changes over a wide range of scales. For example, the representation of the heat, moisture and momentum fluxes between the land surface and the atmosphere is robust over a very wide range of resolutions, then the CRCM5 uses the Canadian Land Surface Scheme version 3.5 (CLASS3.5; Verseghy, 2000, 2008) for all simulations of the cascade. The terrestrial and solar radiation transfers are formulated in terms of correlated-K radiation scheme (CKRS; Li and Barker, 2005) for all simulations. Also, there exist four distinct schemes to represent four different types of clouds in the CRCM5. The first scheme is MOISTKE (Tiedtke, 1989; Benoit *et al.*, 1989), this scheme is used to represent the boundary-layer clouds including stratocumulus and stratus. The second cloud scheme represents the top of the atmospheric boundary layer (small cumulus, altocumulus and altostratus), which corresponds to an unresolved discontinuity in climate models and hence, the uplift of the mixed-layer humidity has to be parameterized by a shallow-convection cloud scheme (KSCCS; Kuo, 1965; Bélair *et al.*, 2005). All these last parameterization components (CLASS3.5, CKRS, MOISTKE and KSCCS) remain unchanged during each simulation of the cascade.

However, as the grid spacing diminishes, there are some processes that become explicitly resolved and it is not necessary to parameterize them anymore. The hydrostatic d81, d27 and d9 simulations use the diagnostic condensation scheme (CONSUN; Sundqvist *et al.*, 1989) that represents the third type of clouds (stratiform or non-convective clouds) for large-scales precipitation. As opposite, the d3 and d1 are non-hydrostatic simulations and use the double-moment bulk microphysics

scheme (MYDM; Milbrandt and Yau, 2005a, 2005b). The prognostic condensation scheme (MYDM) is responsible for the release of latent heat associated with the cloud and precipitation formation. The Milbrandt and Yau microphysics scheme provides detailed information on the different types of precipitation (snow, rain, graupel and hail), while in the Sundqvist scheme, the precipitation type is diagnosed via an empirical algorithm (bourge 3D) developed by Bourgouin (2000). Deep moist convection gives rise to the fourth type of clouds, an important issue with high-resolution modelling. In fact, using convective parameterization schemes at fine scales can violate some hypotheses and assumptions that are at the base of those schemes (Arakawa and Chen, 1987; Molinari and Dudek, 1992). Convective parameterization is used to predict the collective effects of many convective clouds (cumulonimbus and nimbostratus) that may exist in the grid as a function of large-scale processes and, conversely, the predicted convective precipitation consists in a direct feedback to the large-scale processes. Convection processes have large effects on the generation, destruction and redistribution of the heat and moisture in the atmosphere. The resulting clouds play an important role in the surface heating, the atmospheric radiation and the vertical stability. In his NWP study, Gérard (2007) defined a "grey-zone" for grid meshes between 1 km and 10 km where deep convection is partly resolved and partly a subgrid-scale process. It is not clear yet where in this grey-zone the use of the convection parameterization is necessary (Gérard *et al.*, 2009; Piriou *et al.*, 2007; Bengtsson *et al.*, 2013). Yu and Lee (2010) used the MM5 version 3.7.0 (Dudhia, 2005) to do some tests about convective parameterization in the grey-zone using 9-, 6- and 3-km grid meshes simulations. They found that the 3-km simulation is sufficient to resolve the convection band considered in their study so that convective parameterization may not be necessary. On the other hand, the 9-km simulation is not sufficient to reproduce the deep convection and such parameterization tends to suppress the development of the resolved convective band. Some studies find that grid meshes finer than 1 km are required to explicitly resolve convective clouds (Arakawa and Chen, 1987; Molinari

and Dudek, 1992; Petch *et al.*, 2002; Bryan *et al.*, 2003; Craig and Dörnbrack, 2008), while other studies find that coarser meshes (such as 4 km) appears to be sufficient to explicitly resolve convection (Weisman *et al.*, 1997; Deng and Stauffer, 2006). Clearly this calls for further investigation to extend the generality of these conclusions; furthermore such tests have not yet been made with climate models. In our study, the deep convection was turned off and the explicit cloud microphysics turned on for simulations with 3-km and 1-km meshes. For coarser grid spacing (d81, d27 and d9) simulations, the deep convection was parameterized with the KFC scheme (Kain and Fritsch, 1990). Finally, for simulations with grid meshes of 9 km and coarser, a gravity-wave drag (GWD86: McFarlane, 1987) is used to parameterize the drag exerted on the large-scale flow due to the ensemble effect of non-resolved mountain-induced gravity waves, as well as low-level orographic blocking (Zadra *et al.*, 2003). With finer grid spacing (d3 and d1 simulations), the better representation of the topography renders unnecessary these parameterizations.

In summary, some parameterization schemes have to be changed during the cascade as a direct effect of changing resolution. These schemes are the large-scale condensation or cloud microphysics schemes, the empirical diagnostic vs. prognostic precipitation algorithms, the deep convection scheme and the gravity-wave drag for low-level orographic blocking. On the other hand, there did not appear to be any need to adjust other schemes such as the land-surface scheme, the radiation scheme, the shallow-convection scheme and the boundary-layer scheme.

2.2.2.4 Lateral Boundary Conditions

The key for the cascade's success is the control exerted by the coarser resolution LBCs upon the finer resolution integrations. The d81 simulation is driven, at 6-hourly intervals, by the ERA-Interim data, available to us on a 2° mesh. The d81 results are then archived and used to drive the d27 at 3-hourly intervals. The d27 provides the

LBCs at hourly intervals for two sets of d9 simulations (named d9 and d9_pilots). As mentioned before, the 9-km mesh marks the transition between hydrostatic and non-hydrostatic simulations, and the corresponding changes in the parameterizations. Two sets of 9-km mesh simulations are performed with hydrostatic dynamics, but one uses large-scale parameterizations (denoted d9) and the other (denoted d9_pilots) uses the prognostic cloud and precipitation microphysics scheme of Milbrandt et Yau (2005a, 2005b). Then, the d9 simulation is the one presented in the results analysis, while d9_pilots is only used to provide all variables required for the d3 simulation. The d9_pilots LBCs include new hydrometeors' masses (Q_c, Q_r, Q_n, Q_i, Q_g, Q_h) and new hydrometeors' concentrations (N_c, N_r, N_n, N_i, N_g, N_h) where, c stands for cloud, r for rain, n for snow, i for ice, g for graupel and h for hail. The cyan words in table 2.1 represent the configuration differences between d9 and d9_pilots, and the purple words are those between d9_pilots and d3. Then, the d9_pilots simulation provides driving data for d3 at 20-min intervals and the last simulation of the cascade (d1) is driven by d3's data every 5 min.

A central issue with the cascade technique is the choice of the grid mesh and the domain size. Indeed, the domain should be large enough to allow the development of the small scales features, but small enough to ensure control by the driving data as well as limit computational cost (Jones *et al.*, 1995; Leduc and Laprise, 2009). Hence a compromise should be achieved between the domain size and the grid mesh and what constitutes the optimal resolution jump between the regional model and the driving data is not universally accepted. In their cloud-resolving simulations, Clark and Farley (1984) showed that the maximum acceptable resolution jump was about a factor of three. Other studies found that much larger resolution steps were acceptable (e.g. Beck *et al.*, 2004; Suklitsch *et al.*, 2008) and for NWP applications, the resolution jump is often smaller than three (e.g. Mailhot *et al.*, 2012). For their 45-km mesh simulations, Denis *et al.* (2003) showed that a factor of ten appears acceptable for regional climate modelling. The RCM domain size have to be a large enough and

a rule-of-thumb seems to be that the domain should be larger than 10 grid points of the driving data (O. Christensen, DMI, personal communication). However, the resolution jump of three between the driven data and the finer LAM simulation seems appropriate for this study.

2.3 Results

The Section 2.3 is dedicated to the analysis of the cascade results. The results are divided in three sub-Sections, the first part will talk about the analysis of the dynamic wind fields (2.3.1), the second part is the kinetic energy spectra analysis (2.3.2) and the last part is the physical interpretation of the precipitation field (2.3.3).

2.3.1 Dynamical Analysis of Wind Fields

2.3.1.1 High-Resolution SLRV Channelling Effect

Low-level winds are important variables that are directly affected by the topography. The phenomenon of channelling refers to the tendency of the winds to blow more or less parallel to the valley axis for a variety of wind directions above the valley (Eckman, 1998; Weber and Kaufmann, 1998; Kossmann and Sturman, 2003; Nawri and Stewart, 2006). The surface winds from northeast direction observed in the SLRV during winter at Montréal city (red point in figure 2.2) and during throughout the year at Québec city (blue point in figure 2.2) are, most of the time, due to the pressure-driven channelling concept associated with the SLRV presence (e.g. Roebber and Gyakum, 2003; Carrera *et al.*, 2009). The synoptic flow in the free atmosphere is essentially in geostrophic balance, while in the low levels, the flow interacts with the valley and an imbalance is induced in the equations of motion: the Coriolis force is no longer balancing the pressure gradient force. The inertial terms and the friction force introduce surface-wind channelling along the valley. Figure 2.3

shows different types of winds induced by the pressure-driven channelling in the SLRV, the northeast winds are represented in (a) and southwest winds in (b). In situation of low roughness and stable atmospheric conditions, the valley winds can become very strong with the direction along the valley from high to low synoptic pressure.

Figure 2.4 shows typical northeast SLRV winter winds of the cascade simulation as theoretically schematized by figure 2.3 (a). The figure represents the weather situation of the 1200 UTC 26 February 2002 time step for d81 (a), d27 (b), d9 (c) and d3 (d) simulations. The background colors and the black arrows show the speeds [m/s] and the directions of the 1000 hPa horizontal wind, respectively. The black lines are the mean sea level pressure in hPa. The geostrophic winds above the valley (not shown) are parallel to the pressure field and blow from southeast to northwest (perpendicular to the SLRV). In the low-levels, the valley winds blow parallel to the SLRV axis from high to low pressure (northeast to southwest). Others topographic effects, such as the Lake Ontario, the East Coast and the LCV (especially for d3) are observed and almost amplified as the horizontal resolution is becoming finer. Figure 2.5 shows that the southwest winter winds case, theoretically illustrated by figure 2.3 (b), is also observed in the results.

2.3.1.2 Intensity/Frequency/Direction Wind Diagrams

Wind rose diagrams are very useful tools to study at the same times the frequencies, the directions and the intensities of wind fields. Figure 2.6 shows the 1000-hPa wind rose diagrams for d81 (a), d27 (b), d9 (c) and d3 (d) at the closest grid point to Québec City (blue point in figure 2.2) and averaged over the common period (0000 UTC 13 February to 0000 UTC 1 March 2002). The diagrams represent the frequencies (circles) distributions of each wind intensities (colors) and directions (bands) pair contribution to the total wind. For example, northwest winds with

intensities between 4 and 6 m/s occur 11.8 % of the time during the period in the d81 simulation, while 7.5 % of the winds come from the same direction but with weaker strength (2 to 4 m/s). An increase of the intensity and the frequency of the wind blowing along the SLRV axis (essentially absent of d81) is noted with the refinement of the grid mesh. The channelling is definitely more present and more intense with the finer topography definition of the high-resolution climate simulations (d9 and d3), consistent with figures 2.4 and 2.5. Figure 2.7 shows wind rose diagrams of the nearest Québec city grid point of d3 wind simulation for the 1000 hPa (a), 900 hPa (b), 800 hPa (c) and 700 hPa (d) levels. The Ekman spiral (Ekman, 1905) observed in the figure 2.7 shows a shift from northeast to north wind directions and an increase in the intensities when gradually passing from the low to high levels of the atmosphere.

2.3.2 Dynamical Analysis of Kinetic Energy Spectra

A useful variable to study the dynamical behaviour of the climate model atmosphere is the variance spectra that permit to quantify how much power there is in the different spatial scales of a field. It is well known that the stationary component of the Kinetic Energy (KE) dominates the dynamical flow at larges scales and the transient component is gradually dominates the flow at synoptic scales (Boer, 1994; Lilly *et al.*, 1998). Several techniques exist in order to compute variance spectra. For global data on the sphere, horizontal fields can be decomposed in their spectral coefficients of spherical harmonics, made of product of Fourier series along latitude circles and associated Legendre polynomials in latitude. Over a limited-area domain, a Discrete Fourier Transform (DFT; Ahmed *et al.*, 1974) can be computed; artefacts however often appear in the spectrum as a result of the non-periodic nature of the fields (Denis *et al.*, 2002). Three methods have been proposed to circumvent this issue. The first one consists in rearranging the field, making it periodic by removing a linear trend before the application of the DFT (detrending-DFT; Errico, 1985). Although this

process seems to improve the small-scale portion of the spectrum, it usually contaminates the large-scale gradient that exists in the domain and thus affects the large-scale portion of the spectrum. The second method is the application of a weighting function on the physical field before the DFT calculation; this method is called windowing-DFT (Turner, 1994; Salvador *et al.*, 1999). This technique improves the computed spectrum by avoiding the distortion of the spectrum's tail (high wavenumbers). Nonetheless, it seems appropriate for only large-dimension domains, which is usually not the case for a LAM. To compute the KE variance spectra over a limited-area domain, the Discrete Cosine Transform (DCT; Denis *et al.*, 2002) will be used to decompose the two-dimensional horizontal wind fields as a function of the spatial scales present in the domain. The DCT is a simplification of the DFT by removing their sine component giving by the symmetrisation of the regional field. Let $f_U(x,y)$, the horizontal wind component discrete field defined on N_x x N_y horizontal grid points, the direct and inverse DCTs are expressed as:

$$F_U(m,n) = \beta(m)\beta(n) \sum_{x=0}^{x=N_x-1} \sum_{y=0}^{y=N_y-1} f_U(x,y) \times \cos\left[\frac{\pi m\,(x+1/2)}{N_x}\right] \cos\left[\frac{\pi n\,(y+1/2)}{N_y}\right] \tag{2.13}$$

and,

$$f_U(x,y) = \sum_{m=0}^{m=N_x-1} \sum_{n=0}^{n=N_y-1} \beta(m)\beta(n) F_U(m,n) \times \cos\left[\frac{\pi m\,(x+1/2)}{N_x}\right] \cos\left[\frac{\pi n\,(y+1/2)}{N_y}\right] \tag{2.14}$$

with,

$$\beta(m) = \begin{cases} \sqrt{\frac{1}{N_x}}, & for\ m = 0 \\ \sqrt{\frac{2}{N_x}}, & for\ m = [1, N_x - 1] \end{cases} \quad (2.15)$$

and,

$$\beta(n) = \begin{cases} \sqrt{\frac{1}{N_y}}, & for\ n = 0 \\ \sqrt{\frac{2}{N_y}}, & for\ n = [1, N_y - 1] \end{cases} \quad (2.16)$$

where *(x,y)* are the coordinates on the horizontal plan and $F_U(m,n)$ is the matrix of the spectral coefficients of the direct DCT corresponding to *(m,n)* dimensionless wavenumbers ($k = \sqrt{n^2 + m^2}$). The spectral coefficients of *V* component, $F_V(m,n)$, can also be computed the same way. The variances of *U* and *V* are determined by the spectral coefficients of the direct DCT:

$$\sigma_U^2(k) = \sum_{m=0}^{N_x-1} \sum_{n=0}^{N_y-1} \frac{F_U^2(m,n)}{N_x N_y} \quad (2.17)$$

and,

$$\sigma_V^2(k) = \sum_{m=0}^{N_x-1} \sum_{n=0}^{N_y-1} \frac{F_V^2(m,n)}{N_x N_y} \quad (2.18)$$

for $(m,n) \neq (0,0)$. The total variance of KE is calculated as:

$$\sigma_{KE}^2(k) = \frac{\sigma_U^2(k) + \sigma_V^2(k)}{2} \tag{2.19}$$

Finally, if desired, the vertical average of the variance ($\sigma_{KE}^2(k)$) over the pressure levels can be done followed by the temporal average over the selected period. Because of the mirror effect of the DCT, for a square domain $N_x = N_y = N$, the highest and the lowest wavelengths computed in the variance spectra correspond to:

$$\lambda_{max} = 2\,N\,\Delta x \tag{2.20}$$

$$\lambda_{min} = 2\,\Delta x\,\frac{N}{N-1} \tag{2.21}$$

where Δx is the grid spacing in km.

At synoptic scales, where quasi-geostrophic balance prevails, the KE spectrum as a function of horizontal wavenumbers follows a k^{-3} power law. This result is consistent with two-dimensional quasi-geostrophic turbulence theory (Charney, 1971; Boer and Shepherd, 1983). Indeed Kraichnan (1967) showed that the synoptic part of the spectrum corresponds to a nonlinear enstrophy (vorticity square) cascade form large to small scales. The analysis of aircraft observations by Nastrom and Gage (1985) and Gage and Nastrom (1986) showed a spectral slope of $k^{-5/3}$ at mesoscales. Yet, the theories explaining this part of the spectrum are not well understood. Dewan (1979) and VanZandt (1982) proposed that the $k^{-5/3}$ spectral behaviour could be explained by internal gravity waves, with long waves interactions to generate shorter waves and corresponding to a positive energy flux. This explanation agrees with the three-dimensional turbulence theory of Kolmogorov (1941) developed for very small scales (~cm). On the other hand, as the mesoscale flow is not three-dimensional, Gage (1979) and Lilly (1983) proposed that the $k^{-5/3}$ slope arises from the two-dimensional turbulence theory of Kraichnan (1967). The latter theory is characterised by a negative energy flux from small scales (convection, surface forcing) to mesoscales. In

any case, observations and theories are consistent to give a k^{-3} spectral slope for large scales and a $k^{-5/3}$ slope at small scales, with some transition between these two slopes at some scale that differs depending upon theories.

The ability of a model to reproduce the two spectral slopes discussed before is not universal. Some models represent well the observed spectral slopes and others show slopes rather different due to the formulation of the numerical schemes and physical parameterizations. Global GCMs seem to well reproduce the k^{-3} dependence at large scales. Koshyk and Hamilton (2001) even showed a transition to $k^{-5/3}$ at approximately 30-km wavelength, but problems with model's dissipation bring a strong overturned tail. Cloud-resolving models that explicitly resolve convection with grid spacing less than 1 km succeed in the representation of the $k^{-5/3}$ relation (Vallis *et al.*, 1997). Lilly *et al.* (1998) showed that KE in such model is dominated by the divergent modes comparatively to the rotational modes at large scales. Concerning the RCMs and the mesoscale models, the examination of the spectra is more difficult for three reasons. The first one is related to the aperiodic nature of the fields, the second one is that a long time series seem to be required to obtain a representative spectrum and finally there is very little data to compare with.

2.3.2.1 Spin-up of KE Spectra

Starting from and driven by coarse-mesh data, a high-resolution model can develop fine-scale KE variance in different ways. First, there is the direct forcing of the flow with the topography, as the terrain possesses structures at all spatial scales and the associated spectral slope is k^{-2} (Balmino, 1993). Next, there exist the two energy cascades mentioned before. The theories predict that energy from larger scales (present in the LBCs) should quickly fill the mesoscale part of the spectrum (Yuan and Hamilton, 1994). The second cascade is an input of mesoscale energy from the small-scale phenomena such as convection and surface forcing (Lilly *et al.*, 1998).

Skamarock (2004) evaluated the ability of the regional WRF model in terms of the KE spectra statistics. The forecasts were initialized, over the United States of America, on 0000 UTC 1, 2 and 3 June 2003, using 22-, 10- and 4-km grid spacing, respectively. First, it has been shown that long-term series is not really required for computing spectra and that it is possible to compute stable spectra for diurnal cycles. Second, the spin-up times required to completely fill the mesoscale part of the KE spectra of the WRF model have been found between 6 and 12 h for the three grid spacing tested. Figure 2.8 shows the KE spectra of the initial states of the CRCM5 cascade simulations: d81 (a), d27 (b), d9 (c), d3 (d) and d1 (e). The abscissas are the horizontal wavenumbers $k = 2\pi/\lambda$, where λ is the wavelengths in kilometers represented by the upper x-axis. The ordinates correspond to the spatial variance, expressed in J/m^2, vertically averaged from 700 to 200 hPa. To remove the effects induced by the lateral boundaries, the spectra were computed over 50 x 50 inner horizontal grid points. The different line colors correspond to the time step after the initialization as identified by the legends of each panel. The longest wave represented in the spectrum is roughly two times the number of grid points multiplied by the grid spacing in kilometers ($2*50*\Delta x$) and the shortest wave is approximately two times the grid spacing in kilometers ($2*\Delta x$) corresponding roughly to the equations 2.20 and 2.21. Because the main contribution of KE variance is located in the large scales, the spectra are presented in logarithm graphs to better distinguish the small scales portion. So the KE variance spectra spin-up times are seen to be roughly 12 h for d81 and d27, 10 h for d9, 1 h for d3 and 50 min for d1.

Other variables (temperature, geopotential height and specific humidity) show approximately the same spectra spin-up times (not shown, see figures A.1 to A.3 in Annexe A).

2.3.2.2 Effective Resolutions

The model's resolved scales are related to the grid size; the longest permitted scale is limited by the domain size, while the shortest permitted scale is simply equal to the grid spacing. It is important to distinguish the mesh size and the resolution of a model. The KE variance spectra provide a first measure of the necessary condition to be fulfilled for declaring a scale as resolved; the actual simulation skill is a further condition. KE spectra near the upper wavenumber limit of a model provide useful information on the influence of a model's domain size, numerical techniques and dissipation mechanisms. The role of dissipation in particular is to remove small-scale energy to avoid aliasing that would misrepresent the physical interactions. While excessive dissipation may cause damping of the spectrum's tail, insufficient dissipation on the other hand can result in raised tail (Koshyk and Hamilton, 2001). A pragmatic definition of the effective resolution is the wavelength at which a spectrum begins to exhibit decay compared to some reference spectrum obtained from either an observational dataset or from a higher resolution model's simulation. The length scales shorter than the effective resolution have to be considered as dynamically suspects. It would be preferable to use reference spectrum from observations but these spectra are not always available at the desired resolution. The use of spectra computed from higher resolution model must however be done with care as they can lead to false interpretations when the domain sizes are different or because regions are climatologically non-equivalent (such as continents Vs. ocean or mountainous Vs. valleys). Skamarock (2004) found an effective resolution equal to seven times the grid spacing ($7\Delta x$ in km) for the three grid meshes (22, 10 and 4 km) of his study and attribute these results to the filters used in the WRF model. This resolution is also close to the limit of the ability of the low-order finite differences; in general, the effective resolution is considered to lie between $6\Delta x$ and $10\Delta x$ (Skamarock, 2004; Durran, 2010).

Figure 2.9 shows KE spectra of the five simulations, averaged vertically from 700 to 200 hPa and temporally on the common period from 0000 UTC 13 February to 0000 UTC 1 March 2002, excluding the first 24 hours. The black line represents d81, the blue lines are d27, the red lines are d9, the green lines are d3 and the pink one is d1. The solid lines are the spectra computed on 44 x 44 inner horizontal grid points and the dashed lines are the spectra computed over 134 x 134 inner horizontal grid points. The dashed lines are used to find the effective resolution of the nearest coarser resolution spectrum because there are computed on the same region. The effective resolutions of d81, d27, d9 and d3 can be determined by comparing the spectra as follows: d81 (solid black curve) with d27 (blue dashed curve), d27 (solid blue curve) with d9 (red dashed curve), d9 (solid red curve) with d3 (green dashed curve) and d3 (solid green curve) with d1 (pink dashed curve), respectively. The d1 effective resolution cannot be found because of the absence of a higher resolution simulation. The effective wavenumbers (coloured arrows) are approximately 0.011, 0.033, 0.1 and 0.3 rad/km for d81, d27, d9 and d3, respectively. This corresponds to effective wavelengths of roughly 571, 190, 63 and 21 km, respectively and then giving effective resolutions of seven times the grid spacing ($\Delta x_{eff} = 3.5*2\Delta x$), consistent with the study of Skamarock (2004). There is also an observed shift in the spectral slopes from k^{-3} at large scales to $k^{-5/3}$ at small scales noted in d1 at wavelength of 20 km, which is relatively close to the same effective resolution. Clearly as the grid mesh becomes finer, more small scales are resolved and for the comparative wavenumbers, the variance of KE is increasing (we have no explanation for this last result but we are inclined to believe that appears due to an artefact of the spectral algorithm).

2.3.2.3 Vertical Distribution of Horizontal KE

It is informative to look at the vertical distribution of the horizontal KE spectra. One expects that energy in large scales must be greater in upper troposphere because of

the existence of synoptic and planetary waves, and that the low levels will have more energy in small scales than at higher levels. Figure 2.10 shows logarithmic representation of KE variance spectra calculated over 50 x 50 inner grid points for the five simulations of the cascade and vertically averaged over five different layers (colours shown by the legend). The line styles are changed to better distinguish the five simulations identified in the figure. The spectra are time-averaged over the complete period of the respective dates of integrations, excluding their first 24 hours. The spectra should not be compared directly between themselves because the spectra are computed over different regions and periods. The behaviour of each layer follows well our expectations; the lower levels contain more small-scale energy and the higher levels contain most of the large-scale energy.

2.3.3 Physical Analysis of Precipitation Fields

The precipitation field is a useful variable to analyse the added value of the cascade method. One expects that precipitation simulated by nested LAM, while constrained to follow the general spatial and temporal behaviour imposed by the coarser resolution LBCs, will develop their own fine-scale structures permitted by the high spatial resolution. Over the analysis domain, the winter precipitation is essentially governed by the uplift of the humidity associated with mid-latitude depressions, which condenses over fairly large scales and leading to a predominance of stratiform precipitation. The precipitation intensity distribution allows comparing the effect of increased resolution in the cascade. The precipitation intensity distribution statistics of the different simulations are compared over common preselected domain and period. At each grid point and for each archival time, three-hourly precipitation is binned and accumulated into preselected ranges of intensity. The mean of all grid points is made over each bin and the percentage contribution of each bin is calculated dividing by the total precipitation.

2.3.3.1 d81/d27/d9 Intensitiy Distributions

Figure 2.11 shows the distributions, by ranges of intensity, of the contributions to the three-hourly precipitation amounts of d81 (black bars), d27 (blue bars) and d9 (red bars) simulations for the common period of three months (from 0300 UTC 1 January to 0000 UTC 1 April 2002). The common domain of analysis is shown by the orange square in figure 2.11, corresponding to 153 x 153 horizontal grid points for d9, 51 x 51 for d27 and 17 x 17 for d81. The abscissa represents the intensity bins in mm/day and the ordinate is the percentage of the bin's contribution to the three-hourly mean total precipitation. The average and the maximum of each simulation are identified on figure 2.11 top left. It can be noted that, for example, 20.2 % of the three-hourly mean total precipitation comes from the bin 16-32 mm/day for d81, while for the same range, a lesser contribution is noted in d27 and d9: 18.3 % and 18 %, respectively. In contrast, there is an increase of the 128-256 mm/day range contribution when passing from 0.81° to 0.27° and to 0.09°: 0.7 %, 3.7 % and 5.9 %, respectively. The three-hourly intensity precipitation distribution is shifted from weaker to higher intensity bins as the mesh is refined. This fact is in good agreement with our understanding of the finer resolution effect.

Figure 2.12 is the mean precipitation of the 0300 UTC 13 February 2002 time step for d81 (a), d27 (b) and d9 (c). The drizzle (mean precipitation dimension < 1 mm/day) present in the d81 simulation is diminishing and a better definition of the intense precipitation bands for both d27 and d9 simulations appears, consistent with the information provided by the three-hourly mean precipitation intensity distribution.

2.3.3.2 d81/d27/d9/d3 Intensity Distributions

Figure 2.13 repeats a similar analysis as figure 2.11, but adding the d3 finer spatial resolution (green bars) with shorter temporal coverage (from 0300 UTC 4 February to

0000 UTC 7 March 2002) and smaller spatial coverage (shown by the orange square). Corresponding to large difference in the representation of the clouds and precipitation microphysics (hydrostatic Vs. non-hydrostatic), the passage from d9 to d3 is very important for the analysis of the precipitation field. The results caused by the different microphysics scheme show significant differences between each bin of d9 and d3 in the distribution. Same changes as figure 2.11 are noted, the weaker precipitation intensities are decreasing and the highest precipitation ranges are increasing, in term of percent of the three-hourly total precipitation, as the grid mesh is refined from d81 to d3.

2.3.3.3 d81/d27/d9/d3/d1 Intensity Distributions

Figure 2.14 shows the three-hourly precipitation intensity distribution of the d81 (black bars), d27 (blue bars), d9 (red bars), d3 (green bars) and d1 (pink bars) simulations, over the common domain corresponding to the d1 analysis region (163 x 163 horizontal grid points) and for the lesser common period (0300 UTC 13 February to 0000 UTC 1 March 2002). The distributions show no obvious changes from d1 compared to d3, suggesting that the statistics of the finer domain (d1) precipitation field is very similar to those of d3. For example, the larger percentage differences between d3 and d9 are approximately -10.6 % for the 1-2.5 mm/day bin and +15.8 % for the 10-25 mm/day bin, comparatively to differences of about -0.3 % and +0.1 % of d1 Vs. d3 for the same bins (1-2.5 mm/day and 10-25 mm/day, respectively).

Figure 2.15 shows the two-dimensional three-hourly mean precipitation of the 0000 UTC 17 February 2002 time step for d9 (a), d3 (b) and d1 (c). The general pattern of d9 is well reproduced by d3, but with an overall increase of the precipitation values. The d1 field is similar to d3 but with finer scale details, especially over the Green Mountains (black circle).

2.4 Conclusions

High-resolution modelling has a big potential for improving the accuracy of the climate simulations on regional and local scales. This is due to a better representation of the surface forcing such as topography and to the explicit resolution of mesoscale circulations such as deep convection and cloud microphysical properties (including precipitation types). In this study, a general methodology was proposed to obtain very high-resolution climate simulations at a reasonable computational cost. In our experiments, it consisted in a series of five one-way nested simulations with grid mesh ranging from 0.81° to 0.01° by steps of three. It was shown that if one accepts to make some compromises, such as reducing the domain size and the length of integration as the mesh gets finer, the computational cost could be kept roughly constant between all simulations. In practice, however, the cost increases somewhat because explicit cloud microphysics parameterization is turned on with the finer resolution (d3 and d1). Fifteen days in the February 2002 month were run successfully with the CRCM5 at 0.01° horizontal resolution (roughly 1-km grid spacing). Although the evaluation of the resulting simulations is difficult because of the lack of high-density observations, the results are encouraging for high-resolution climate simulations, thus paving the way for future climate projections usable for impact studies.

To evaluate the simulations obtained with the cascade method, a diagnostic study was performed using KE variance spectra. It was found that simulations initialised and driven by three times coarser data exhibited development of fine scales, visible in the KE spectra, with spin-up times of roughly 9 to 12 h for d81, d27 and d9 simulations, and roughly 1 h for d3 and d1 simulations. The KE spectra also showed that the effective resolution, defined as the shortest wavelength not exhibiting an overdamping of the KE amplitudes, is roughly seven times the grid spacing for all the simulations, in agreement with the findings of Skamarock (2004) using the WRF model. The shift in the spectral slope form k^{-3} (large scales) to $k^{-5/3}$ (small scales),

expected from many theories and observations, is seen in the d1 simulation to occur around the 20-km wavelength. The results are in good agreement with the understanding and the theoretical expectations of the atmospheric dynamical behaviour from a KE spectra point of view.

To complete this feasibility study, some variables such as the precipitation field and the low-level winds, which greatly depend on the details of the topography and consequently are dependent of the resolution of the model, have been examined. The domain of analysis is influenced by the presence of orographic features that affect the local climate of the region: two valleys (the St-Lawrence River and the Lake Champlain Valleys) and three major mountainous regions (the Appalachians, the Adirondacks and the Green Mountains). The same general patterns of precipitation are reproduced in the d81, d9 and d27 simulations, indicating a strong control by the LBCs. One notes however a tendency for concentrating the precipitation in narrow bands at higher resolution. The transition from d9 to d3 simulations is very important because of the changing microphysics' parameterizations from diagnostic to prognostic (CONSUN to MYDM) with a noteworthy repercussion on the precipitation fields. The better definition of the topography at 0.03° and 0.01° seems to bring significant changes for the precipitation. The general features of d9 precipitation are well reproduced by d3 and d1, but the finer topography results in substantial differences in intensity. The d1 precipitation is rather similar to d3, with a small but detectable amplification of the orographic effects. The simulated three-hourly precipitation intensity distributions exhibit systematic changes as a function of resolutions: weaker precipitation intensities become less frequent and higher precipitation intensities become more frequent with the finer grid spacing, in agreement with expectations of grid refinement. Finally, the influence of the St-Lawrence River Valley on the winter wind fields becomes increasingly felt with the refinement of the resolution, as it shown by wind roses and map for the northeast and southwest winds induced by the pressure-driven channelling.

Future work is needed to evaluate the quality of simulations with some high-density observations (e.g. radar data) and to quantify the added value afforded by the cascade method. Other studies can be done to extend the potential of very high-resolution climate simulations such as choosing different period (e.g. summer instead of winter) and domain (e.g. high mountainous region). In conclusion, results of this feasibility study are encouraging as first step in the development of the next generation of very high-resolution CRCM5, with mesh of the order of one kilometer.

Acknowledgements

This research was funded by the Québec's *Ministère du Développement Économique, Innovation et Exportation* (MDEIE), the Natural Sciences and Engineering Research Council of Canada (NSERC), Hydro-Québec and the Ouranos Consortium on Regional Climatology and Adaptation to Climate Change. The calculations were made possible through the CLUMEQ Consortium, on the Colosse and Guillimin high-performance computing platforms; CLUMEQ is part of the Compute Canada national HPC platform and a member of the *Calcul Québec* regional HPC platform. The authors thank Mr. Georges Huard and Mrs. Nadjet Labassi for maintaining an efficient and user-friendly local computing facility. The authors are greatly indebted to Ms Katja Winger and Dr Bernard Dugas for helping with the CRCM5 code; without their precious assistance this work involving multiple cascades of CRCM5 with different parameterization packages would not have been possible.

CHAPITRE III

CONCLUSION

L'objectif de cette étude était d'appliquer la méthode de grilles télescopiques (aussi dite de cascade) à la 5^{e} génération du Modèle Régional Canadien du Climat pour effectuer une étude de faisabilité de ce modèle à très haute résolution. La nécessité d'une telle étude se résume par la volonté des climatologues à fournir des simulations climatiques pour des échelles de plus en plus régionales, voire même locales. Les conséquences des changements climatiques perturbent la société et les écosystèmes notamment par le biais d'une augmentation dans la fréquence des évènements climatologiques intenses associés à des phénomènes de petites échelles. Dans cette étude, il a été montré que la méthode de cascade, déjà employée de façon courante en PNT, peut aussi s'appliquer en mode climat et ce, en respectant les limites raisonnables des ressources computationnelles disponibles.

La simulation climatique à très haute résolution permet une meilleure définition des forçages topographiques dans le modèle. La topographie exerce une grande influence sur la circulation synoptique, sur l'écoulement de plus petites échelles et sur les rétroactions qu'exercent ces deux types d'écoulement l'un sur l'autre. Les modèles du climat à très haute résolution sont des sujets très peu traités, mais tout de même d'actualité, et les récentes ouvertures concernant la possibilité de simuler le climat à des fines résolutions (de l'ordre du kilomètre) est en plein essor. Plusieurs effets découlant des changements climatiques pourraient être mieux évaluées, surtout en ce

qui concerne les évènements climatologiques extrêmes comme les fortes précipitations, les vents violents, les inondations et les dégâts associés aux différents types de précipitation (verglas, grésil et grêle).

C'est par le biais de nouvelles méthodes (comme celle de la cascade) que la simulation climatique de très haute résolution pourrait s'effectuer. La cascade consiste en une suite de simulations dans laquelle les grilles sont imbriquées les unes dans les autres. Une première simulation de résolution trop grossière pour des fins régionales sert à piloter une deuxième intégration de résolution plus fine et dont le domaine est restreint à une zone imbriquée dans le domaine de la première simulation. Un troisième domaine de maillage encore plus fin et imbriqué dans la deuxième intégration est ensuite simulé et contrôlé aux frontières latérales par la deuxième intégration. Ce processus peut alors être répété autant de fois que nécessaire afin d'atteindre la fine résolution souhaitée. Dans cette étude, la cascade était constituée de cinq simulations, la première ayant un espacement entre deux points de grille d'environ 81 km, la deuxième, de 27 km, la troisième, de 9 km, la quatrième, de 3 km et la dernière, de 1 km. Les domaines sont centrés sur Montréal, Québec, Canada et le domaine commun d'analyse couvre essentiellement la vallée du Saint-Laurent (vallée d'orientation sud-ouest/nord-est), la vallée du Lac Champlain (vallée d'orientation nord/sud) et plusieurs chaines de montagnes telles que les Laurentides, les Appalaches, les Adirondacks, les Montagnes Vertes et les Montagnes Blanches.

Il a été démontré que pour des nombres de points de grille et de pas de temps constants entre les simulations ($N_x * N_y * N_z * N_t = \text{constant}$), et pour un même facteur de saut de résolution et de pas de temps entre chaque simulation (ces sauts sont d'un facteur trois), le coût informatique théorique restait le même pour toutes les intégrations. Bien qu'il s'agisse d'une considération pragmatique théorique importante associée à l'application de la cascade climatique, en pratique, le coût

computationnel était difficilement maintenu constant et ce dû aux changements apportés dans les schémas de paramétrisation (abandon de l'approximation hydrostatique dans les fines résolutions). Dans cette étude, les trois premières simulations (81 km, 27 km et 9 km) étaient hydrostatiques et les deux dernières (3 km et 1 km) étaient non-hydrostatiques. Le passage de la simulation de 9 km à la simulation de 3 km était donc très important et plusieurs différences existaient entre ces deux simulations, notamment au niveau des schémas du modèle (condensation et convection) ainsi qu'au niveau de leurs paramètres associés (détermination des types de précipitation et coefficients de trainée engendrés par les ondes de gravité internes de sous échelles).

Les résultats étaient divisés en deux principales analyses. La première était l'étude du changement du comportement dynamique des simulations lorsque la résolution était raffinée par le biais des champs de vents horizontaux et d'énergie cinétique horizontale. La deuxième analyse était concentrée sur le champ de précipitation.

L'analyse des vents était principalement axée sur des exemples d'effets topographiques sur l'écoulement horizontal. Les deux premiers effets ont été associés à la présence du Lac Ontario et de la côte est Nord-Américaine, où était notée une intensification des vents lorsque le maillage de la grille du LAM était raffiné. Le troisième effet était un vent typique du nord-est, résultant de l'effet de canalisation dû à la présence de la vallée du Saint-Laurent. En effet, lorsque les conditions étaient propices (gradient de pression parallèle à l'axe de la vallée et vents au dessus de la vallée parallèles aux isobares), les vents à 1000 hPa s'accentuaient et s'intensifiaient, soufflant de la haute pression vers la basse pression le long de l'axe de la vallée. En général, les vents associés à l'effet de la vallée du Saint-Laurent augmentaient en fréquence et en intensité lorsque la résolution devenait fine, tel que démontré par les roses des vents du point de grille à l'entrée nord-est de la vallée du Saint-Laurent.

L'analyse spectrale a montré, en premier lieu, que l'équilibre dynamique de l'énergie cinétique dans les petites longueurs d'ondes a été atteint en moins de 12 h pour les cinq simulations de la cascade. Ce temps d'ajustement diminuait lorsque la résolution était raffinée, passant de 12 h pour la simulation grossière (81 km) à 50 min pour la simulation fine (1 km). En deuxième lieu, la résolution effective, qui est définie comme la longueur d'onde à laquelle une chute dans les amplitudes de petites échelles des spectres est observée, était d'environ sept fois la résolution horizontale (en kilomètres) pour les quatre premières simulations de la cascade (d81, d27, d9 et d3). Ainsi, pour des longueurs d'ondes plus petites que cette résolution effective, les spectres ont été considérés dynamiquement suspects (limite de résolution). En troisième lieu, l'analyse de la distribution verticale de l'énergie cinétique par les spectres de variance a montré que l'énergie cinétique horizontale des petites échelles est surtout importante dans les bas niveaux de l'atmosphère (1000-850 hPa) et que l'énergie cinétique des grandes échelles est plus importante dans les hauts niveaux de l'atmosphère (200-50 hPa). L'analyse spectrale de la cascade, de par ces trois résultats, est en accord avec notre compréhension de la dynamique de l'énergie cinétique de l'atmosphère.

Les distributions d'intensités du champ de précipitation archivé aux trois heures ont montré une augmentation des forts taux de précipitation compensée par une diminution des faibles taux de précipitation, et ce, au fur et à mesure que la résolution se raffinait. D'autre part, un changement significativement plus intense entre la simulation hydrostatique (9 km) et la simulation non-hydrostatique (3 km) a été constaté par l'effet accentué des chaines de montagne. Finalement, une faible intensification des taux de précipitation a été notée lors de la comparaison entre les deux simulations non-hydrostatiques (3 km et 1 km).

En conclusion, cette étude a bien démontré la faisabilité de l'application de la méthode de la cascade au MRCC5 tout en démontrant l'existence d'une valeur

ajoutée par les très hautes résolutions. Cette étude fût le premier pas vers la simulation du climat de très haute résolution effectuée par le MRCC5. Bien que les résultats aient été concluants quant à la faisabilité de l'application de la cascade, d'autres études sont nécessaires afin de valider la méthode. Tout d'abord, même si ces données ne sont pas encore totalement disponibles pour de telles résolutions, la validation des résultats avec des données d'observations est requise. Il serait possible, par exemple, de considérer l'interpolation des 351 stations météorologiques du Ministère du Développement durable, de l'Environnement de la Faune et des Parcs (MDDEP), principalement concentrées dans la vallée du Saint-Laurent, pour permette la validation de certains champs de surface de la cascade. L'utilisation des données radars pourrait également permettre la validation des champs de précipitation de haute résolution. La présente étude, principalement concentrée sur une période hivernale de 15 jours, gagnerait à être élargie à une période estivale pour laquelle la convection deviendrait importante et ayant ainsi des effets accentués sur le champ de précipitation. Par le même raisonnement, l'analyse d'un domaine d'orographie plus marquée, où l'influence topographique sur l'écoulement serait plus forte, devrait aussi être envisagée. Ces dernières suggestions seraient directement liées à une évaluation plus précise de la « zone grise » (Gérard, 2007) et du saut de résolution optimal à l'efficacité du changement de paramétrisation dans le cas du MRCC5. Finalement, une période de 15 jours est certes intéressante pour une étude de faisabilité, mais insuffisante pour fournir une robustesse climatique statistique. C'est ainsi que l'application de cascades pour une série d'évènements climatiques extrêmes de mêmes espèces (fronts, vents de canalisation, évènements convectifs) permettrait d'obtenir une étude climatologique statistiquement significative.

FIGURES

FIGURE DU CHAPITRE I : FIGURE 1.1
FIGURES DU CHAPITRE II : FIGURES 2.1 À 2.15

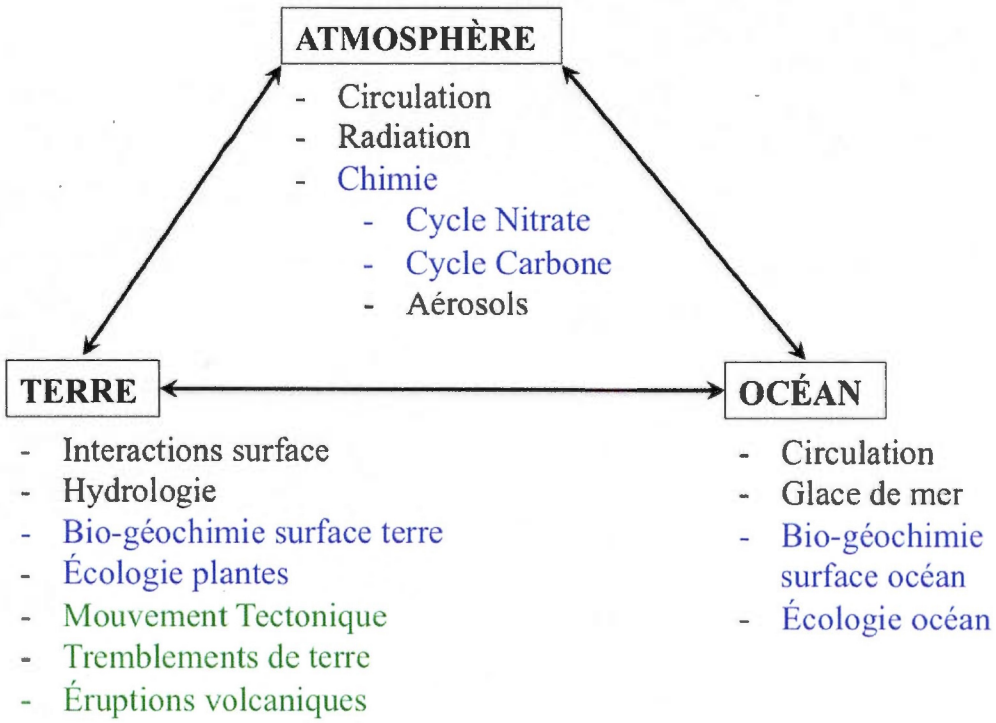

Figure 1.1 Composantes des ESMs (en bleu et noir), composantes des MCGs (en noir) et composantes à inclure (en vert) dans les ESMs.

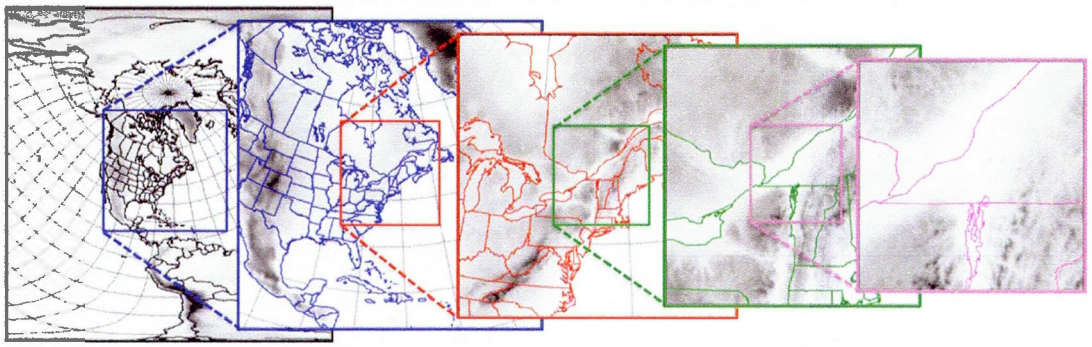

Figure 2.1 The CRCM5 cascade domains: d81 (black), d27 (blue), d9 (red), d3 (green) and d1 (pink). The domains are square and centred on Montréal, Québec, Canada (45°30'N, 73°35'W). The grey tones represent the topography definition of the CRCM5.

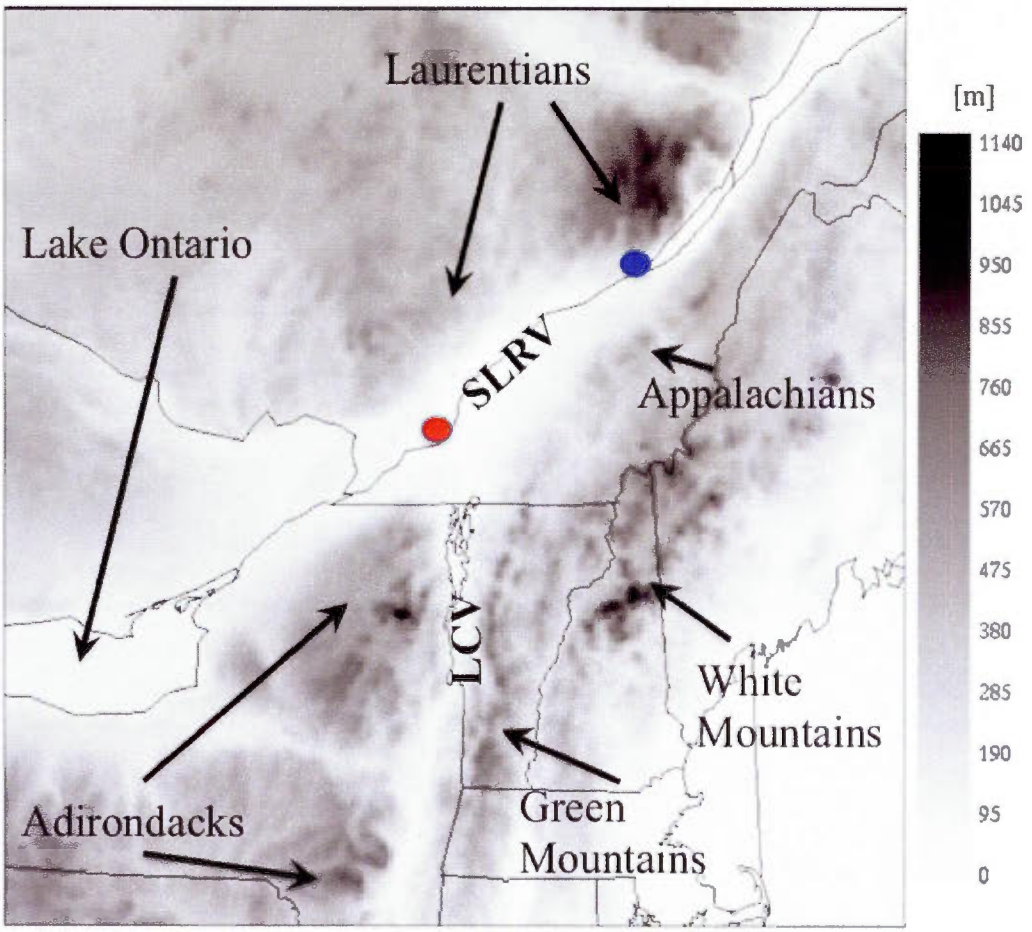

Figure 2.2 Topography input map [m] of the d3's domain. The red and blue points show the locations of Montréal and Québec cities, respectively. Some specific regions are identified such as the SLRV, the LCV, the Laurentian Mountains, the Lake Ontario, the Appalachians, the Adirondacks, the Green Mountains and the White Mountains.

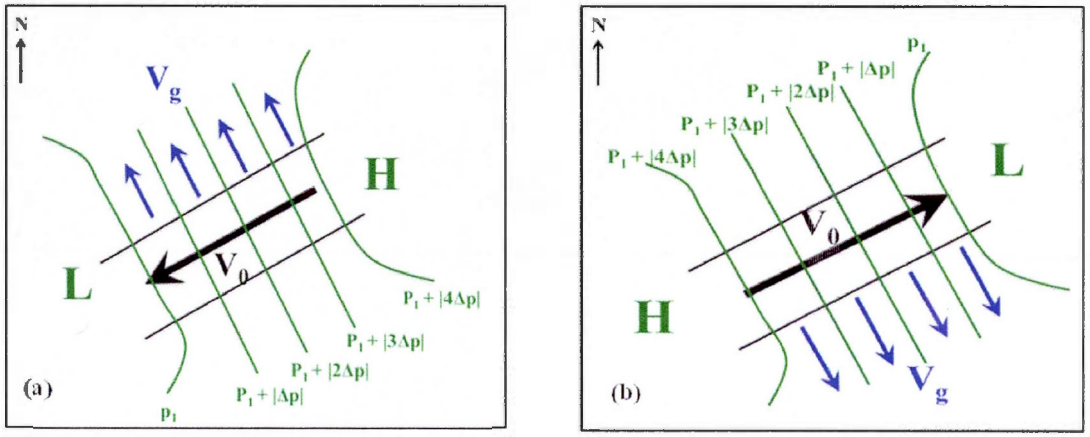

Figure 2.3 The pressure-driven channelling concept inducing winds blowing along the valley axis from high to low synoptic pressure for typical northeast winds (a) and typical southwest winds (b). The black lines are the SLRV axis, the black arrow represent the winds blowing along the valley (close to the surface), the green lines are the mean sea level pressure and the blue arrows are the geostrophic surface winds above the valley blowing parallel to the pressure lines.

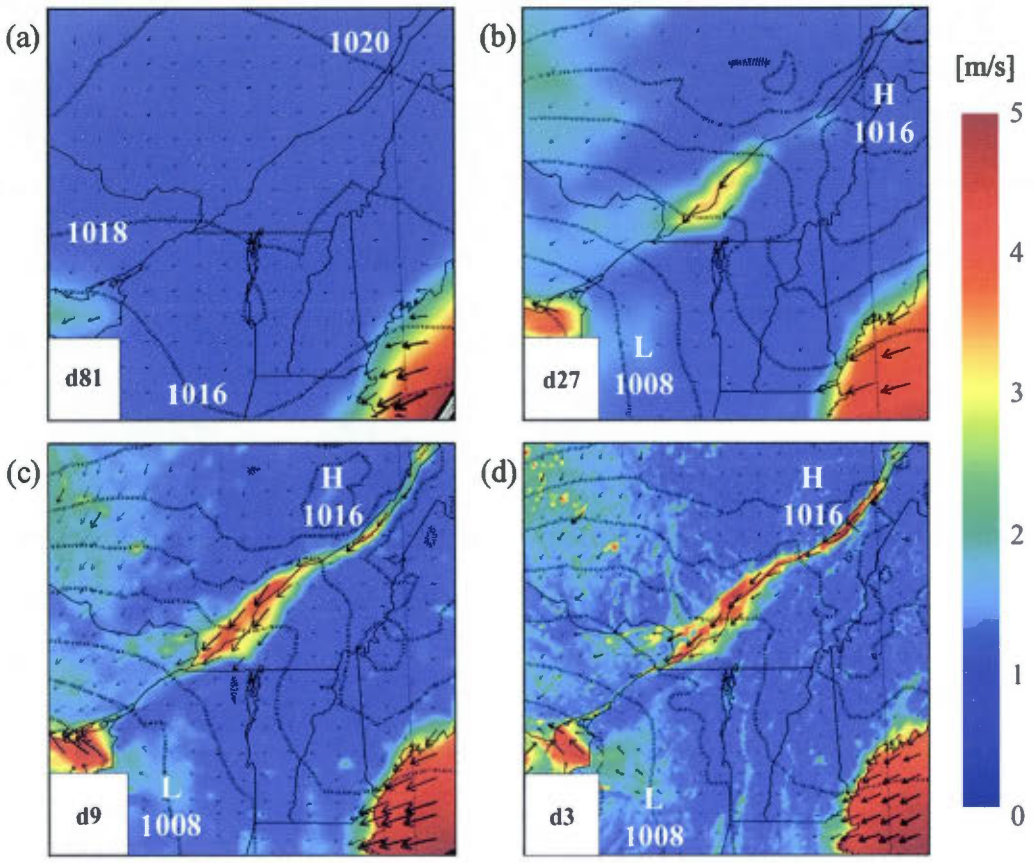

Figure 2.4 This figure shows typical northeast winter wind channelling in the SLRV of the d81 (a), d27 (b), d9 (c) and d3 (d) simulations for the 1200 UTC 26 February 2002 time step. The background colours and the black arrows show the speeds [m/s] and the directions of the 1000 hPa horizontal wind, respectively. The black lines are the mean sea level pressure in hPa.

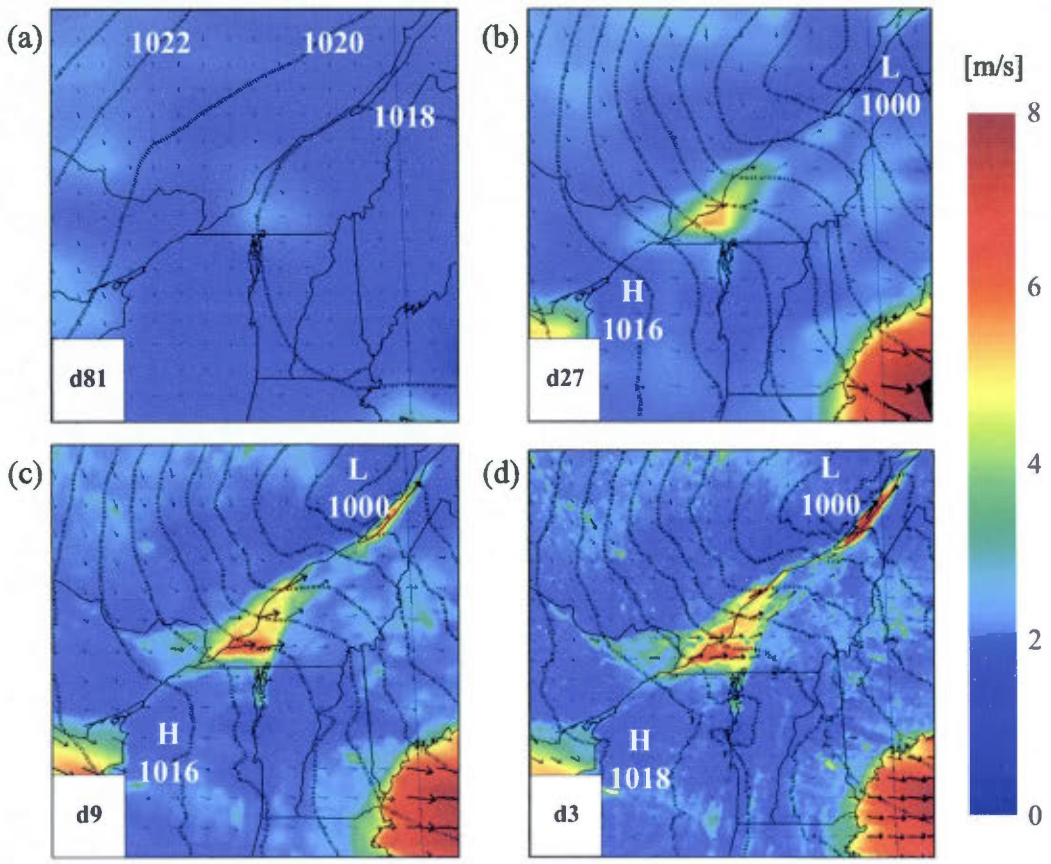

Figure 2.5 This figure shows typical southwest wind channelling in the SLRV of the d81 (a), d27 (b), d9 (c) and d3 (d) simulations for the 1800 UTC 16 February 2002 time step. The background colours and the black arrows show the speeds [m/s] and the directions of the 1000 hPa horizontal wind, respectively. The black lines are the mean sea level pressure in hPa.

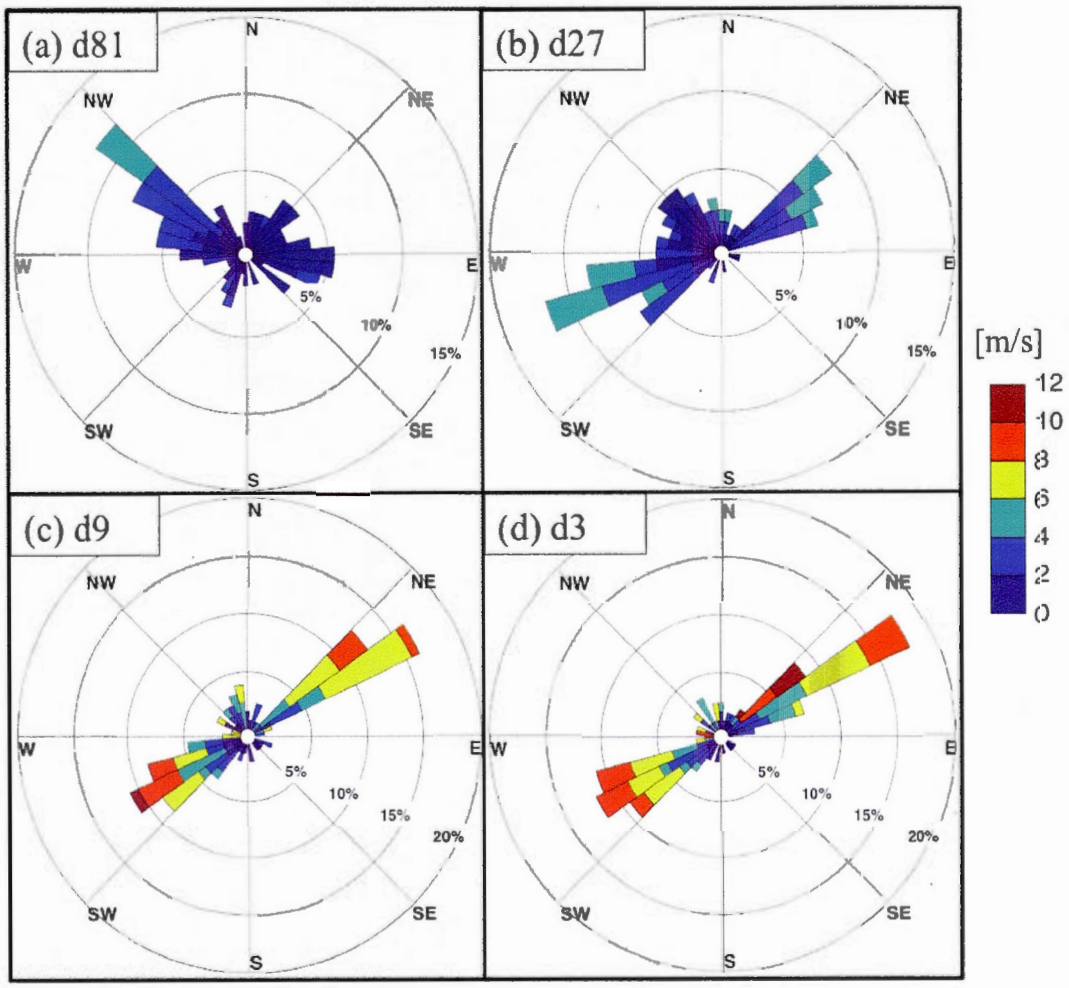

Figure 2.6 Wind rose diagrams of the 1000 hPa horizontal wind for the d81 (a), d27 (b), d9 (c) and d3 (d) simulations over the common period (from 0000 UTC 13 February to 0000 UTC 1 March 2002) and for the nearest Québec City grid point (blue point in figure 2.2). The colours represent the wind intensities [m/s] and the circles are the frequencies [%] of each intensity/direction pair's contribution to the total wind.

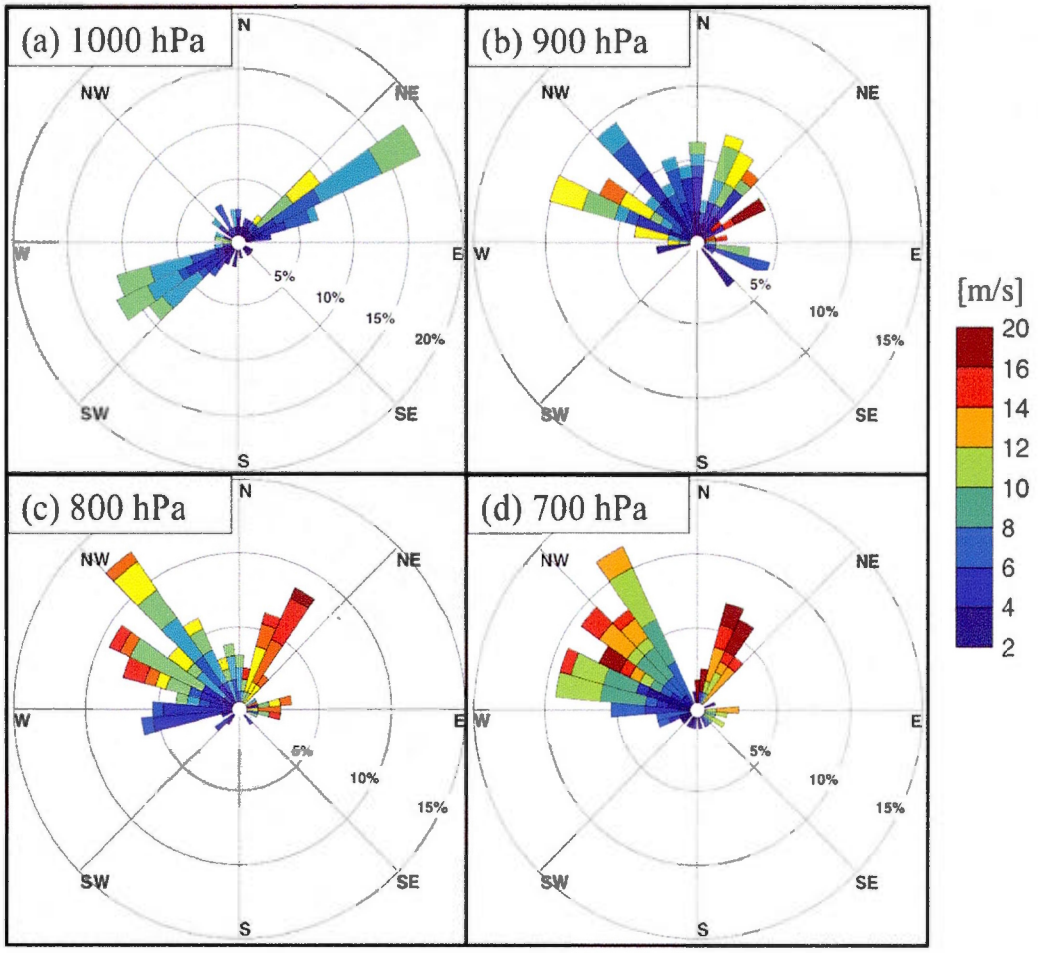

Figure 2.7 The Ekman spiral effect shown by d3's wind-rose diagrams of the nearest Québec City grid point (blue point in figure 2.2). Four levels are shown: 1000 hPa (a), 900 hPa (b), 800 hPa (c) and 700 hPa (d). Each level wind field is averaged over the common period (from 0000 UTC 13 February to 0000 UTC 1 March 2002). The colours represent the wind intensities [m/s] and the circles are the frequencies [%] of each intensity/direction pair's contribution to the total wind.

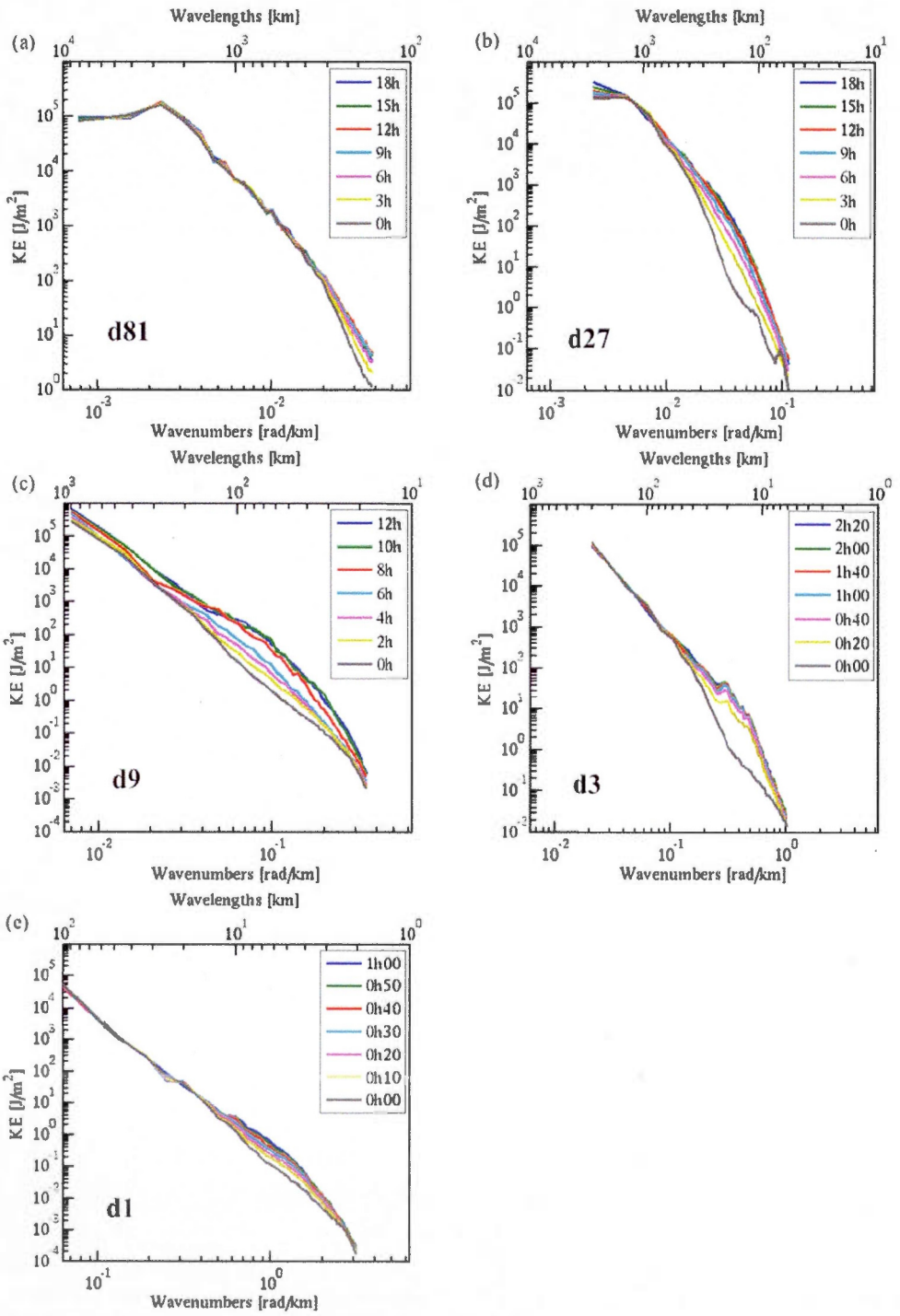

Figure 2.8 Logarithmic representation of the spatial variance spectra of horizontal KE vertically averaged from 700 to 200 hPa over 50 x 50 inner horizontal grid points of the initial states of each simulation: d81 (a), d27 (b), d9 (c), d3 (d) and d1 (e). The different line colors correspond to the time step identified by the legend of each panel. The abscissas represent the wavenumbers [rad/km], the upper abscissas are the wavelengths [km] and the ordinates are the spatial variance of horizontal KE [J/m^2] vertically averaged.

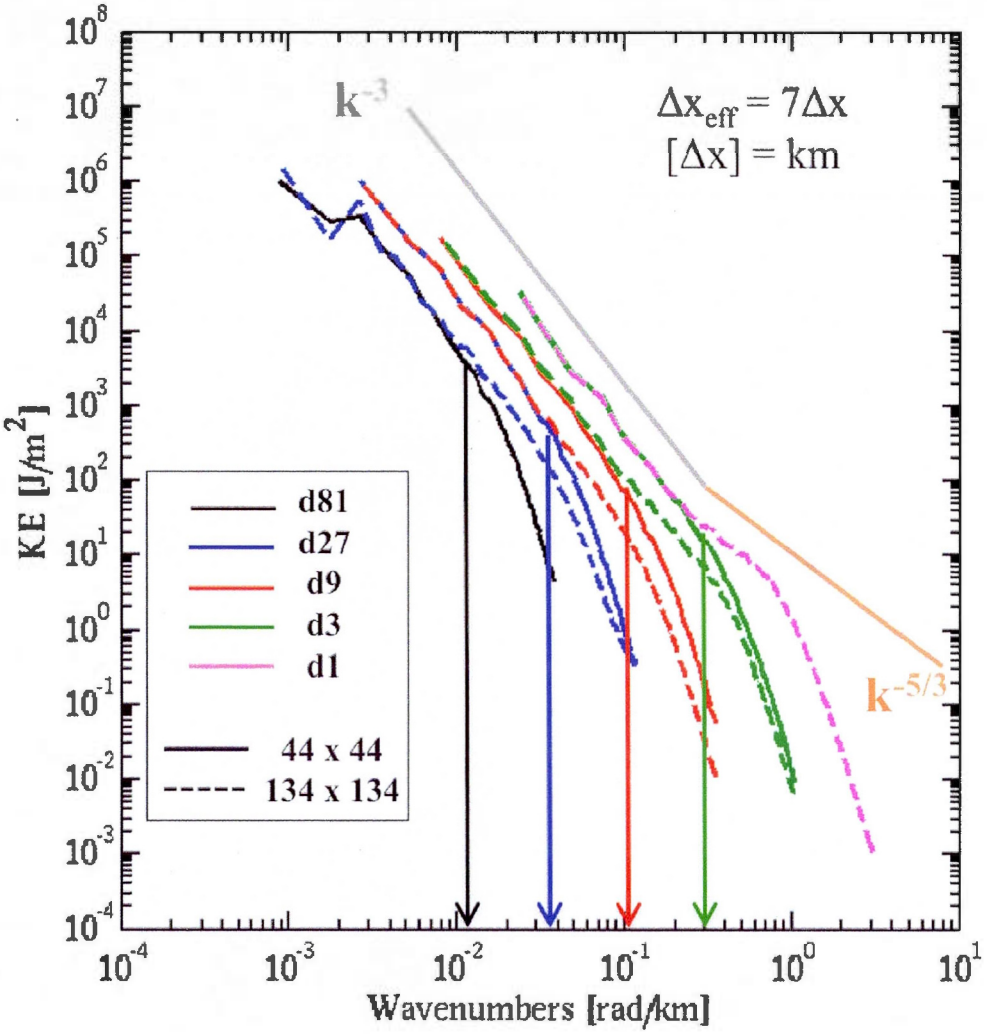

Figure 2.9 Logarithmic representation of the spatial variance spectra of horizontal KE for the d81 (black), d27 (blue), d9 (red), d3 (green) and d1 (pink) simulations. The abscissa represents the wavenumbers [rad/km] and the ordinate is the spatial variance of horizontal KE [J/m^2] vertically averaged from 700 to 200 hPa and temporally averaged over the common period (from 0000 UTC 13 February to 0000 UTC 1 March 2002). The solid lines correspond to a spatial coverage of 44 x 44 inner horizontal grid points and the dashed lines correspond to a spatial coverage of 134 x 134 inner horizontal grid points. The arrows show the effective wavenumber of each simulation. To determine the effective resolution of d3, d9, d27 and d81: the d3 (solid green line) is compared to d1 (pink dashed line), the d9 (solid red line) is compared to d3 (green dashed line), the d27 (solid blue line) is compared to d9 (red dashed line) and d81 (solid black line) is compared to d27 (blue dashed line), respectively. The grey and orange lines are the k^{-3} and $k^{-5/3}$ spectral slopes, respectively. The effective resolutions of d81, d27, d9 and d3 correspond to approximately seven times the respective grid spacing in km ($\Delta x_{eff} = 7\Delta x$).

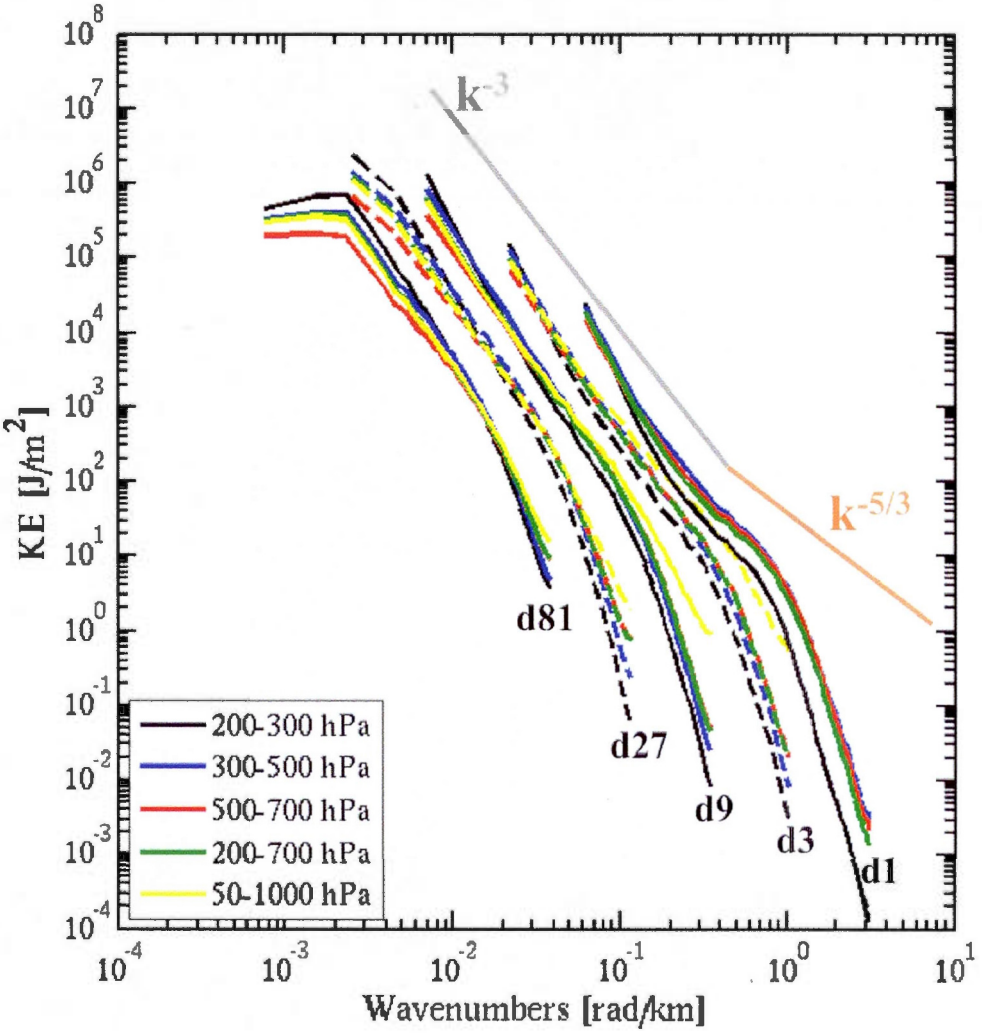

Figure 2.10 Logarithmic representation of the spatial variance spectra of horizontal KE vertically averaged over five different layers (colours shown by the legend) and computed over 50 x 50 inner horizontal grid points. The spectra are also temporally averaged over the complete period of each respective simulation (see table 2.1 for periods, excluding the first 24 hours). The abscissa represents the wavenumbers [rad/km] and the ordinate is the spatial variance of horizontal KE vertically averaged in J/m^2. The five simulations are identified in the figure with alternating line styles to better distinguish them. The grey and orange lines are the k^{-3} and $k^{-5/3}$ spectral slopes, respectively.

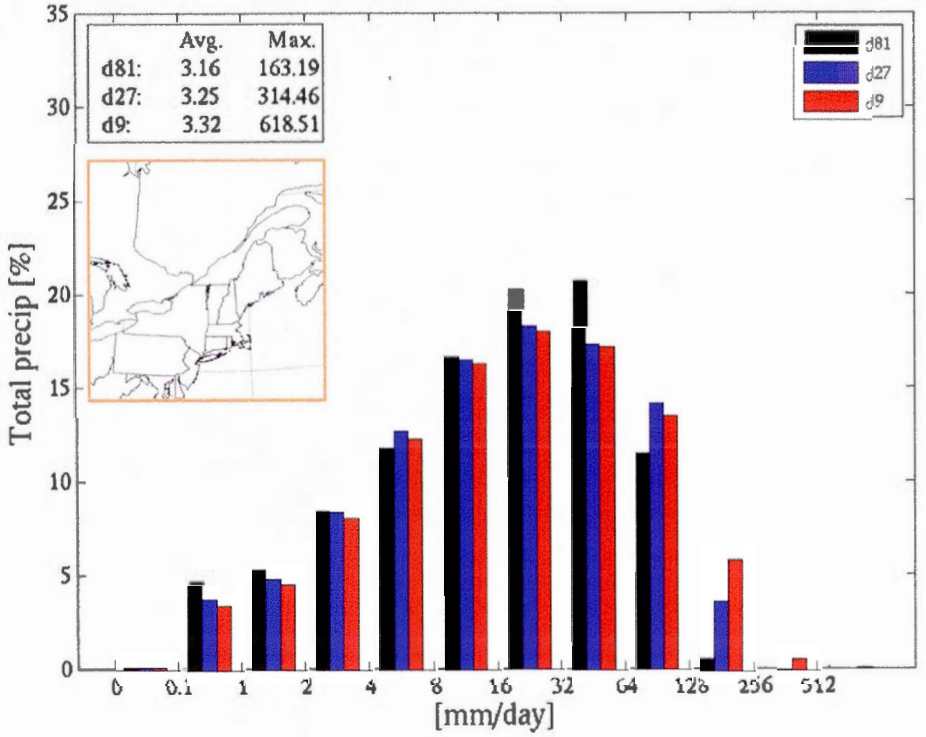

Figure 2.11 Three-hourly precipitation intensity distributions of d81 (black), d27 (blue) and d9 (red) simulations over a period from 0300 UTC 1 January to 0000 UTC 1 April 2002 and for a spatial coverage shown by the orange square. The abscissa represents the different bins of intensity [mm/day] and the ordinate is each bin/simulation pair's contribution [%] to the three-hourly mean total precipitation. The average and the maximum [mm/day] of each simulation are written top left.

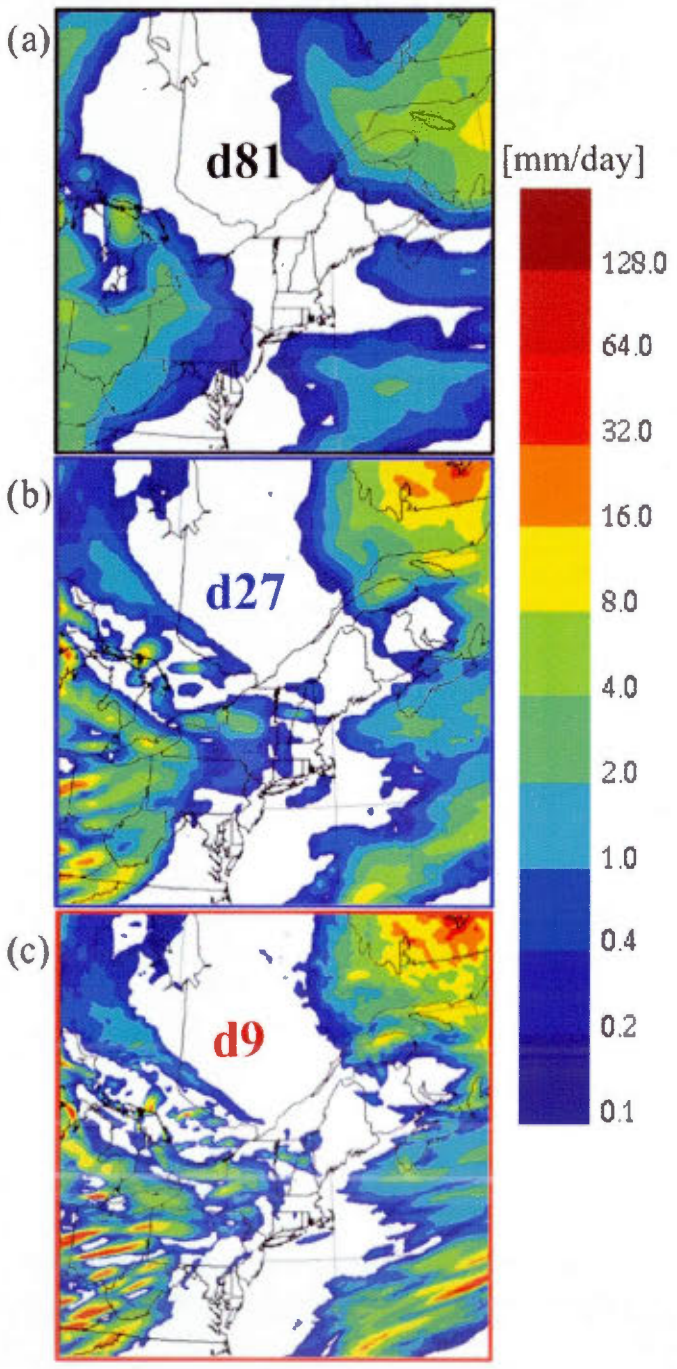

Figure 2.12 Three-hourly mean precipitation [mm/day] of the 0300 UTC 13 February 2002 time step for d81 (a), d27 (b) and d9 (c) simulations over the d9 common domain.

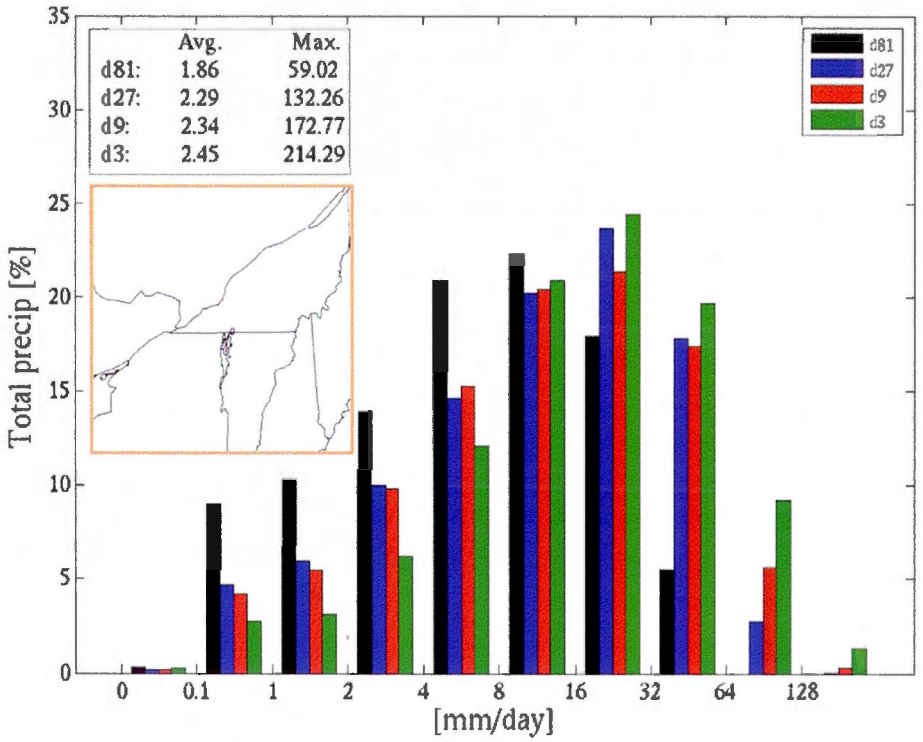

Figure 2.13 Three-hourly precipitation intensity distributions of d81 (black), d27 (blue), d9 (red) and d3 (green) simulations over a period from 0300 UTC 4 February to 0000 UTC 7 March 2002 and for a spatial coverage shown by the orange square. The abscissa represents the different bins of intensity [mm/day] and the ordinate is each bin/simulation pair's contribution [%] to the three-hourly mean total precipitation. The average and the maximum [mm/day] of each simulation are written top left.

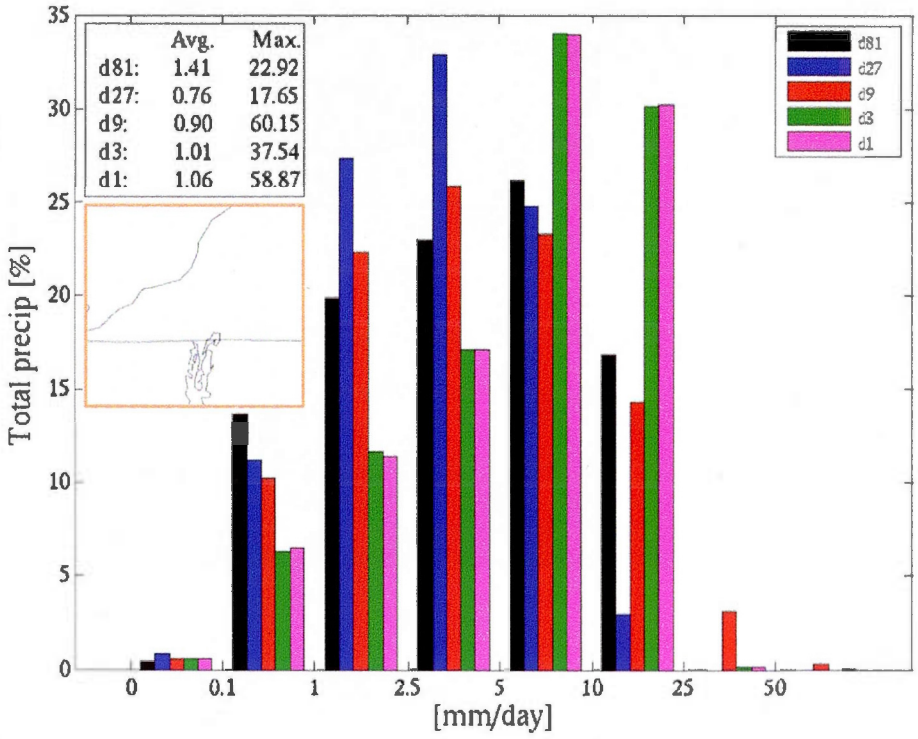

Figure 2.14 Three-hourly precipitation intensity distributions of d81 (black), d27 (blue), d9 (red), d3 (green) and d1 (pink) simulations over a period from 0300 UTC 13 February to 0000 UTC 1 March 2002 and for a spatial coverage shown by the orange square. The abscissa represents the different bins of intensity [mm/day] and the ordinate is each bin/simulation pair's contribution [%] to the three-hourly mean total precipitation. The average and the maximum [mm/day] of each simulation are written top left.

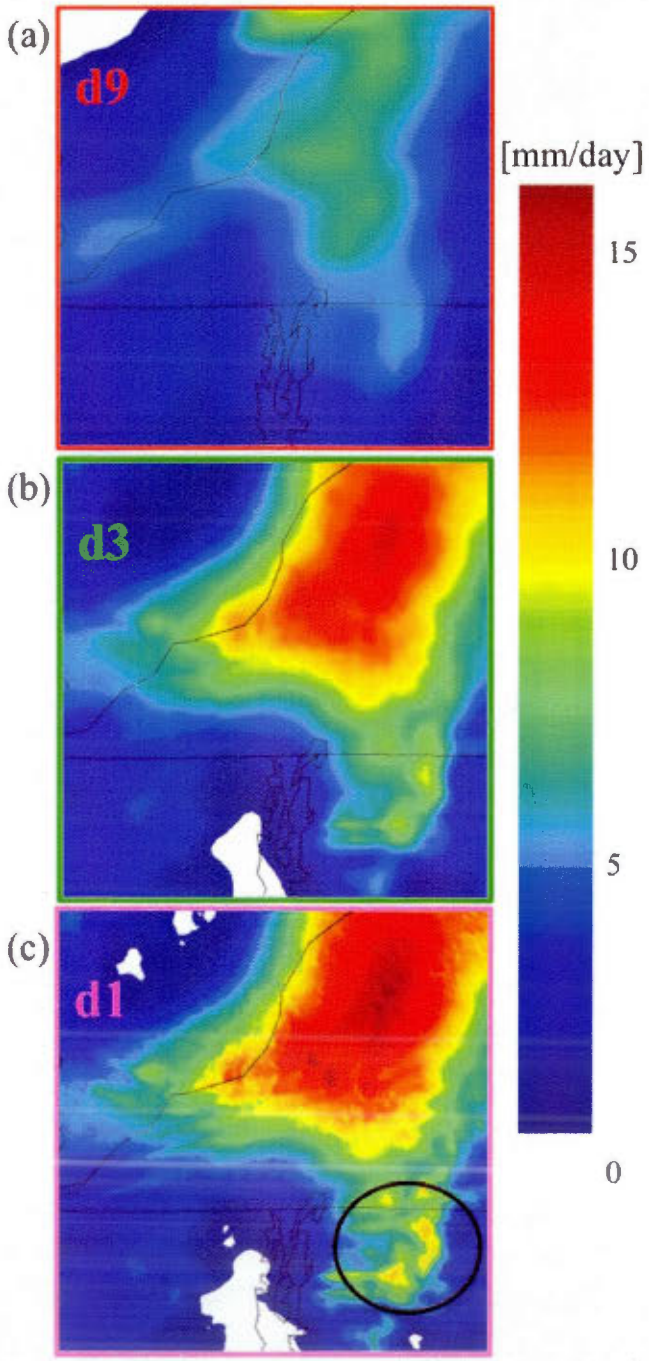

Figure 2.15 Three-hourly mean precipitation [mm/day] of the 0000 UTC 17 February 2002 time step for d9 (a), d3 (b) and d1 (c) simulations over the d1 common domain. The black circle in panel (c) represents the amplified effect of the Green Mountains.

TABLEAUX

TABLEAUX DU CHAPITRE I : TABLEAUX 1.1 À 1.5
TABLEAU DU CHAPITRE II : TABLE 2.1

Tableau 1.1 Institutions (1re colonne), MCGs, (2e colonne) évolution des résolutions [degré de latitude x degré de longitude] à travers les différentes versions (3e colonne) et les références respectives à chaque version (4e colonne).

CENTRES/Pays	MCGs	Ver.: Horiz. Rés.	Références
NCAR/États-Unis	Community Climate System Model (CCSM) Community Earth System Model (CESM)	CCSM1: 2.9° x 2.9° CCSM3: 2.9° x 2.9° CCSM3: 2° x 2.5° *CCSM4: 1.25° x 0.9°* **CESM1: 1.25° x 0.9°**	Boville and Gent (1998) Kiehl and Gent (2004) Collins et al. (2005) Gent et al. (2011) Meehl et al. (2013)
GFDL/États-Unis	Climate Model (CM) Global High Resolution Atmospheric Model (HIRAM) Earth System Model (ESM)	*CM2: 2° x 2.5°* CM3: 1.875° x 2° *HIRAM: 0.5° x 0.5°* **ESM (2M, 2G): 2° x 2.5°**	Delworth et al. (2006) Griffies et al. (2011) Zhao et al. (2009) Dunne et al. (2013)
GISS/États-Unis	Atmosphere-Ocean Model (AOM) ModelE2	AOM1: 4° x 5° *AOM2: 3° x 4°* **E2-R & E2-H: 2° x 2.5°**	Russell et al. (1995) Russell et al. (2005) Schmidt et al. (2006)
COLA/États-Unis	Coupled Global Climate Model (CGCM) Climate Forecast System (CFS)	*CGCM: 2.8° x 2.8°* CFSv1: 2.1° x 2.1° CFSv2: 0.9° x 0.9°	DeWitt & Schneider (1999) Saha et al. (2006) Saha et al. (2013)
CNRM/France	Action de Recherche Petite Échelle Grande Échelle (ARPEGE) Global Coupled Climate Model (CM)	ARPEGE: 5.6° x 5.6° CM2: 1.9° x 1.9° *CM3: 1.9° x 1.9°* **CM5: 1.4° x 1.4°**	Déqué et al. (1994) Douville et al. (2002) Salas-Mélia et al. (2005) Voldoire et al. (2013)
IPSL/France	Global Coupled Climate Model (CM)	CM1: 4° x 5.6° CM2: 4° x 5° CM3: 4° x 5° *CM4: 2.5° x 3.75°* **CM5 ESM: 1.25° x 2.5°**	Braconnot et al. (1999) Khodri et al. (2001) Li and Conil (2003) Hourdin et al. (2006) Dufresne et al. (2012)
CMCC/Italie	Climate Model (CM) Carbon Earth System Model (CESM/CMCC)	*CM: 0.75° x 0.75°* **CESM/CMCC: 3.75° x 3.75°**	Scoccimarro et al. (2011) Fogli et al. (2009)
BCCR/Norvège	Bergen Climate Model (BCM) Norwegian Earth System Model (NorESM)	*BCM1: 2.4° x 2.4°* *BCM2: 1.9° x 1.9°* **NorESM1-M: 2° x 2°** **NorESM1-ME: 2° x 2°**	Furevik et al. (2003) Otterâ et al. (2009) Bentsen et al. (2012) Tjiputra et al. (2013)
INM/Russie	Global Coupled Climate Model (CM)	*CM3: 4° x 5°* *CM4: 1.5° x 2°* **ESM: 1.5° x 2°**	Dianskii and Volodin (2002) Volodin et al. (2010) Dianskii et al. (2010)
MPI/Allemagne	Atmospheric General Circulation model (ECHAM) Earth System Model (ESM): LR=low resolution MR=mixed resolution P=paleo mode LR	*ECHAM1: 5.6° x 5.6°* ECHAM2: 4.3° x 4.3° ECHAM3: 5.6° x 5.6° ECHAM4: 2.8° x 2.8° ECHAM5: 1.9° x 1.9° *ECHAM6: 1.875° x 1.875°* **ESM (LR, MR, P): 1.9° x 1.9°**	von Storch et al. (1997) Lunkeit et al. (1996) Roeckner et al. (1992) Roeckner (1996) Roeckner (2003) Stevens et al. (2013) Giorgetta et al. (2012)
UKMO/Royaume-Uni	Hadley Centre Coupled Model (HadCM) Hadley Centre Global Environmental Model (HadGEM)	*HadCM1: 2.5° x 3.75°* HadCM2: 2.5° x 3.75° HadCM3: 2.5° x 3.75° HadCM4: 2.5° x 3.75° HadGEM1: 1.25° x 1.875° *HadGEM2: 1.25° x 1.875°* **HadGEM3: 1.25° x 1.875°**	Murphy (1995) Johns et al. (1997) Collins et al. (2001) Webb et al. (2001) Johns et al. (2006) Collins et al. (2008) Hewitt et al. (2011)

Tableau 1.1 Suite…

CENTRES/Pays	MCGs	Ver. : Horiz. Rés.	Références
BCC/Chine	Global Coupled Climate Model (CM) Climate System Model (CSM)	CM1: 1.875° x 1.875° CM2: 2.8° x 2.8° **CSM1.0: 2.8° x 2.8°** **CSM1.1: 1.9° x 1.9°** **CSM1.1(m): 0.25° x 0.25°**	Dong (2001) Wu et al. (2010) Zhang et al. (2011) Zhang and Wu (2012) Xin et al. (2012a)
LASG/Chine	Flexible Global Ocean-Atmosphere-Land System Model (FGOALS)	**FGOALS-g1: 2.8° x 2.8°** **FGOALS-s2: 1.66° x 2.8°** **FGOALS-g2: 2.8° x 2.8°**	Yu et al. (2004) Bao et al. (2013) Wang et al. (2013)
FIO/Chine	Earth System Model (ESM)	**ESM: 0.64° x 1.28°**	Bao et al. (2012)
GCESS/Chine	Beijing Normal University – Earth System Model (BNU-ESM)	**BNU-ESM: 2.8° x 2.8°**	Wang (2011)
MRI/Japon	Coupled General Circulation Model (CGCM)	CGCM1: 4° x 5° CGCM2: 2.8° x 2.8° **CGCM3/ESM1: 1.1° x 1.1°**	Tokioka et al. (1995) Yukimoto et al. (2001) Yukimoto et al. (2012)
CCSR/Japon	Model for Interdisciplinary Research On Climate (MIROC) Earth System Model (MIROC-ESM)	MIROC3m: 2.8° x 2.8° MIRCO4h: 0.56° x 0.56° MIROC5: 1.4° x 1.4° **MIROC-ESM: 2.8° x 2.8°**	Nozawa et al. (2007) Sakamoto et al. (2012) Watanabe et al. (2010) Watanabe et al. (2011)
CSIRO/Australie	Climate System Model (Mk) Australian Community Climate and Earth System Simulator (ACCESS)	Mk2.0: 3.2° x 5.6° Mk3.0: 1.9° x 1.9° Mk3.5: 1.9° x 1.9° Mk3.6: 1.875 x 1.875° **ACCESS1: 1.25° x 1.875°**	Gordon and O'Farrell (1997) Gordon et al. (2002a) Gordon et al. (2010) Collier et al. (2011) Bi et al. (2012)
CCCma/Canada	Canadian Global Coupled Model (CGCM) Canadian Earth System Model (CanESM)	CGCM1: 3.8° x 3.8° CGCM2: 3.8° x 3.8° CGCM3: 2.8° x 2.8° CGCM4:1.9° x 1.9° **CanESM1: 3.75° x 3.75°** **CanESM2: 2.81° x 2.81°**	Flato et al. (2000) Flato and Boer (2001) McFarlane et al. (2005) Scinocca et al. (2008) Christian et al. (2010) Chylek et al. (2011)

Tableau 1.2 Liste des modèles du tableau 1.1 utilisés pour le 5e rapport du GIEC (2e colonne) et leur centre de recherche respectif (1re colonne).

Centres de Recherche (Pays)	MCGs ou ESMs
NCAR (États-Unis)	CCSM4 CESM1
GFDL (États-Unis)	CM3 ESM2G ESM2M HIRAM-C180 HIRAM-C360
GISS (États-Unis)	E2-R E2-H
COLA (États-Unis)	CFSv2
CNRM (France)	CM5
IPSL (France)	CM5 ESM
CMCC (Italie)	CM CESM/CMCC
BCCR (Norvège)	NorESM1-M NorESM1-ME
INM (Russie)	CM4
MPI (Allemagne)	ESM-LR ESM-MR ESM-P
UKMO (Royaume-Uni)	HadCM3 HadGEM2
BCC (Chine)	CSM1.1(m)
LASG (Chine)	FGOALS-g2
FIO (Chine)	ESM
GCESS (Chine)	BNU-ESM
MRI (Japon)	CGCM3 ESM1
CCSR (Japon)	MIROC5
CSIRO (Australie)	Mk3.6 ACCESS1.0 ACCESS1.3
CCCma (Canada)	CanCM4 CanESM2

Tableau 1.3 MRCs (1re colonne), institutions (2e colonne), résolutions horizontales [km] (3e colonne), nombre de niveaux verticaux (4e colonne), nombre de points de grille pour la zone des CFLs (5e colonne), l'implantation ou non du mode non-hydrostatique (6e colonne) et schémas de microphysique (7e colonne). Voir liste des acronymes pour les noms des schémas et des modèles.

MRCs	Institutions	Hor. Rés.	# vertical levels	# of CFLs	Option Non-hydro?	Microphysique
CMM5 Liang et al. (2004)	NCAR	30 km	23	14	Oui	GSFC: Tao and Simpson (1989)
MM5 Grell et al. (1994)	NCAR	45 km	23	10	Oui	Dudhia scheme: Hong et al. (2004) R2: Reisner et al. (1998)
RM3 Druyan et al. (2006)	GISS	50 km	28	10	Non	CLWS: Del Genio et al. (1996)
ALADIN Farda et al. (2010)	CNRM	50 km	31	8	Oui	Mod MY: Ricard and Royer (1993)
CWRF Liang et al. (2006)	NCAR BCCR	30 km	36	14	Oui	GSFC-GCE: Tao et al. (2003)
WRF Skamarock and Klemp (2008)	NCAR	30 km	36	14	Oui	WSM6: Hong and Lim (2006)
REMO Jacob and Podzun (1997)	MPI	55 km	20	8	Non	Kessler: Kessler (1969)
HadRM3 Pope et al. (2000)	UKMO	50 km	19	8	Non	SS: Smith (1990)
CanRCM4 von Salzen et al. (2013)	CCCma	50 km	32	10	Non	PCI: Lohmann and Roeckner (1996)
CRCM4 Music and Caya (2007)	OURANOS	45 km	56	10	Oui	CGCM2: Flato and Boer (2001)
CRCM5 Hernández-Díaz et al. (2012)	ESCER-(UQAM)	45 km	56	10	Oui	CONSUN: Sundqvist et al. (1989) MYDM: Milbrandt and Yau (2005a.b)
COSMO-CLM Böhm et al. (2006)	DWD-CMCC	55 km	20	8	Oui	Kessler: Kessler (1969) SB: Seifert and Beheng (2001)

Tableau 1.3 Suite…

MRCs	Institutions	Hor. Rés.	# vertical levels	# of CFLs	Option Non-Hydro?	Microphysique
RCAO Doscher et al. (2002)	SMHI	50 km	24	8	Oui	K-scheme: Rasch and Kristjansson (1998)
HIRHAM5 Christensen et al. (2006)	DMI	50 km	19	10	Non	CONSUN: Sundqvist et al. (1989)
RegCM3 Pal et al. (2007)	ICTP-DHMZ-BCC	50 km	16	11	Non	SUBEX: Pal et al. (2000)
PROMES Castro et al. (1993)	UCM	50 km	28	10	Non	PCP: Hsie et al. (1984)
CHRM Vidale et al. (2003)	GSMS	55 km	20	8	Non	Kessler: Kessler (1969)
RACMO2 Lenderink et al. (2003)	KNMI	50 km	31	8	Non	MOISTKE: Tiedtke (1989)

Tableau 1.4 MRCs du tableau 1.3 (1re colonne), schémas de surface (2e colonne), schémas de couche limite (3e colonne), schémas de radiation (4e colonne) et schémas de convection (5e colonne). Voir liste des acronymes pour les noms des schémas et des modèles.

MRCs	Surface	Couche Limite	Radiation	Convection
CMM5	Noah: Chen and Dudhia (2001)	MRF: Hong and Pan (1996)	CCM2: Hack et al. (1993)	GR: Grell (1993)
MM5	Noah: Chen and Dudhia (2001)	MRF: Hong and Pan (1996)	Dudhia SW: Dudhia (1989) RRTM LW: Mlawer et al. (1997)	KFC2: Kain (2004)
RM3	LS: Rosenzweig and Abramopoulos (1997)	K-scheme: Rasch and Kristjansson (1998)	GLAS/UCLA LW: Harshvardhan et al. (1987) SW rad: Davies (1987)	GISS scheme: Del Genio and Yao (1993)
ALADIN	ISBA: Noilhan and Planton (1989)	MY2.0: Mellor and Yamada (1982)	FMR: Morcrette (1989)	ARPEGE: Bougeault (1985)
CWRF	CSSP: Choi et al. (2007)	CAM3: Holtslag and Boville (1993)	GSFC: Chou et al. (2001)	ECP mod G3: Qiao and Liang (2012)
WRF	Noah: Ek et al. (2003)	YSU: Hong et al. (2006)	CAM3: Collins et al. (2004)	G3: new GD: Grell and Dévényi (2002)
REMO	ARNO: Todini (1996)	MY2.0: Mellor and Yamada (1982)	CRS: Ritter and Geleyn (1992)	MoisTKE: Tiedtke (1989)
HadRM3	MOSES2: Essery et al. (2003)	SS: Smith (1993)	Mod-FMR: Gregory et al. (2000)	GRCS: Gregory and Rowntree (1990)
CanRCM4	CLASS2.7: Verseghy (1991)	VSMF: von Salzen and McFarlane (2002)	CKRS: Li and Barker (2005)	ZMFS: Zhang and McFarlane (1995)
CRCM4	CLASS2.7: Verseghy (1991)	NBLMS: Jiao and Caya (2006)	GCM3: Puckrin et al. (2004)	BFK: Bechtold et al. (2001)
CRCM5	CLASS3.5: Verseghy (2000)	MOISTKE: Tiedtke (1989)	CKRS: Li and Barker (2005)	KFC: Kain and Fritsch (1990) KSCCS: Kuo (1965)
COSMO-CLM	TERRA_LM: Doms et al. (2005)	MY2.0: Mellor and Yamada (1982)	CRS: Ritter and Geleyn (1992)	MOISTKE: Tiedtke (1989) KFC: Kain and Fristch (1990)

Tableau 1.4 Suite…

MRCs	Surface	Couche Limite	Radiation	Convection
RCAO	LSS: Sellers et al. (1997)	CBR: Cuxart et al. (2000)	FRPS: Savijärvi (1990)	KFC: Kain and Fritsch (1990)
HIRHAM5	ARNO: Todini (1996)	Moist CBR: Tijm and Lenderink (2003)	FRPS: Savijärvi (1990)	MOISTKE: Tiedtke (1989)
RegCM3	BATS1e: Dickinson et al. (1993)	CAM3: Holstlag and Boville (1993)	CCM3: Keihl et al. (1996)	GR: Grell (1993) MIT: Emanuel (1991)
PROMES	SECHIBA: Ducoudré et al. (1993)	CBR: Cuxart et al. (2000)	RPEWC: Stephens (1978)	KFC: Kain and Fritsch (1990)
CHRM	BATS: Dickinson et al. (1993)	MY2.0: Mellor and Yamada (1982)	CRS: Ritter and Geleyn (1992)	MOISTKE: Tiedtke (1989)
RACMO2	TESSEL: White (2001)	DualM-TKE: Lenderink et al. (2005)	FMR: Morcrette (1989)	MOISTKE: Tiedtke (1989)

Tableau 1.5 Identification des MRCs du tableau 1.3 (1re colonne) dans les différents projets (colonnes 2 à 8) utilisant un ensemble de MRCs. Les MRCs en rouge sont absents du tableau 1.3. Voir liste des acronymes pour les noms des projets et des modèles.

MRCs \ Projets	PRUDENCE	NARCCAP	RMIP	ENSEMBLES	CORDEX	ARCMIP	CLARIS
CRCM		X		X	X		
ALADIN	X			X	X		
WRF		X			X		X
MM5		X	X		X		X
HadRM	X	X		X			
RCAO	X			X	X		X
HIRHAM	X			X	X	X	
REMO	X			X	X	X	X
COSMO-CLM	X			X	X		
RegCM	X	X	X	X	X		
PROMES	X			X			X
CHRM	X						
CanRCM4					X		
RACMO	X			X	X		
PRECIS					X		
REIMS			X				
MRI			X				
CSIRO			X				
SNU-RCM			X				
COAMPS						X	

Table 2.1 The CRCM5 cascade specifications: d81 (2nd column), d27 (3th column), d9 and d9_pilots (4th and 5th columns, respectively), d3 (6th column), and d1 (7th column). The first row represents the grids description, the second row is the time characteristics, the third row is the parameterization schemes and the fourth row is the LBCs' specifications.

	d81	**d27**	**d9**	**d9_pilots**	**d3**	**d1**
Grids description						
Grid spacing [°]	0.81	0.27	0.09	0.09	0.03	0.01
Grid spacing [km]	~81	~27	~9	~9	~3	~1
Grid size (N_x x N_y)	200 x 200	225 x 225	225 x 225	225 x 225	225 x 225	225 x 225
# vertical levels (N_z)	56	56	56	56	56	56
Time characteristics						
Model time step	30 min	10 min	200 s	200 s	1 min	20 s
Output time step	3 h	3 h	1 h	1 h	20 min	5 min
Length of sim.	6 months	4 months	3 months	3 months	1 month	15 days
Period	Oct. 1st 2001 to Apr. 1st 2002	Dec. 1st 2001 to Apr. 1st 2002	Jan. 1st to Apr. 1st 2002	Jan. 1st to Apr. 1st 2002	Feb. 4th to Mar. 7th 2002	Feb. 12th to Mar. 1st 2002
Parameterizations						
Surface	CLASS3.5	CLASS3.5	CLASS3.5	CLASS3.5	CLASS3.5	CLASS3.5
Radiation	CKRS	CKRS	CKRS	CKRS	CKRS	CKRS
Shallow convection	KSCCS	KSCCS	KSCCS	KSCCS	KSCCS	KSCCS
Boundary clouds	MOISTKE	MOISTKE	MOISTKE	MOISTKE	MOISTKE	MOISTKE
Condensation	CONSUN	CONSUN	CONSUN	MYDM	MYDM	MYDM
Precipitation types	bourge 3D	bourge 3D	bourge 3D	nil	nil	nil
Convection	KFC	KFC	KFC	KFC	nil	nil
Gravity wave drag	GWD86	GWD86	GWD86	GWD86	nil	nil
Hydrostatic?	yes	yes	yes	yes	no	no
Boundary conditions						
Driving data	ERAInterim	**d81**	d27	d27	d9_pilots	d3
Driving time interval	6 h	3 h	1 h	1h	20 min	5 min

ANNEXE A

FIGURES SUPPLÉMENTAIRES N'AYANT PAS ÉTÉ PRÉSENTÉES DANS LE CHAPITRE II, MAIS DISCUTÉES INDIRECTEMENT

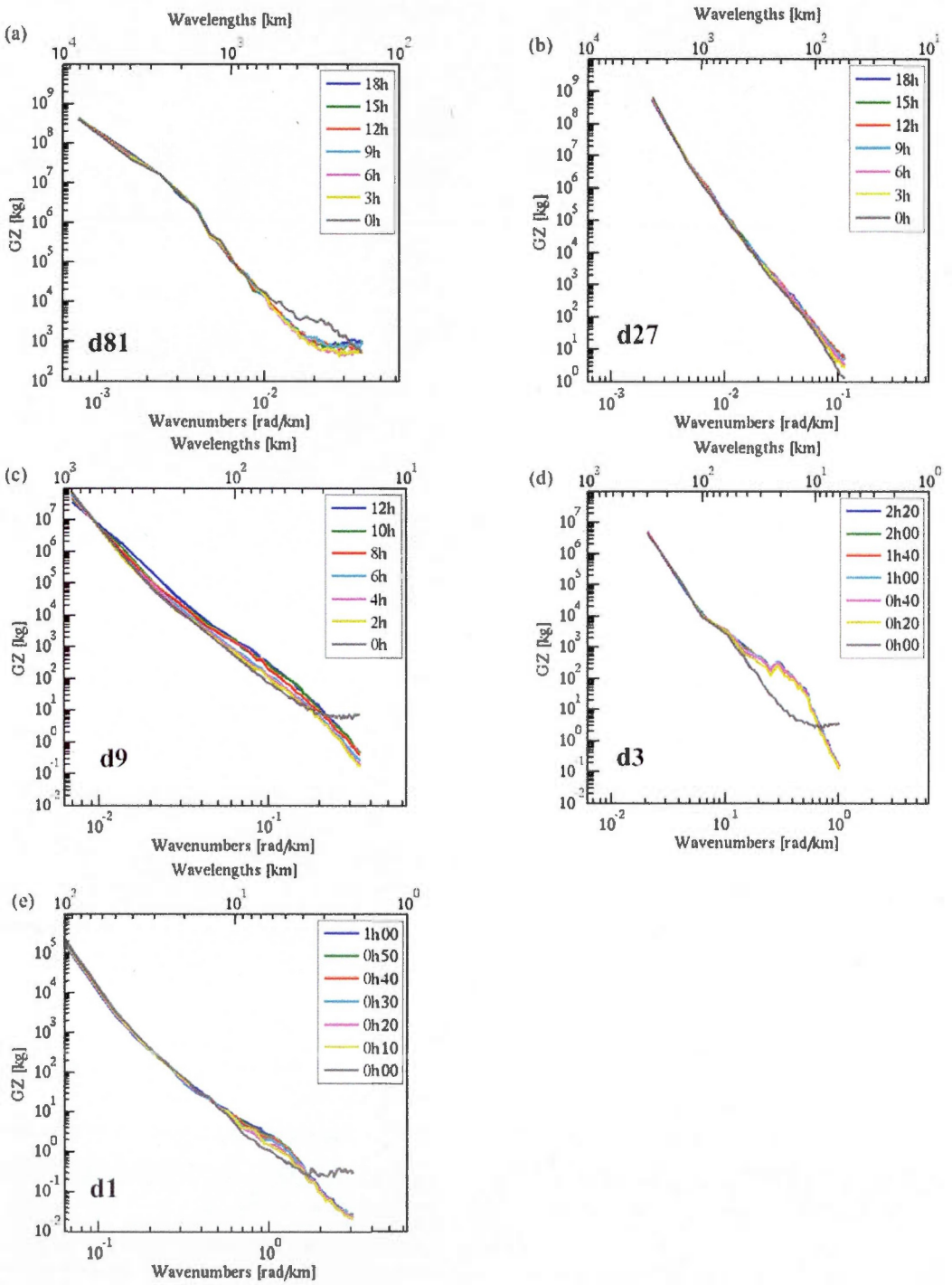

Figure A.1 Logarithmic representation of the geopotential height spatial variance spectra vertically averaged from 700 to 200 hPa over 50 x 50 inner horizontal grid points of the initial states of each simulation: d81 (a), d27 (b), d9 (c), d3 (d) and d1 (e). The different line colors correspond to the time step identified by the legend of each panel. The abscissas represent the wavenumbers [rad/km], the upper abscissas are the wavelengths [km] and the ordinates are the spatial variance of geopotential height [kg] vertically averaged.

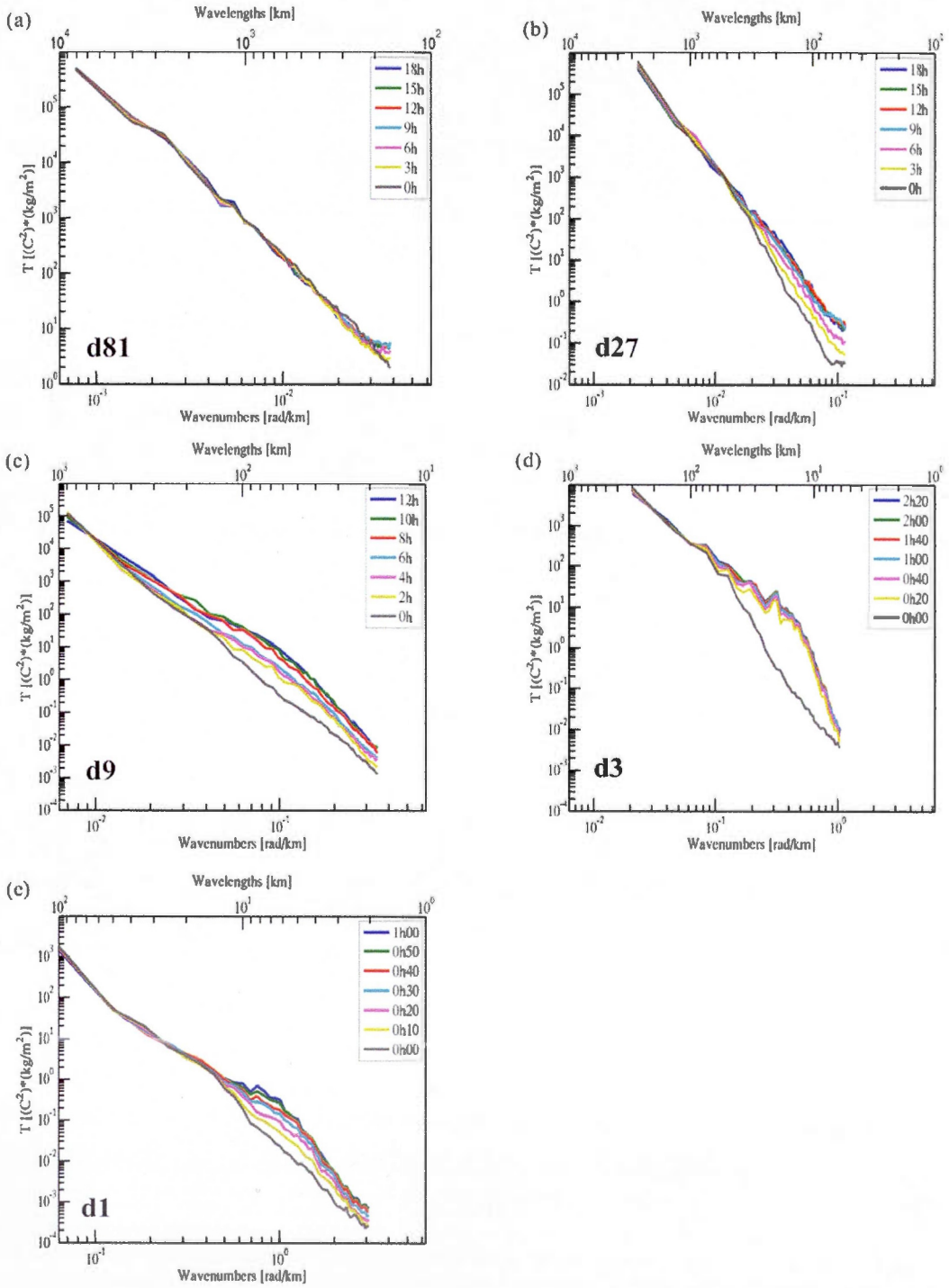

Figure A.2 Logarithmic representation of the temperature spatial variance spectra vertically averaged from 700 to 200 hPa over 50 x 50 inner horizontal grid points of the initial states of each simulation: d81 (a), d27 (b), d9 (c), d3 (d) and d1 (e). The different line colors correspond to the time step identified by the legend of each panel. The abscissas represent the wavenumbers [rad/km], the upper abscissas are the wavelengths [km] and the ordinates are the spatial variance of temperature [$(°C^2)*(kg/m^2)$] vertically averaged.

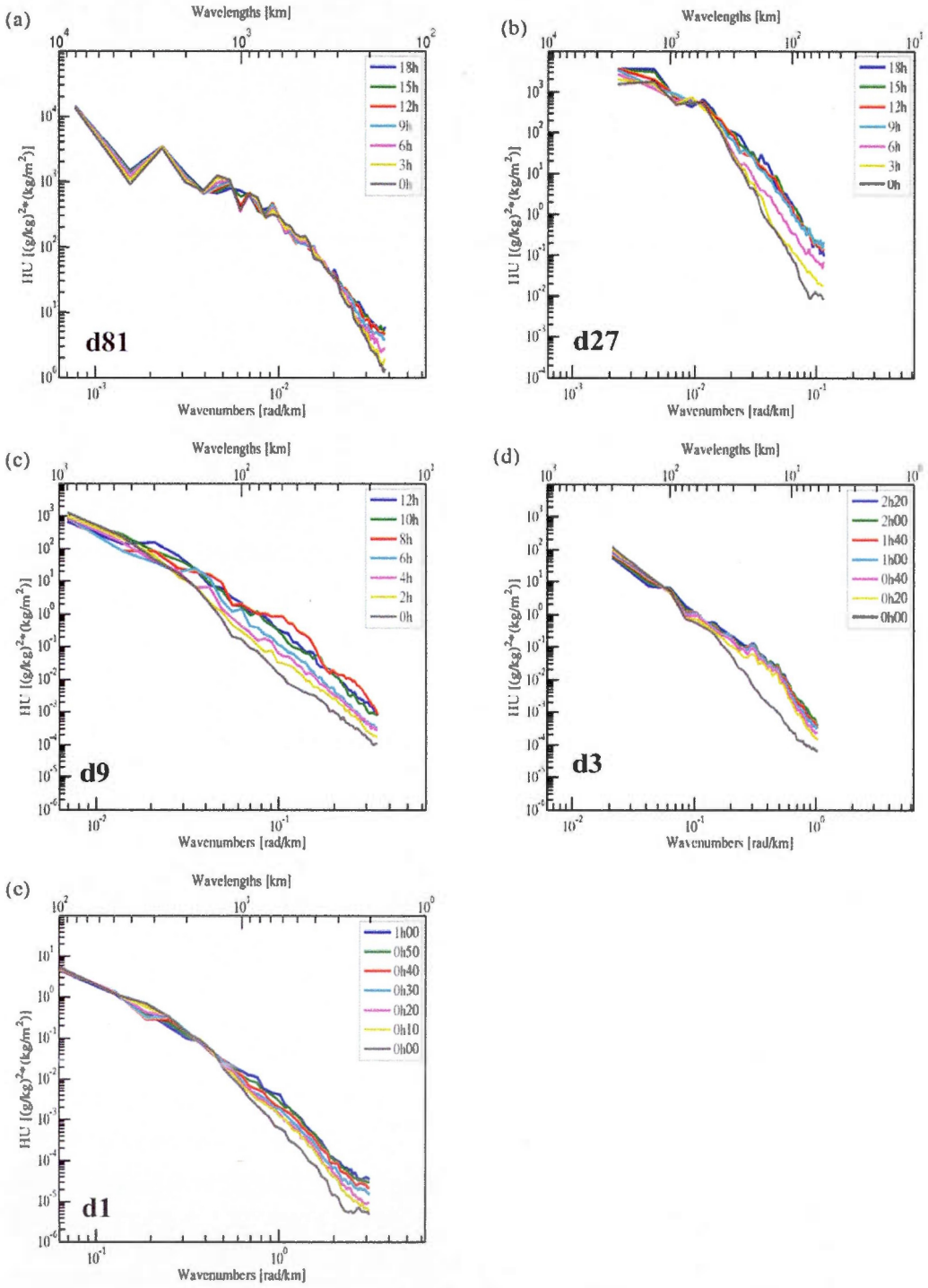

Figure A.3 Logarithmic representation of the specific humidity spatial variance spectra vertically averaged from 700 to 200 hPa over 50 x 50 inner horizontal grid points of the initial states of each simulation: d81 (a), d27 (b), d9 (c), d3 (d) and d1 (e). The different line colors correspond to the time step identified by the legend of each panel. The abscissas represent the wavenumbers [rad/km], the upper abscissas are the wavelengths [km] and the ordinates are the spatial variance of specific humidity $[(g/kg)^2*(kg/m^2)]$ vertically averaged.

CHAPITRE IV

RÉFÉRENCES

Ahmed, N., T. Natarajan, and K. R. Rao (1974). Discrete Cosine Transform. *IEEE Transactions on Computers*, *100*(1), 90-93.

Alexandru, A., R. de Elia, and R. Laprise (2007). Internal variability in regional climate downscaling at the seasonal scale. *Monthly Weather Review*, *135*(9), 3221-3238.

Arakawa, A., and J. M. Chen (1987). Closure assumptions in the cumulus parameterization problem. *Short- and Medium-Range Numerical Weather Prediction*, 107-131.

Balmino, G. (1993). The spectra of topography of the Earth, Venus and Mars. *Geophysical Research Letters*, *20*, 1063-1066.

Ban, N., J. Schmidli, and C. Schär (2013, mars). *Evaluation of a 10-year cloud-resolving climate simulation driven by ERA-Interim.* Communication donnée lors du COSMO/CLM User seminar, Institute for Atmospheric and Climate Science, ETH Zürich.

Bao, Q., P. Lin, T. Zhou, Y. Liu, Y. Yu, G. Wu, B. He, J. He, L. Li, J. Li, Y. Li, H. Liu, F. Qiao, Z. Song, B. Wang, J. Wang, P. Wang, X. Wang, Z. Wang, B. Wu, W. Zheng, and L. Zhou (2013). The Flexible Global Ocean-Atmosphere-Land System Model, Spectral Version 2: FGOALS-s2. *Advances in Atmospheric Sciences, 3*, 561-576.

Bao, Y., F. L. Qiao, and Z. Y. Song (2012) The historical global carbon cycle simulation of FIO-ESM. *European Geosciences Union General Assembly Conference Abstracts*, *14*, 6834.

Bechtold, P., J. S. Kain, E. Bazile, F. Guichard, P. Mascart, and E. Richard (2001). A mass flux convection scheme for regional and global models. *Quarterly Journal of Royal Meteorology Society, 127*, 869-886.

Beck, A., B. Ahrens, and K. Stadlbacher (2004). Impact of nesting strategies in dynamical downscaling of reanalysis data. *Geophysical Research Letters, 31*, L19101, doi: 10.1029/2004GK020115

Bélair, S., J. Mailhot, E. Girard, and P. Vaillancourt (2005). Boundary-layer and shallow cumulus clouds in a medium-range forecast of a large-scale weather system. *Monthly Weather Review, 133*, 1938-1960.

Bengtsson, L., M. Steinheimer, P. Bechtold, and J. F. Geleyn (2013). A stochastic parametrization for deep convection using cellular automata. *Quarterly Journal of the Royal Meteorological Society, 139,* 1533-1543, DOI: 10.1002/qj.2108

Benoit, R., J. Côté, and J. Mailhot (1989). Inclusion of TKE boundary layer parameterization in the Canadian Regional Finite-Element Model. *Monthly Weather Review, 117*, 1726-1750.

Bentsen, M., I. Bethke, J. B. Debernard, T. Iversen, A. Kirkevåg, Ø. Seland, H. Drange, C. Roelandt, I. A. Seierstad, C. Hoose, and J. E. Kristjánsson (2012). The Norwegian Earth System Model, NorESM1-M-Part 1: Description and basic evaluation. *Geoscientific Model Development Discussions, 5*, 2843-2931.

Bi, D., M. Dix, S. J. Marsland, S. O'Farrell, H. Rashid, P. Uotila, A. C. Hirst, E. Kowalczyk, M. Golebiewski, A. Sullivan, H. Yan, N. Hannah, C. Franklin, Z. Sun, P. Vohralik, I. Watterson, X. Zhou, R. Fiedler, M. Collier, Y. Ma, J. Noonan, L. Stevens, P. Uhe, H. Zhu, S. M. Griffies, R. Hill, C. Harris, and K. Puri (2012). The ACCESS Coupled Model: Description, Control Climate and Evaluation. *Australia Meteorological Oceanography Journal, 63*, 41-64.

Boer, G. J., and T. G. Shepherd (1983). Large-scale two-dimensional turbulence in the atmosphere. *Journal of Atmospheric Sciences, 40*, 164-184.

Boer, G. J. (1994). Predictability regimes in atmospheric flow. *Monthly Weather Review, 122*(10), 2285-2295.

Böhm, U., M. Kücken, W. Ahrens, A. Block, D. Hauffe, K. Keuler, B. Rockel, and A.Will (2006). CLM The climate version of LM: Brief Descripition and long-term applications. *Consortium for Small-scale Modeling Newsletter, 6*, 225-235.

Bougeault, P. (1985). A simple parameterization of the large-scale effects of cumulus convection. *Monthly Weather Review, 113*, 21082121.

Bourgouin, P. (2000) A method to determine precipitation types. *Weather and Forecasting, 15*, 583-592.

Boville, B. A., and P. R. Gent (1998). The NCAR Climate System Model, Version One. *Journal of Climate, 11*(6), 1115-1130.

Braconnot, P., S. Joussaume, O. Marti, and N. De Noblet (1999). Synergistic feedbacks from ocean and vegetation on the African Monsoon response to Mid Holocene insolation. *Geophysical Research Letters, 26*(16), 2481-2484.

Bryan, G. H., J. C. Wyngaard, and J. M. Fritsch (2003). Resolution requirements for the simulation of deep moist convection. *Monthly Weather Review, 131*(10), 2394-2416.

Carrera, M. L., J. R. Gyakum, and C. A. Lin (2009). Observational study of wind channeling within the St-Lawrence River valley. *Journal of Applied Meteorology and Climatology, 98*, 2341-2361.

Castro M., C. Fernandez, and M. A. Gaertner (1993). Description of a meso-scale atmospheric numerical model. *Diaz JI, Lions JL (eds) Mathematics, Climate and Environment,* Mason, 230-253.

Charney, J. G., and N. A. Phillips (1953). Numerical integration of the quasi-geostrophic equations for barotropic and simple baroclinic flows. *Journal of Atmospheric Sciences, 10*, 71-99.

Charney, J. G. (1971). Geostrophic turbulence. *Journal of Atmospheric Sciences, 28*, 1087-1095.

Chen, F., and J. Dudhia (2001). Coupling an advanced land surface hydrology model with the Penn State NCAR MM5 modeling system. Part I: Model implementation and sensitivity. *Monthly Weather Review, 129*, 569-585.

Chen, J. H., and K. Miyakoda (1974). A nested grid computation for the barotropic free surface atmosphere. *Monthly Weather Review, 102*, 181-190.

Choi, H. I., P. Kumar, and X.-Z. Liang (2007). Three-dimensional volume-averaged soil moisture transport model with a scalable parameterization of subgrid topographic variability. *Water Resource Research, 43*, W04414, doi: 10.1029/2006WR005134

Chou, M.-D., M. J. Suarez, X.-Z. Liang, and M.-H. Yan (2001). *A thermal infrared radiation parameterization for atmospheric studies.* (NTIS: 0125). USA: National Aeronautics and Space Administration / Goddard Space Flight Center (NASA/GSFC), 19, 68 pp.

Christensen, J. H., and O. B. Christensen (2007). A summary of the PRUDENCE model projections of changes in European climate by the end of this century. *Climatic Change*, *81*, 7-30.

Christensen, O. B., M. Drews, J. H. Christensen, K. Dethloff, K. Ketelsen, I. Hebestadt, and A. Rinke (2006). *The HIRHAM regional climate model, version 5.* (DMI: 06-17). Copenhagen: Danish Meteorological Institute. Available online at http://www.dmi.dk/dmi/tr06-17.pdf

Christian, J. R., V. K. Arora, G. J. Boer, C. L. Curry, K. Zahariev, K. L. Denman, G. M. Flato, W. G. Lee, W. J. Merryfield, N. T. Roulet, and J. F. Scinocca (2010). The global carbon cycle in the Canadian Earth system model (CanESM1): Preindustrial control simulation. *Journal of Geophysical Research*, *115*(G3), G03014.

Chylek P., J. Li, M. Dubey, M. Wang, and G. Lesins (2011). Observed and model simulated 20th century arctic temperature variability: Canadian earth system model canesm. *Atmospheric Chemistry and Physics*, *11*(22), 893-907.

Clark, T. L., and R. D. Farley (1984). Severe downslope windstorm calculations in two and three spatial dimensions using anelastic interactive grid nesting: A possible mechanism for gustiness. *Journal of the Atmospheric Sciences*, *41*(3), 329-350.

CMIP-Coupled Model Intercomparison Project. (2013). *PCMDI Program for Climate Model Diagnosis and Intercomparison.* En ligne. < http://cmip-pcmdi.llnl.gov/>. Consulté le 20 avril 2013.

Collier, M. A., S. J. Jeffrey, L. D. Rotstayn, K. K. Wong, S. M. Dravitzki, C. Moseneder, C. Hamalainen, J. I. Syktus, R. Suppiah, J. Antony, A. E. Zein, and M. Artif (2011, december). *The CSIRO-Mk3. 6.0 Atmosphere-Ocean GCM: participation in CMIP5 and data publication.* Communication donnée à l'International Congress on Modelling and Simulation (19th MODSIM), Australia.

Collins, M., S. F. B. Tett, and C. Cooper (2001). The internal climate variability of HadCM3, a version of the Hadley Centre coupled model without flux adjustments. *Climate Dynamics*, *17*(1), 61-81.

Collins, W. D., P. J. Rasch, B. A. Boville, J. J. Hack, J. R. McCaa, D. L. Williamson, J. T. Kiehl, B. Briegled, C. Bitz, S.-J. Lin, M. Zhang, and Y. Dai (2004). *Description of the NCAR community atmosphere model (CAM 3.0).* (NCAR / TN-464+STR). USA: National Center for Atmospheric Research.

Collins, W. D., C. M. Bitz, M. L. Blackmon, G. B. Bonan, C. S. Bretherton, J. A. Carton, P. Chang, S. C. Doney, J. J. Hack, T. B. Henderson, J. T. Kiehl, W. G. Large, D. S. McKenna, B. D. Santer, and R. D. Smith (2005). The Community Climate System Model Version 3 (CCSM3). *Journal of Climate*, *19*, 2122-2143.

Collins, W. J., N. Bellouin, M. Doutriaux-Boucher, N. Gedney, T. Hinton, C. D. Jones, S. Liddicoat, G. Martin, F. O'Connor, J. Rae, C. Senior, I. Totterdell, S. Woodward, T. Reichler, and J. Kim (2008). *Evaluation of the HadGEM2 model.* (TN-74). United Kingdom: Hadley Center (UKMO).

Cortinas, J. (2000). A climatology of freezing rain in the great lakes region of North America. *Monthly Weather Review*, *128*(10), 3574-3588.

Cortinas, Jr. J. V., B. C. Bernstein, C. C. Robbins, and J. W. Strapp (2004). An analysis of freezing rain, freezing drizzle, and ice pellets across the United States and Canada: 1976-90. *Weather and Forecasting*, *19*(2), 377-390.

Côté, J., S. Gravel, A. Méthot, A. Patoine, M. Roch, and A. Staniforth (1998). The operational CMC-MRB Global Environmental Multiscale (GEM) model: Part I – Design considerations and formulation. *Monthly Weather Review*, *126*, 1373-1395.

Côté, J., J.-G. Desmarais, S. Gravel, A. Méthot, A. Patoine, M. Roch, and A. Staniforth (1998). The operational CMC-MRB Global Environmental Multiscale (GEM) model: Part II – Results. *Monthly Weather Review*, *126*, 1397-1418.

Craig, G. C., and A. Dörnbrack (2008). Entrainment in cumulus clouds: What resolution is cloud-resolving? *Journal of the Atmospheric Sciences*, *65*(12), 3978-3988.

Curry, J. A., and A. H. Lynch (2002). Comparing arctic regional climate model. *Eos, Transactions American Geophysical Union*, *83*(9), 87.

Cuxart, J., P. Bougeault, and J.-L. Redelsperger (2000). A turbulence scheme allowing for mesoscale and large-eddy simulations. *Quarterly Journal of Royal Meteorology Society, 126*, 1-30.

Davies, H. C. (1976). A lateral boundary formulation for multi-level prediction models. *Quarterly Journal of the Royal Meteorological Society*, *128*, 689-708.

Davies, R., D. A. Randall, and T. G. Corsetti (1987). A fast radiation parameterization for atmospheric circulation models. *Journal of Geophysical Research: Atmospheres (1984–2012)*, *92*(D1), 1009-1016.

Del Genio, A. D., and M.-S. Yao (1993). Efficient cumulus parameterization for long-term climate studies: The GISS scheme. The Representation of Cumulus Convection in Numerical Models. *Meteorology Monography*, *46*, 181-184.

Del Genio, A., M.-S. Yao, W. Kovari, and K.-W. Lo (1996). A prognostic cloud water parameterization for global climate models. *Journal of Climate*, *9*, 270-304.

Delworth, T. L., A. J. Broccoli, A. Rosati, R. J. Stouffer, V. Balaji, J. A. Beesley, W. F. Cooke, K. W. Dixon, J. Dunne, K. A. Dunne, J. W. Durachta, K. L. Findell, P. Ginoux, A. Gnanadesikan, C. T. Gordon, S. M. Griffies, R. Gudgel, M. J. Harrison, I. M. Held, R. S. Hemler, L. W. Horowitz, S. A. Klein, T. R. Knutson, P. J. Kushner, A. R. Langenhorst, H.-C. Lee, S.-J. Lin, J. Lu, S. L. Malyshev, P. C. D. Milly, V. Ramaswamy, J. Russell, M. D. Schwarzkopf, E. Shevliakova, J. J. Sirutis, M. J. Spelman, W. F. Stern, M. Winton, A. T. Wittenberg, B. Wyman, F. Zeng, and R. Zhang (2006). GFDL's CM2 global coupled climate models. Part I: Formulation and simulation characteristics. *Journal of Climate*, *19*(5), 643-674.

Deng, A., and D. R. Stauffer (2006). On improving 4-km mesoscale model simulations. *Journal of Applied Meteorology and Climatology*, *45*(3), 361-381.

Denis, B., J. Côté, and R. Laprise (2002). Spectral decomposition of two-dimensional atmospheric fields on limited-area domains using the Discrete Cosine Transform (DCT). *Monthly Weather Review*, *130*, 1812-1829.

Denis, B., R. Laprise, and D. Caya (2003). Sensitivity of a regional climate model to the resolution of the lateral boundary conditions. *Climate Dynamics*, *20*(2-3), 107-126.

Déqué M., C. Dreveton, A. Braun, and D. Cariolle (1994). The ARPEGE-IFS atmosphere model: a contribution to the French community climate modelling. *Climate Dynamics, 10*, 249-266.

Dewan, E. M. (1979). Stratospheric spectra resembling turbulence. *Science*, *402*, 832-835.

DeWitt, D. G., and E. K. Schneider (1999). The processes determining the annual cycle of equatorial sea surface temperature: A coupled general circulation model perspective. *Monthly Weather Review*, *127*(3), 381-395.

Diaconescu, E. P., R. Laprise, and L. Sushama (2007). The impact of lateral boundary data errors on the simulated climate of a nested regional climate model. *Climate Dynamics*, *28*(4), 333-350.

Dianskii, N. A., and E. M. Volodin (2002). Simulation of present-day climate with a coupled atmosphere-ocean general circulation model. *Izvestiya, Atmospheric and Oceanic Physics*, *38*, 732-747.

Dianskii, N. A., V. Y. Galin, A. V. Gusev, S. P. Smyshlyaev, E. M. Volodin, and N. G. Iakovlev (2010). The model of the Earth system developed at the INM RAS. *Russian Journal of Numerical Analysis and Mathematical Modelling*, *25*(5), 419-429.

Dickinson, R. E., R. M. Errico, F. Giorgi, and G. T. Bates (1989). A regional climate model for the western United States. *Climatic Change*, *15*(3), 383-422.

Dickinson, R. E., A. Henderson-Sellers, and P. J. Kennedy (1993). *Biosphere-atmosphere transfer scheme (bats) version 1e as coupled to the ncar community climate model.* (NCAR-TN). USA: National Center for Atmospheric Research.

Doms, G., J. Förstner, E. Heise, H.-J. Herzog, M. Raschendorfer, R. Schrodin, T. Rhein-Hardt, and G. Vogel (2005). *A description of the non-hydrostatic regional model LM. Part II: physical parameterisation.* Printed at Deutscher Wetterdienst, Offenbach, Germany. [Available online at: www.cosmo-model.org]

Done, J. M., G. J. Holland, C. L. Bruyère, L. R. Leung, and A. Suzuki-Parker (2012). *Modeling high-impact weather and climate: lessons from a tropical cyclone perspective.* (NCAR-TN-490+STR). USA: National Center for Atmospheric Research.

Dong, M. (2001). Introduction to National Climate Center Atmospheric general Circulation Model documentation-basic principles and applications. *China Meteorological Press*, 152 pp.

Döscher, R., U. Willén, C. Jones, A. Rutgersson, H. M. Meier, U. Hansson, and L. P. Graham (2002). The development of the regional coupled ocean-atmosphere model RCAO. *Boreal Environment Research*, *7*(3), 183-192.

Douville, H., F. Chauvin, S. Planton, J. F. Royer, D. Salas-Melia, and S. Tyteca (2002). Sensitivity of the hydrological cycle to increasing amounts of greenhouse gases and aerosols. *Climate Dynamics*, *20*(1), 45-68.

Druyan, L. M., M. Fulakeza, and P. Lonergan (2006). Mesoscale analyses of West African summer climate: focus on wave disturbances. *Climate Dynamics*, *27*(5), 459-481.

Ducoudré, N., K. Laval, and A. Perrier (1993). Sechiba, a new set of parameterizations of the hydrologic exchanges at the land-atmosphere interface within the LMD atmospheric general circulation model. *Journal of Climate*, *6*, 248-273.

Dudhia, J. (1989). Numerical study of convection observed during the winter monsoon experiment using a mesoscale two-dimensional model. *Journal of Atmospheric Sciences*, *46*, 3077-3107.

Dudhia, J. (2005). *The weather research and forecast model version 2.0: Physics update.* Communication donnée au MM5/WRF User's Workshop. USA, Colorado: National Center for Atmospheric Research.

Dufresne, J. L., M. A. Foujols, S. Denvil, A. Caubel, O. Marti, O. Aumont, Y. Balkanski, S. Bekki, H. Bellenger, R. Benshila, S. Bony, L. Bopp, P. Braconnot, P. Brockmann, P. Cadule, F. Cheruy, F. Codron, A. Cozic, D. Cugnet, N. de Noblet, J.-P. Duvel, C. Ethé, L. Fairhead, T. Fichefet, S. Flavoni, P. Friedlingstein, J.-Y. Grandpeix, L. Guez, E. Guilyardi, D. Hauglustaine, F. Hourdin, A. Idelkadi, J. Ghattas, S. Joussaume, M. Kageyama, G. Krinner, S. Labetoulle, A. Lahellec, M.-P. Lefebvre, F. Lefevre, C. Levy, Z. X. Li, J. Lloyd, F. Lott, G. Madec, M. Mancip, M. Marchand, S. Masson, Y. Meurdesoif, J. Mignot, I. Musat, S. Parouty, J. Polcher, C. Rio, M. Schulz, D. Swingedouw, S. Szopa, C. Talandier, P. Terray, N. Viovy, and N. Vuichardan (2012). Climate change projections using the IPSL-CM5 Earth System Model: from CMIP3 to CMIP5. *Climate Dynamics*, *40*, 2123-2165.

Dunne, J. P., J. G. John, E. Shevliakova, R. J. Stouffer, J. P. Krasting, S. L. Malyshev, P. C. D. Milly, L. T. Sentman, A. J. Adcroft, W. Cooke, K. A. Dunne, S. M. Griffies, R. W. Hallberg, M. J. Harrison, H. Levy, A. T. Wittenberg, P. J. Phillips, and N. Zadeh (2013). GFDL's ESM2 Global Coupled Climate-Carbon Earth System Models. Part II: Carbon System Formulation and Baseline Simulation Characteristics. *Journal of Climate*, *26*(7), 2247-2267.

Durran, D. R. (2010). Physically Insignificant Fast Waves. *Numerical Methods for Fluid Dynamics*, 393-451.

Eckman, R. M. (1998). Observations and numerical simulations of winds within a broad forested valley. *Journal of Applied Meteorology*, *37*(2), 206-219.

Ek, M. B., K. E. Mitchell, Y. Lin, E. Rogers, P. Grunmann, V. Koren, G. Gayno, and J. D. Tarpley (2003). Implementation of Noah land surface model advances in the National Centers for Environmental Prediction operational mesoscale Eta model. *Journal of Geophysical Research, 108*(D22), 8851.

Ekman, V. W. (1905). On the influence of the earth's rotation on ocean currents. *Arkiv för matematik, astronomi och fysik, 11*(2), 52 pp.

Emanuel, K. A. (1991). A scheme for representing cumulus convection in large-scale models, *Journal of Atmospheric Sciences, 48*(21), 2313-2335.

Errico, R. M. (1985). Spectra computed from a limited area grid. *Monthly Weather Review, 113*, 1554-1562.

Essery, R. L. H., M. J. Best, R. A. Betts, P. M. Cox, and C. M. Taylor (2003). Explicit representation of subgrid heterogeneity in a GCM land-surface scheme. *Journal of Hydrometeorology, 4*, 530-543.

Farda, A., M. Déué, S. Somot, A. Horányi, V. Spiridonov, and H. Tóth (2010). Model ALADIN as regional climate model for Central and Eastern Europe. *Studia Geophysica et Geodaetica, 54*(2), 313-332.

Flato, G. M., G. J. Boer, W. G. Lee, N. A. McFarlane, D. Ramsden, M. C. Reader, and A. J. Weaver (2000). The Canadian Centre for Climate Modelling and Analysis Global Coupled Model and its Climate. *Climate Dynamics, 16*, 451-467.

Flato, G. M., and G .J. Boer (2001). Warming Asymmetry in Climate Change Simulations. *Geophysical Research Letters, 28*, 195-198.

Fogli, P. G., E. Manzini, M. Vichi, A. Alessandri, L. Patara, S. Gualdi, E. Scoccimarro, S. Masina, and A. Navarra (2009). *INGV-CMCC Carbon: a carbon cycle earth system model.* (Volume 61, 31 pp.). Italy: Centro Euro-Mediterraneo per | Cambiamenti Climatici (CMCC) Research.

Fu, C., S. Wang, Z. Xiong, W. J. Gutowski, D. K. Lee, J. L. McGregor, Y. Sato, H. Kato, J.-W. Kim, and M. S. Suh (2005). Regional climate model intercomparison project for Asia. *Bulletin of the American Meteorological Society, 86*(2), 257-266.

Furevik, T., M. Bentsen, H. Drange, I. K. T. Kindem, N. G. Kvamstø, and A. Sorteberg (2003). Description and evaluation of the Bergen climate model: ARPEGE coupled with MICOM. *Climate Dynamics, 21*(1), 27-51.

Gage, K. S. (1979). Evidence for a $k^{-5/3}$ law inertial range in mesoscale two-dimensional turbulence. *Journal of Atmospheric Sciences*, *36*, 1950-1954.

Gage, K. S., and G. D. Nastrom (1986). Theoretical interpretation of atmospheric wavenumber spectra of wind and temperature observed by commercial aircraft during GASP. *Journal of Atmospheric Sciences*, *43*(7), 729-740.

Gent, P. R., G. Danabasoglu, L. J. Donner, M. M. Holland, E. C. Hunke, S. R. Jayne, D. M. Lawrence, R. B. Neale, P. J. Rasch, M. Vertenstein, P. H. Worley, Z.-L. Yang, and M. Zhang (2011). The community climate system model version 4. *Journal of Climate*, *24*(19), 4973-4991.

Gérard, L. (2007). An integrated package for subgrid convection, clouds and precipitation compatible with meso-gamma scales. *Quarterly Journal of the Royal Meteorological Society*, *133*, 711-730.

Gérard, L., J.-M. Piriou, R. Brožková, J.-F. Geleyn, and D. Banciu (2009). Cloud and precipitation parameterization in a meso-gamma-scale operational weather prediction model. *Monthly Weather Review*, *137*, 3960-3977.

Giorgetta, M. A., J. H. Jungclaus, C. H. Reick, S. Legutke, V. Brovkin, T. Crueger, M. Esch, K. Fieg, K. Glushak, V. Gayler, H. Haak, H.-D. Hollweg, T. Ilyina, S. Kinne, L. Kornblueh, D. Matei, T. Mauritsen, U. Mikolajewicz, W. Mueller, D. Notz, T. Raddatz, S. Rast, R. Redler, E. Roeckner, H. Schmidt, R. Schnur, J. Segschneider, K. Six, M. Stockhause, J. Wegner, H. Widman, K.-H. Wieners, M. Claussen, J. Marotzke, and B. Stevens (2012). Climate change from 1850 to 2100 in MPI-ESM simulations for the Coupled Model Intercomparison Project 5. The Max Planck Institute for Meteorology Earth System Model. *Submitted to Journal of Advances in Modeling Earth Systems, special issue.*

Giorgi, F., and G. T. Bates (1989). The climatological skill of a regional model over complex terrain. *Monthly Weather Review*, *117*(11), 2325-2347.

Giorgi, F. (1990). Simulation of regional climate using a limited area model nested in a general circulation model. *Journal of Climate*, *3*(9), 941-963.

Giorgi, F., and E. Coppola (2010). Does the model regional bias affect the projected regional climate change? An analysis of global model projections. *Climatic Change*, *100*(3), 787-795.

Gordon, H. B., and S. P. O'Farrell (1997). Transient climate change in the CSIRO coupled model with dynamic sea ice. *Monthly Weather Review*, *125*, 875-907.

Gordon, H. B., L. D. Rotstayn, J. L. McGregor, M. R. Dix, E. A. Kowalczyk, S. P. O'Farrell, L. J. Waterman, A. C. Hirst, S. G. Wilson, M. A. Collier, I. G. Watterson, and T. I. Elliott (2002a). *The CSIRO Mk3 Climate System Model.* (TP 60). Commonwealth Scientific and Industrial Research Organisation (CSIRO) Atmospheric Research. Available at: http://www.cmar.csiro.au/e-print/open/gordon 2002a.pdf

Gordon, H., S. P. O'Farrell, M. Collier, M. Dix, L. Rotstayn, E. Kowalczyk, T. Hirst, and I. Watterson (2010). *The CSIRO Mk3. 5 climate model.* (TR No. 021) Centre for Australian Weather and Climate Research (CAWCR).

Grasso, L. D. (2000). The differentiation between grid spacing and resolution and their application to numerical modeling. *Bulletin of the American Meteorological Society*, *81*(3), 579-580.

Gregory, D., and P. R. Rowntree (1990). A mass flux convection scheme with representation of cloud ensemble characteristics and stability dependent closure. *Monthly Weather Review*, *118*, 1483-1506.

Gregory, D., J. J. Morcrette, C. Jakob, A. C. M. Beljaars, and T. Stockdale (2000). Revision of convection, radiation and cloud schemes in the ECMWF Integrated Forecasting System. *Quarterly Journal of the Royal Meteorological Society*, *126*(566), 1685-1710.

Grell, G. A. (1993). Prognostic evaluation of assumptions used by cumulus parameterizations. *Monthly Weather Review, 121*, 764-787.

Grell, G. A., J. Dudhia, and D.R. Stauffer (1994). *A Description of the Fifth-Generation Penn State/NCAR Mesoscale Model (MM5).* (NCAR-TN-398+STR). USA: National Center for Atmospheric Research.

Grell, G. A., and D. Dévényi (2002). A generalized approach to parameterizing convection combining ensemble and data assimilation techniques. *Geophysical Research Letters*, *29*(14-38), 1-4.

Griffies, S. M., M. Winton, L. J. Donner, L. W. Horowitz, S. M. Downes, R. Farneti, A. Gnanadesikan, W. J. Hurlin, H.-C. Lee, Z. Liang, J. B. Palterm B. L. Samuels, A. T. Wittenberg, B. K. Wyman, J. Yin, and N. Zadeh (2011). The GFDL CM3 coupled climate model: Characteristics of the ocean and sea ice simulations. *Journal of Climate*, *24*(13), 3520-3544.

Grotch, S. L. (1988). *Regional intercomparisons of general circulation model predictions and historical climate data.* (Report DOE/NBB-0084). USA, Springfield: National Technical Information Service, U.S. Department of Commerce, VA 22161.

Hack, J. J., B. A. Boville, B. P. Briegleb, J. T. Kiehl, P. J. Rasch, and D. L. Williamson (1993). *Description of the NCAR Community Climate Model (CCM2).* (NCAR/TN-382-STR, 108 pp). USA: National Center for Atmospheric Research.

Haiden, T., A. Kann, C. Wittmann, G. Pistotnik, B. Bica, and C. Gruber (2011). The Integrated Nowcasting through Comprehensive Analysis (INCA) system and its validation over the Eastern Alpine region. *Weather and Forecasting, 26*(2), 166-183.

Harshvardhan, R. Davies, D. A. Randall, T. G. and Corsetti (1987). A fast radiation parameterization for atmospheric circulations models. *Journal of Geophysical Research, 92*, 1009-1016.

Hart, K. A., W. J. Steenburgh, and D. J. Onton (2005). Model forecast improvements with decreased horizontal grid spacing over finescale intermountain orography during the 2002 Olympic Winter Games. *Weather and Forecasting, 20*(4), 558-576.

Hernández-Díaz, L., R. Laprise, L. Sushama, A. Martynov, K. Winger, and B. Dugas (2013). Climate simulation over CORDEX Africa domain using the fifth-generation Canadian Regional Climate Model (CRCM5). *Climate Dynamics, 40*(5-6), 1415-1433.

Hewitt, C. D. (2005). The ENSEMBLES Project: Providing ensemble-based predictions of climate changes and their impacts. *European Geophysical Society (EGGS) Newsletter, 13*, 22-25.

Hewitt, H. T., D. Copsey, I. D. Culverwell, C. M. Harris, R. S. R. Hill, A. B. Keen, and E. C. Hunke (2011). Design and implementation of the infrastructure of HadGEM3: the next-generation Met Office climate modelling system. *Geoscientific Model Development, 4*(2), 223-253.

Hill, C., C. DeLuca, M. S. Balaji, and A. da Silva (2004). The architecture of the earth system modeling framework. *Journal of Computing Science Engineering, 6*, 18-28.

Hill, G. E. (1968). Grid telescoping in numerical weather prediction. *Journal of Applied Meteorology, 7*(1), 29-38.

Holtslag, A. A. M., and B. A. Boville (1993). Local versus nonlocal boundary-layer diffusion in a global climate model. *Journal of Climate*, *6*, 1825-1842.

Hong, S.-Y., and H.-L. Pan (1996). Nonlocal boundary layer vertical diffusion in a medium-range forecast model. *Monthly Weather Review, 124*, 2322-2339.

Hong, S.-Y., J. Dudhia, and S.H. Chen (2004). A revised approach to ice microphysical processes for the bulk parameterization of clouds and precipitation. *Monthly Weather Review*, *132*(1), 103-120.

Hong, S.-Y., and J. O. J. Lim (2006). The WRF single-moment 6-class microphysics scheme (WSM6). *Journal of Korean Meteorology Society*, *42*(2), 129-151.

Hong, S.-Y., Y. Noh, and J. Dudhia (2006). A new vertical diffusion package with an explicit treatment of entrainment processes. *Monthly Weather Review*, *134*(9), 2318-2341.

Hourdin, F., I. Musat, S. Bony, P. Braconnot, F. Codron, J.-L. Dufresne, L. Fairhead, M.-A. Filiberti, P. Friedlingstein, J.-Y. Grandpeix, G. Krinner, P. LeVan, Z.-X. Li, and F. Lott (2006). The LMDZ4 general circulation model: climate performance and sensitivity to parametrized physics with emphasis on tropical convection. *Climate Dynamics*, *27*(7-8), 787-813.

Hsie, E.-Y., R. A. Anthes, and D. Keyser (1984). Numerical simulation of frontogenesis in a moist atmosphere. *Journal of Atmospheric Sciences*, *41*, 2581-2594.

IPCC-Intergovernmental Panel on Climate Change. 2013. *IPCC*. En ligne. <http://www.ipcc.ch/>. Consulté le 20 avril 2013.

Jacob, D., and R. Podzun (1997). Sensitivity studies with the regional climate model REMO. *Meteorology and Atmospheric Physics*, *63*(1-2), 119-129.

Jiao, Y., and D. Caya (2006). An investigation of summer precipitation simulated by the Canadian Regional Climate Model. *Monthly Weather Review*, *134*, 919-932.

Johns, T. C., R. E. Carnell, J. F. Crossley, J. M. Gregory, J. F. Mitchell, C. A. Senior, S. F. B. Tett, and R. A. Wood (1997). The second Hadley Centre coupled ocean-atmosphere GCM: model description, spinup and validation. *Climate Dynamics*, *13*(2), 103-134.

Johns, T. C., C. F. Durman, H. T. Banks, M. J. Roberts, A. J. McLaren, J. K. Ridley, C. A. Senior, K. D. Williams, A. Jones, G. J. Rickard, S. Cusack, W. J. Ingram, M. Crucifix, D. M. H. Sexton, M. M. Joshi, B.-W. Dong, H. Spencer, R. S. R. Hill, J. M. Gregory, A. Keen, A. K. Pardaens, J. A. Lowe, A. Bodas-Salcedo, S. Stark, and Y. Searl (2006). The new Hadley Centre climate model (HadGEM1): Evaluation of coupled simulations. *Journal of Climate*, *19*(7), 1327-1353.

Jones, C., F. Giorgi, and G. Asrar (2011). The Coordinated Regional Downscaling Experiment: CORDEX an international downscaling link to CMIP5. *Clivar Exchanges*, *16*, 34-39.

Jones, R. G., J. M. Murphy, and M. Noguer (1995). Simulation of climate change over Europe using a nested regional-climate model. I: Assessment of control climate, including sensitivity to location of lateral boundaries. *Quarterly Journal of the Royal Meteorological Society*, *121*(526), 1413-1449.

Kain, J. S., and J. M. Fritsch (1990). A one-dimensional entraining/detraining plume model and application in convective parameterization. *Journal of Atmospheric Sciences*, *47*, 2784-2802.

Kain, J. S. (2004). The Kain-Fritsch convective parameterization: an update. *Journal of Applied Meteorology*, *43*(1), 170-181.

Kalnay, E., M. Kanamitsu, R. Kistler, W. Collins, D. Deaven, L. Gandin, M. Iredell, S. Saha, G. White, J. Woollen, Y. Zhu, A. Leetmaa, R. Reynolds, M. Chelliah, W. Ebisuzaki, W. Higgins, J. Janowiak, K. C. Mo, C. Ropelewski, J. Wang, R. Jenne, and D. Joseph (1996). The NCEP/NCAR 40-year reanalysis project. *Bulletin of the American Meteorological Society*, *77*(3), 437-471.

Kessler, E. (1969). On the distribution and continuity of water substance in atmospheric circulation models. *Meteorological Monography*, *10*(32), 88 pp.

Khodri, M., Y. Leclainche, G. Ramstein, P. Braconnot, O. Marti, and E. Cortijo (2001). Simulating the amplification of orbital forcing by ocean feedbacks in the last glaciation. *Nature*, *410*(6828), 570-574.

Kiehl, J. T., and P. R. Gent (2004). The community climate system model, version 2. *Journal of Climate*, *17*(19), 3666-3682.

Kolmogorov, A. N. (1941). The local structure of turbulence in incompressible viscous fluid for very large Reynolds numbers. *Czech Republic Academy of Sciences URSS*, *30*, 301-305.

Koshyk, J. N., and K. Hamilton (2001). The horizontal kinetical energy spectrum and spectral budget simulated by high-resolution troposphere-stratosphere-mesosphere GCM. *Journal of Atmospheric Sciences*, *58*, 329-348.

Kossmann, M., and A. P. Sturman (2003). Pressure-driven channeling effects in bent valleys. *Journal of Applied Meteorology*, *42*, 151-158.

Kraichnan, R. H. (1967). Inertial ranges in two-dimensional turbulence. *Physique Fluids*, *10*, 1417-1423.

Kuo, H. L. (1965). On formation and intensification of tropical cyclones through latent heat release by cumulus convection. *Journal of Atmospheric Sciences*, *22*, 40-63.

Laflamme, J. N., and G. Périard (1998). The climate of freezing rain over the province of Quebec in Canada: A preliminary analysis. *Atmospheric Research*, *46*(1), 99-111.

Laprise, R. (1992). The Euler equation of motion with hydrostatic pressure as independent coordinate. *Monthly Weather Review*, *120*, 197-207.

Laprise, R., D. Caya, G. Bergeron, and M. Giguère (1997). The formulation of André Robert MC2 (Mesoscale Compressible Community) model. *Atmosphere-Ocean*, *35*(1), 195-220.

Laprise, R., R. de Elia, D. Caya, S. Biner, P. Lucas-Picher, E. Diaconescu, M. Leduc, A. Alexandru, and L. Separovic (2008). Challenging some tenets of regional climate modelling. *Meteorology and Atmospheric Physics*, *10*(1-4), 3-22.

Lean, H. W., P. A. Clark, M. Dixon, N. M. Roberts, A. Fitch, R. Forbes, and C. Halliwell (2008). Characteristics of high-resolution versions of the Met Office Unified Model for forecasting convection over the United Kingdom. *Monthly Weather Review*, *136*(9), 3408-3424.

Leduc, M., and R. Laprise (2009). Regional climate model sensitivity to domain size. *Climate Dynamics*, *32*(6), 833-854.

Lenderink, G., B. J. J. M. van den Hurk, E. van Meijgaard, A. van Ulden, and H. Cuijpers (2003). *Simulation of present-day climate in RACMO2: first results and model developments.* Koninklijk Nederlands Meteorologisch Instituut. [Available online at: http://www.weeralarm.nl/publications/fulltexts/trracmo2.pdf]

Lenderink, G., A. P. Siebesma, S. Cheinet, S. Irons, C. G. Jones, P. Marquet, F. Müller, D. Olmeda, J. Calvo, E. Sanchez, and P. M. M. Soares (2005). The diurnal cycle of shallow cumulus clouds over land: a single column model intercomparison study. *Quarterly Journal of Royal Meteorology Society, 123*, 223-242.

Li, J., and H. W. Barker (2005). A radiation algorithm with correlated-k distribution. Part-I: local thermal equilibrium. *Journal of Atmospheric Sciences, 62*, 286-309.

Li, Z. X., and S. Conil (2003). Transient response of an atmospheric GCM to North Atlantic SST anomalies. *Journal of Climate, 16*(23), 3993-3998.

Liang, X. Z., L. Li, K. E. Kunkel, M. Ting, and J. X. Wang (2004). Regional climate model simulation of US precipitation during 1982-2002. Part I: Annual cycle. *Journal of Climate, 17*(18), 3510-3529.

Liang, X. Z., M. Xu, H. I. Choi, K. E. Kunkel, L. Rontu, J. F. Geleyn, M. D. Müller, E. Joseph, and J. X. L. Wang (2006). *Development of the regional Climate Weather Research and Forecasting model (CWRF): Treatment of subgrid topography effects.* Communication in Proceedings of the 7th Annual WRF User's Workshop, Boulder, CO, 19-22.

Lilly, D. K., and E. Peterson (1983). Stratified turbulence and the mesoscale variability of the atmosphere. *Journal of Atmospheric Sciences, 40*, 744-761.

Lilly, D. K., G. Bassett, K. Droegemeier, and P. Bartello (1998). Stratified turbulence in the atmospheric mesoscales. *Theoretical and Computational Fluid Dynamics, 11*, 139-153.

Lindzen, R. S., and M. Fox-Rabinowitz (1989). Consistent vertical and horizontal resolution. *Monthly Weather Review, 117*, 2575-2583.

Lohmann, U., and E. Roeckner (1996). Design and performance of a new cloud microphysics scheme developed for the ECHAM general circulation model. *Climate Dynamics, 12*, 557-572.

Lunkeit, F., R. Sausen, and J. M. Oberhuber (1996). Climate simulations with the global coupled atmosphere-ocean model ECHAM2/OPYC Part I: present-day climate and ENSO events. *Climate Dynamics, 12*(3), 195-212.

Mailhot, J., J. A. Milbrandt, A. Giguère, R. McTaggart-Cowan, A. Erfani, B. Denis, A. Glazer, and M. Vallée (2012). An experimental high resolution forecast system during the Vancouver 2010 winter Olympic and Paralympic games. *Pure Applied Geophysics*, 1-21.

Manabe, S., J. Smagorinsky, and R. F. Strickler (1965). Simulated climatology of a general circulation model with a hydrologic cycle 1. *Monthly Weather Review, 93*(12), 769-798.

Manabe, S., and K. Bryan (1969). Climate calculations with a combined ocean-atmosphere model. *Journal of Atmospheric Sciences, 26*(4), 786-789.

Manabe, S., and R. T. Wetherald (1975). The effects of doubling the CO_2 concentration on the climate of a General Circulation Model. *Journal of Atmospheric Sciences, 32*, 3-15.

Marengo, J. A., and T. Ambrizzi (2006). Use of regional climate models in impacts assessments and adaptations studies from continental to regional and local scales. *Proceedings of, 8*, 24-28.

Mass, C., D. Ovens, K. Westrick, and B. A. Colle (2002). Does increasing horizontal resolution produce more skilful forecasts? The results of two years of real-time nnumerical weather prediction over the Pacific northwest. *Bulletin of the American Meteorological Society, 83*, 407-430.

McFarlane, N. A. (1987). The effect of orographically excited gravity-wave drag on the circulation of the lower stratosphere and troposphere. *Journal of Atmospheric Sciences, 44*, 1175-1800.

McFarlane, N. A., J. F. Scinocca, M. Lazare, R. Harvey, D. Verseghy, and J. Li (2005). *The CCCma third generation atmospheric general circulation model.* Canadian Centre for Climate Modelling and Analysis (CCCma) Internal Report, 25 pp.

Mearns, L. O., S. H. Schneider, S. L. Thompson, and L. R. McDaniel (1990). Analysis of climate variability in General Circulation Models: comparison with observations and changes in variability in 2xCO2 experiments. *Journal of Geophysical Research, 95*(12), 469-520.

Mearns, L. O., W. J. Gutowski, R. Jones, L.-Y. Leung, S. McGinnis, A. M. B. Nunes, and Y. Qian (2009). A regional climate change assessment program for North America. *Eos, Transactions American Geophysical Union, 90*(36), 311-312.

Meehl, G., W. Washington, J. Arblaster, A. Hu, H. Teng, J. Kay, A. Gettelman, D. Lawrence, B. Sanderson, and W. Strand (2013). Climate change projections in CESM1 (CAM5) compared to CCSM4. *Journal of Climate*, DOI: 10.1175/JCLI-D-12-00572.1, in press.

Mellor, G. L., and T. Yamada (1982). Development of a turbulence closure model for geophysical fluid problems. *Review Geophysics and Space Physics*, *20*, 851-875.

Milbrandt, J. A., and M. K. Yau (2005). A multimoment bulk microphysics parameterization. Part I: Analysis of the role of the spectral shape parameter. *Journal of the Atmospheric Sciences*, *62*(9), 3051-3064.

Milbrandt, J. A., and M. K. Yau (2005). A multimoment bulk microphysics parameterization. Part II: A proposed three-moment closure and scheme description. *Journal of the Atmospheric Sciences*, *62*(9), 3065-3081.

Mlawer, E. J., S. J. Taubman, P. D. Brown, M. J. Iacono, and S. A. Clough (1997). Radiative transfer for inhomogeneous atmospheres: RRTM, a validated correlated-k model for the longwave. *Journal of Geophysical Research*, *102*(D14), 663-716.

Molinari, J., and M. Dudek (1992). Parameterization of convective precipitation in mesoscale numerical models: A critical review. *Monthly Weather Review*, *120*(2), 326-344.

Morcrette, J.-J. (1989). *Description of the Radiation Scheme in the ECMWF Model.* Technical Memorandum 165, European Center for Medium-Range Weather Forecasts (ECMWF), 26 pp.

Murphy, J. M. (1995). Transient response of the Hadley Centre coupled ocean-atmosphere model to increasing carbon dioxide. Part I: Control climate and flux adjustment. *Journal of Climate*, *8*(1).

Music, B., and D. Caya (2007). Evaluation of the Hydrological Cycle over the Mississippi River Basin as Simulated by the Canadian Regional Climate Model (CRCM). *Journal of Hydrometeorology*, *8*(5), 969-988.

Nastrom, G. O., and K. S. Gage (1985). A climatology of atmospheric wavenumber spectra of wind and temperature observed by commercial aircraft. *Journal of Atmospheric Sciences*, *42*(9), 950-960.

« National Aeronautics and Space Administration (NASA) ». 2010 (14 Octobre). In *Earth Observatory Vilhelm Bjerknes (1862-1951).* En ligne. <http://earthobservatory.nasa.gov/Features/Bjerknes/bjerknes_2.php>. Consulté le 2 mai 2013.

Nawri, N., and R. E. Stewart (2006). Climatological features of orographic low-level jets over Frobisher Bay. *Atmosphere-Ocean*, *44*, 397-413.

Noilhan, J., and S. Planton (1989). A simple parameterization of land surface processes for meteorological models. *Monthly Weather Review*, *117*, 536-549.

Nozawa, T., T. Nagashima, T. Ogura, T. Yokohata, N. Okada, and H. Shiogama (2007). Climate change simulations with a coupled ocean- atmosphere GCM called the model for interdisciplinary research on climate: MIROC. *Centre for Global Environmental Research, National Institute for Environmental Studies, Tsukuba, Report 12.*

Otterâ, O. H., M. Bentsen, I. Bethke, and N. G. Kvamstø (2009). Simulated pre-industrial climate in Bergen Climate Model (version 2): model description and large-scale circulation features. *Geoscientific Model Development*, *2*, 197-212.

Pal, J. S., E. E. Small, and E. A. B. Eltahir (2000). Simulation of regional-scale water and energy budgets: Representation of subgrid cloud and precipitation processes within RegCM. *Journal of Geophysical Research-Atmospheres*, *105*(D24), 579-594.

Pal, J. S., F. Giorgi, X. Bi, N. Elguindi, F. Solmon, S. A. Rauscher, R. Francisco, A. Zakey, J. Winter, M. Ashfaq, F. S. Syed, J. L. Bell, N. S. Diffenbaugh, J. Karmacharya, A. Konaré, D. Martinez, R. P. da Rocha, L. C. Sloan, and A. L. Steiner (2007). Regional climate modeling for the developing world: The ICTP RegCM3 and RegCNET. *Bulletin of the American Meteorological Society*, *88*(9), 1395-1409.

Parry, M. L., O. F. Canziani, J. P. Palutikof, P. J. van der Linden, and C. E. Hanson (2007). *IPCC: Climate Change 2007 Impacts, Adaptation and Vulnerability. Contribution of Working Group II to the Fourth Assessment Report of the Intergovernmental Panel on Climate Change*. Cambridge University Press, Cambridge, Ukraine, 976 pp.

Petch, J. C., A. R. Brown, and M. E. B. Gray (2002). The impact of horizontal resolution on the simulations of convective development over land. *Quarterly Journal of the Royal Meteorological Society*, *128*(584), 2031-2044.

Pielke, R. A. (1991). A recommended specific definition of "resolution". *Bulletin of American Meteorology Society*, *72*(12), 1914.

Piriou, J. M., J. L. Redelsperger, J. F. Geleyn, J. P. Lafore, and F. Guichard (2007). An approach for convective parameterization with memory: separating microphysics and transport in grid-scale equations. *Journal of the Atmospheric Sciences*, *64*(11), 4127-4139.

Pope, V. D., M. L. Gallani, P. R. Rowntree, and R. A. Stratton (2000). The impact of new physical parametrizations in the Hadley Centre climate model: HadAM3. *Climate Dynamics*, *16*(2-3), 123-146.

Prein, A., H. Truhetz, M. Suklistch, and A. Gobiet (2011). *Evaluation of the Local Climate Model Intercomparison Project (LocMIP) simulations.* (Report 41). Austria: WegCenter Verlag, Graz, ISBN 978-3-9502940-8-8.

Puckrin, E., W. F. J. Evans, J. Li, and H. Lavoie (2004). Comparison of clear-sky surface radiative fluxes simulated with radiative transfer models. *Canadian Journal of Remote Sensing*, *30*, 903-912.

Qiao, F., and X. Z. Liang (2012). An ensemble cumulus parameterization: Optimization for mesoscale modeling over land and ocean. *Journal of Climate*, in preparation.

Rasch, P. J., and J. E. Kristjánsson (1998). Comparison of the CCM3 model climate using diagnosed and predicted condensate parameterizations. *Journal of Climate, 11*, 1587-1614.

Reisner, J., R. M. Rasmussen, and R. T. Bruintjes (1998). Explicit forecasting of supercooled liquid water in winter storms using the MM5 mesoscale model. *Quarterly Journal of the Royal Meteorological Society*, *124*(548), 1071-1107.

Ricard, J.-L., and J.-F. Royer (1993). A statistical cloud scheme for use in an AGCM. *Annual Geophysics – Atmosphere Hydrosphere Space Sciences*, *11*, 1095-1115.

Rife, D. L., C. A. Davis, and J. C. Knievel (2009). Temporal changes in wind as objects for evaluating mesoscale numerical weather prediction. *Weather and Forecasting*, *24*(5), 1374-1389.

Ritter, B., and J. F. Geleyn (1992). A comprehensive radiation scheme for numerical weather prediction models with potential applications in climate simulations. *Monthly Weather Review, 120*, 303-325.

Robert, A. (1981). A stable numerical integration scheme for the primitive meteorological equations. *Atmosphere-Ocean*, *19*(1), 35-46.

Roebber, P. J., and J. R. Gyakum (2003). Orographic influences on the mesoscale structure of the 1998 ice storm. *Monthly Weather Review*, *131*, 27-50.

Roeckner, E., K. Arpe, L. Bengtsson, S. Brinkop, L. Dümenil, M. Esch, E. Kirk, F. Lunkeit, S. Schubert, M. Windelband, U. Schlese, S. Brinkop, M. Ponater, and R. Sausen (1992). *Simulation of the present-day climate with the ECHAM model: Impact of model physics and resolution.* Hamburg, Germany: Max-Planck-Institut für Meteorologie, 171 pp.

Roeckner, E. (1996). *The atmospheric general circulation model ECHAM-4: Model description and simulation of present-day climate.* (Report No. 218). Hamburg, Germany: Max-Planck-Institut fürr Meteorologie.

Roeckner, E. (2003). *The atmospheric general circulation model ECHAM5: Part 1: model description.* (Report No. 349). Hamburg, Germany: Max-Planck-Institut für Meteorologie.

Rosenzweig, C., and F. Abramopoulos (1997). Land-surface model development for the GISS GCM. *Journal of Climate*, *10*(8), 2040-2054.

Russell, G. L., J. R. Miller, and D. Rind (1995). A Coupled Atmosphere-Ocean Model for Transient Climate Change Studies. *Atmosphere-Ocean*, *33*(4), 683-730.

Russell, J. L., R. J. Stouffer, and K. W. Dixon (2005). Intercomparison of the Southern Ocean Circulations in IPCC Coupled Model Control Simulations. *Journal of Climate*, *19*, 4560-4575.

Saha, S., S. Nadiga, C. Thiaw, J. Wang, W. Wang, Q. Zhang, Q., H. M. Van den Dool, H.-L. Pan, S. Moorthi, D. Behringer, D. Stokes, M. Peña, S. Lord, G. White, W. Ebisuzaki, P. Peng, and P. Xie (2006). The NCEP climate forecast system. *Journal of Climate*, *19*(15), 3483-3517.

Saha, S., S. Moorthi, X. Wu, J. Wang, S. Nadiga, P. Tripp, D. Behringer, Y.-T. Hou, H.-ya Chuang, M. Iredell, M. Ek, J. Meng, R. Yang, M. P. Mendez, H. Van den Dool, Q. Zhang, W. Wang, M. Chen, and E. Becker (2013). The NCEP climate forecast system version 2. *Journal of Climate*, submitted.

Sakamoto, T. T., Y. Komuro, M. Ishii, H. Tatebe, H. Shiogama, A. Hasegawa, T. Toyoda , M. Mori, T. Suzuki, Y. Imada-Kanamaru, T. Nozawa, K. Takata, T. Mochizuki, K. Ogochi, T. Nishimura, S. Emori, H. Hasumi, and M. Kimoto (2012). MIROC4h a new high-resolution atmosphere-ocean coupled general circulation model. *Journal of Meteorological Society Japan*, in press.

Salas-Mélia, D., F. Chauvin, M. Déqué, H. Douville, J. F. Gueremy, P. Marquet, S. Planton, J. F. Royer, and S. Tyteca (2005). Description and validation of the CNRM-CM3 global coupled model. *Climate Dynamics,* in review.

Salvador, R., J. Calbó, and M. M. Millán (1999). Horizontal grid size selection and its influence on mesoscale model simulations. *Journal of Applied Meteorology, 38*, 1311-1329.

Savijaïrvi, H. (1990). A fast radiation scheme for mesoscale model and short-range forecast models. *Journal of Applied Meteorology, 29*, 437-447.

Schmidt, G. A., R. Ruedy, J. E. Hansen, I. Aleinov, N. Bell, M. Bauer, S. Bauer, B. Cairns, V. Canuto, Y. Cheng, A. Del Genio, G. Faluvegi, A. D. Friend, T. M. Hall, Y. Hu, M. Kelley, N. Y. Kiang, D. Koch, A. A. Lacis, J. Lerner, K. K. Lo, R. L. Miller, L. Nazarenko, V. Oinas, Ja. Perlwitz, Ju. Perlwitz, D. Rind, A. Romanou, G. L. Russell, M. Sato, D. T. Shindell, P. H. Stone, S. Sun, N. Tausnev, D. Thresher, and M.-S. Yao (2006). Present day atmospheric simulations using GISS ModelE: Comparison to in-situ, satellite and reanalysis data. *Journal of Climate, 19*, 153-192.

Scinocca, J. F., N. A. McFarlane, M. Lazare, J. Li, and D. Plummer (2008). The CCCma third generation AGCM and its extension into the middle atmosphere. *Atmospheric Chemistry and Physics, 8*, 7055-7074.

Scoccimarro, E., S. Gualdi, A. Bellucci, A. Sanna, P. G. Fogli, E. Manzini, M. Vichi, P. Oddo, and A. Navarra (2011). Effects of Tropical Cyclones on Ocean Heat Transport in a High Resolution Coupled General Circulation Model. *Journal of Climate, 24*, 4368-4384.

Seifert, A., and K. D. Beheng (2001). A double moment parameterization for simulating autoconversion and selfcollection. *Atmospheric Research, 59*(60), 265-281.

Sellers, P. J., R. E. Dickinson, D. A. Randall, A. K. Betts, F. G. Hall, J. A. Berry, G. J. Collatz, A. S. Denning, H. A. Mooney, C. A. Nobre, N. Sato, C. B. Field, and A. Henderson-Sellers (1997). Modeling the exchanges of energy, water, and carbon between continents and the atmosphere. *Science, 275*, 502-509.

Simmons, A., S. Uppala, D. Dee, and S. Kobayashi (2007). ERA-Interim: New ECMWF reanalysis products from 1989 onwards. *European Center for Medium-Range Weather Forecasts Newsletter, 110*(110), 25-35.

Skamarock, W. C. (2004). Evaluating mesoscale NWP models using kinetic energy spectra. *Monthly Weather Review, 132*, 3019-3032.

Skamarock, W. C., J. B. Klemp, J. Dudhia, D. O. Gill, D. M. Barker, W. Wang, and J. G. Powers (2005). *A description of the advanced research WRF version 2.* (NCAR/TN-468+STR). USA: National Center for Atmospheric Research.

Skamarock, W. C., and J. B. Klemp (2008). A time-split nonhydrostatic atmospheric model for weather research and forecasting applications. *Journal of Computational Physics*, *227*(7), 3465-3485.

Smith, R. N. B. (1990). A scheme for predicting layer clouds and their water content in a general circulation model. *Quarterly Journal of Royal Meteorology Society*, *116*, 435-460.

Smith, R. N. B. (1993). *Experience and developments with the layer cloud and boundary layer mixing schemes in the UK Meteorological Office United Model.* Communication in the ECMWF/GCSS workshop on parametrization of the cloud-topped boundary layer, ECMWF, Reading, England.

Stephens, G. L. (1978). Radiation profiles in extended water clouds. II: Parameterizaton schemes. *Journal of Atmospheric Sciences*, *35*, 2123-2132.

Stevens, B., M. Giorgetta, M. Esch, T. Mauritsen, T. Crueger, S. Rast, M. Salzmann, H. Schmidt, J. Bader, K. Block, R. Brokopf, I. Fast, S. Kinne, L. Kornblueh, U. Lohmann, R. Pincus, T. Reichler, and E. Roeckner (2013). Atmospheric component of the MPI-M earth system model: ECHAM6. *Journal of Advances in Modeling Earth Systems*, *5*, 1-27.

Stuart, R. A., and G. A. Isaac (1999). Freezing precipitation in Canada. *Atmosphere-Ocean*, *37*(1), 87-102.

Suklitsch, M., A. Gobiet, A. Leuprecht, and C. Frei (2008). High resolution sensitivity studies with the regional climate model CCLM in the Alpine Region. *Meteorologische Zeitschrift*, *17*(4), 467-476.

Sundqvist, H., E. Berge, and J. E. Kristjansson (1989). Condensation and cloud parameterization studies with a mesoscale numerical weather prediction model. *Monthly Weather Review*, *117*, 1641-1657.

Tao, W.-K., and J. Simpson (1989). Modeling of a tropical squall-type convective line. *Journal of Atmospheric Sciences, 46*, 177-202.

Tao, W.-K., J. Simpson, D. Baker, S. Braun, M.-D. Chou, B. Ferrier, D. Johnson, A. Khain, S. Lang, B. Lynn, C.-L. Shie, D. Starr, C.-H. Sui, Y. Wang, and P. Wetzel (2003). Microphysics, radiation and surface processes in the Goddard Cumulus Ensemble (GCE) model. *Meteorology Atmospheric Physics*, *82*, 97-137.

Tiedtke, M. (1989). A comprehensive mass flux scheme for cumulus parameterization in large-scale models. *Monthly Weather Review*, *117*(8), 1779-1800.

Tijm, A. B. C., and G. Lenderink (2003). Characteristics of CBR and STRACO versions. *Hirlam Newsletter*, *43*, 115-124.

Tjiputra, J. F., C. Roelandt, M. Bentsen, D. M. Lawrence, T. Lorentzen, J. Schwinger, Ø. Seland, and C. Heinze (2013). Evaluation of the carbon cycle components in the Norwegian Earth System Model (NorESM). *Geoscientific Model Development Discussions*, *6*, 301-325.

Todini, E. (1996). The ARNO rainfall-runoff model. *Journal of Hydrology*, *175*(1), 339-382.

Tokioka, T., A. Noda, A. Kitoh, Y. Nikaidou, S. Nakagawa, S. Yukimoto, and K. Takata (1995). A transient CO2 experiment with the MRI CGCM: Quick report. *Journal of the Meteorological Society of Japan*, *73*(4), 817-826.

Trapp, R. J., B. A. Halvorson, and N. S. Diffenbaugh (2007). Telescoping, multimodel approaches to evaluate extreme convective weather under future climates. *Journal of Geophysical Research: Atmospheres, 112*(D20109), 1-13.

Turner, S. (1994). *Analyse spectral des données du modèle regional du climat de l'UQÀM*: M.S. Thèse, Sciences de l'Atmosphère, Université du Québec à Montréal, 113 pp.

Vallis, G. K., G. J. Schutts, and M. E. B. Gray (1997). Balanced mesoscale motion and stratified turbulence forced by convection. *Quarterly Journal of Royal Meteorology Society*, *123*, 1621-1652.

VanZandt, T. E. (1982). A universal spectrum of buoyancy in the atmosphere. *Geophysical Research Letters*, *9*, 575-578.

Verseghy, D. L. (1991). CLASS: A Canadian land surface scheme for GCMs. Part I: Soil model. *International Journal of Climatology*, *11*, 111-133.

Verseghy, D. L. (2000). The Canadian land surface scheme (CLASS): Its history and future. *Atmosphere-Ocean*, *38*(1), 1-13.

Verseghy, D. L. (2008) *The Canadian Land Surface Scheme:* Technical documentation Version 3.4. Climate Research Division, Science and Technology Branch, Environment Canada.

Vidale, P. L., D. Lüthi, C. Frei, S. I. Seneviratne, and C. Schär (2003). Predictability and uncertainty in a regional climate model. *Journal of Geophysical Research*, *108*, 4586.

Voldoire, A., E. Sanchez-Gomez, D. S. y Mélia, B. Decharme, C. Cassou, S. Sénési, S. Valcke, I. Beau, A. Alias, M. Chevalier, M. Déqué, J. Deshayes, H. Douville, E. Fernandez, G. Madec, E. Maisonnave, M.-P. Moine, S. Planton, D. Saint-Martin, S. Szopa, S. Tyteca, R. Alkama, S. Belamari, A. Braun, L. Coquart, and F. Chauvin (2013). The CNRM-CM5.1 global climate model: description and basic evaluation. *Climate Dynamics*, *40*, 2091-2121.

Volodin, E. M., N. A. Dianskii, and A. V. Gusev (2010). Simulating present-day climate with the INMCM4.0 coupled model of the atmospheric and oceanic general circulations. *Izvestiya, Atmospheric and Oceanic Physics*, *46*(4), 414-431.

von Salzen, K., and N. A. McFarlane (2002). Parameterization of the bulk effects of lateral and cloud-top entrainment in transient shallow cumulus clouds. *Journal of Atmospheric Sciences*, *59*, 1405-1429.

von Salzen, K., J. F. Scinocca, N. A. McFarlane, J. Li, J. N. Cole, D. Plummer, D. Verseghy, M. C. Reader, X. Ma, M. Lazare, and L. Solheim (2013). The Canadian Fourth Generation Atmospheric Global Climate Model (CanAM4). Part I: Representation of Physical Processes. *Atmosphere-Ocean*, *51*(1), 104-125.

von Storch, J. S., V. V. Kharin, U. Cubasch, G. C. Hegerl, D. Schriever, H. von Storch, and E. Zorita (1997). A description of a 1260-year control integration with the coupled ECHAM1/LSG general circulation model. *Journal of Climate*, *10*(7), 1525-1543.

Wang, B., T. Zhou, and Y. Yu (2009). A view of Earth System Model development. *ACTA Meteorologica Sinica*, *1*, 1-17.

Wang, B. (2011). *CMIP5 in China*. Communication in the 15th WGCM, Boulder, USA. Available online http://www.wcrp-climate.org/wgcm/WGCM15/presentations/21Oct/WANG_WGCM.pdf

Wang, B., M. Liu, Y. Yu, L. Li, P. Lin, L. Dong, L. Liu, J. Liu, W. Huang, S. Xu, S. Shen, Y. Pu, W. Xue, K. Xia, Y. Wang, W. Sun, N. Hu, X. Huang, H. Liu, W. Zheng, B. Wu, T. Zhou, and G. Yang (2013). Preliminary Evaluations of FGOALS-g2 for Decadal Predictions. *Advances in Atmospheric Sciences, 3*, 674-683.

Watanabe M, T. Suzuki, R. Oishi, Y. Komuro, S. Watanabe, S. Emori, T. Takemura, M. Chikira, T. Ogura, M. Sekiguchi, K. Takata, D. Yamazaki, T. Yokohata, T. Nozawa, H. Hasumi, H. Tatebe, and M. Kimoto (2010). Improved climate simulation by MIROC5: mean states, variability, and climate sensitivity. *Journal of Climate*, *23*(23), 6312-6335.

Watanabe, M., T. Hajima, K. Sudo, T. Nagashima, T. Takemura, H. Okajima, T. Nozawa, H. Kawase, M. Abe, T. Yokohata, T. Ise, H. Sato, E. Kato, K. Takata, S. Emori, and M. Kawamiya (2011). MIROC-ESM: model description and basic results of CMIP5-20c3m experiments. *Geoscientific Model Development Discussions, 4*(2), 1063-1128.

Webb, M., C. Senior, S. Bony, and J. J. Morcrette (2001). Combining ERBE and ISCCP data to assess clouds in the Hadley Centre, ECMWF and LMD atmospheric climate models. *Climate Dynamics*, *17*(12), 905-922.

Weber, R. O., and P. Kaufmann (1998). Relationship of synoptic winds and complex terrain flows during the MISTRAL field experiment. *Journal of Applied Meteorology*, *37*, 1486-1496.

Weisman, M. L., W. C. Skamarock, and J. B. Klemp (1997). The resolution dependence of explicitly modeled convective systems. *Monthly Weather Review*, *125*(4), 527-548.

White, P. W. (2001). *Physical processes.* (CY23R4). European Center for Medium-Range Weather Forecasts (ECMWF), Reading, United Kingdom.

Wu, T., R. Yu, F. Zhang, Z. Wang, M. Dong, L. Wang, X. Jin, D. Chen, and L. Li (2010). The Beijing Climate Center atmospheric general circulation model: description and its performance for the present-day climate. *Climate Dynamics*, *34*(1), 123-147.

Xin, X., T. Wu, and J. Zhang (2012a). Introductions to the CMIP 5 simulations conducted by the BCC climate system model (in Chinese). *Advances in Climate Change Research,* in press.

Yeh, K. S., S. Gravel, A. Méthot, A. Patoine, M. Roch, and A. Staniforth (2002). The operational CMC-MRB global environmental multiscale (GEM) model. Part III: non-hydrostatic formulation. *Monthly Weather Review*, *130*, 339-356.

Yu, Y., X. Zhang, and Y. Guo (2004). Global coupled ocean-atmosphere general circulation models in LASG/IAP. *Advances in Atmospheric Sciences*, *21*, 444-455.

Yu, X., and T. Y. Lee (2010). Role of convective parameterization in simulations of a convective band at grey-zone resolutions. *Tellus*, *62A*, 617-632.

Yuan, L., and K. Hamilton (1994). Equilibrium dynamics in a forced-dissipative f-plane shallow-water system. *Journal of Fluid Mechanics*, *280*(1), 369-394.

Yukimoto, S., A. Noda, A. Kitoh, M. Sugi, Y. Kitamura, M. Hosaka, K. Shibata, S. Maeda, and T. Uchiyama (2001). The new Meteorological Research Institute coupled GCM (MRI-CGCM2) Model climate and variability. *Meteorology and Geophysics*, *51*(2), 47-88.

Yukimoto, S., Y. Adachi, and M. Hosaka (2012). A New Global Climate Model of the Meteorological Research Institute: MRI-CGCM3: Model Description and Basic Performance (Special Issue on Recent Development on Climate Models and Future Climate Projections). *Journal of the Meteorological Society of Japan*, *90*, 23-64.

Zadra, A., M. Roch, S. Laroche, and M. Charron (2003). The subgrid-scale orographic blocking parametrization of the GEM Model. *Atmosphere-Ocean*, *41*(2), 155-170.

Zadra, A., D. Caya, J. Côté, B. Dugas, C. Jones, R. Laprise, K. Winger, and L.-Ph. Caron (2008). The next Canadian regional climate model. *Physique Canada*, *64*, 75-83.

Zhang, G. J., and N. A. McFarlane (1995). Sensitivity of climate simulations to the parameterization of cumulus convection in the CCC-GCM. *Atmosphere-Ocean*, *3*, 407-446.

Zhang, G. J., and T. Wu (2012). *The impact of external forcings on climate during the past millennium: Results from transient simulation with BCC_CSM1.1.* Geophysical Research Abstracts, 14, EGU2012-448.

Zhang, L., M. Dong, and T. Wu (2011). Changes in precipitation extremes over Eastern China simulated by the Beijing Climate Center Climate System Model (BCC_CSM1.0). *Climate Research*, *50*, 227-245.

Zhao, M., I. M. Held, S. J. Lin, and G. A. Vecchi (2009). Simulations of global hurricane climatology, interannual variability, and response to global warming using a 50-km resolution GCM. *Journal of Climate*, *22*(24), 6653-6678.